


5-2021

Improvement of Stability of a Grid-Connected Inverter with an LCL filter by Robust Strong Active Damping and Model Predictive Control

Seungyong Lee
University of Arkansas, Fayetteville

Follow this and additional works at: <https://scholarworks.uark.edu/etd>

 Part of the [Controls and Control Theory Commons](#), [Power and Energy Commons](#), and the [VLSI and Circuits, Embedded and Hardware Systems Commons](#)

Citation

Lee, S. (2021). Improvement of Stability of a Grid-Connected Inverter with an LCL filter by Robust Strong Active Damping and Model Predictive Control. *Graduate Theses and Dissertations* Retrieved from <https://scholarworks.uark.edu/etd/4082>

This Dissertation is brought to you for free and open access by ScholarWorks@UARK. It has been accepted for inclusion in Graduate Theses and Dissertations by an authorized administrator of ScholarWorks@UARK. For more information, please contact scholar@uark.edu.

Improvement of Stability of a Grid-Connected Inverter with an LCL filter
by Robust Strong Active Damping and Model Predictive Control

A dissertation submitted in partial fulfilment
of the requirement for the degree of
Doctor of Philosophy in Engineering with a concentration in Electrical Engineering

by

Seungyong Lee
Sogang University
Bachelor of Science in Chemistry and Electronics 2003
University of Arkansas
Master of Science in Electrical Engineering 2013

May 2021
University of Arkansas

This dissertation is approved for recommendation to the Graduate Council.

Roy A. McCann Ph.D.
Dissertation Director

Jingxian Wu Ph.D.
Committee Member

Yue Zhao Ph.D.
Committee Member

Mark E. Arnold Ph.D.
Committee Member

ABSTRACT

This study addresses development and implementation of robust control methods for a three-phase grid-connected voltage source inverter (VSI) accompanied by an inductive-capacitive-inductive (LCL) filter. A challenge of current control for the VSI is LCL filter resonance near to the control stability boundary, which interacts with the inverter control switching actions and creates the possibility of instability. In general, active damping is needed to stabilize the system and ensure robust performance in steady-state and dynamic responses. While many active damping methods have been proposed to resolve this issue, capacitor-current-feedback active damping has been most widely used for its simple implementation.

There has been no clear consensus regarding design of a control system including capacitor-current-feedback active damping. This is due to the fact that simulation/experiment results are not congruent with the design analyses on which the control is designed. This study explains the incoherence between theory and practice when it comes to a capacitor-currents-feedback active damping system. Proposed capacitor-current-estimate active damping utilizing a developed posteriori Kalman estimator gives coherent simulation results as expected from the design analyses. This reveals that the highly oscillatory capacitor currents containing the inverter switching effects bring about uncertainty in the system performance. The switching effects are not incorporated in the analyses and control system design. Therefore, it is required to remove the switching noise from the capacitor currents in order to yield consistent results.

It has been confirmed that the proportional-negative feedback of the capacitor current is equivalent to virtual impedance connected in parallel with the filter capacitor. In a digitally controlled system, the computation delay causes the equivalent resistance of the virtual impedance to become negative in the frequency range of $f_s/6$ to $f_s/2$, which produces a pair of

open-loop unstable poles in RHP. This happens when the displaced resonance peak by active damping is in that region. Thus, an a priori Kalman estimator has been developed to generate one-sample-ahead state variable estimates to reconstruct the capacitor currents for active damping, which can compensate for the delay. The one-sample-ahead capacitor-current estimates are computed from the inverter-side and grid-side current estimates. The proposed method provides extended limits of the active damping gain that improve robustness against system parameter variation. It also allows strong active damping which can sufficiently attenuate the resonance.

Grid condition is another significant factor affecting the stability of the system. In particular, a weak grid tends to provide high impedance. The system employing the proposed active damping method stably operates in a weak grid, ensuring robustness under grid impedance variation. The developed Kalman estimators offer an effective and easy way of determining the stability status of a system in addition to the functions of filtering and estimation. Stability analysis can be easily made since state variable estimates go to infinity when a system is unstable.

As a promising approach, model predictive control (MPC) has been designed for the system. This study suggests that MPC including active damping can be employed for a grid-connected VSI with an LCL filter with good dynamic performance.

ACKNOWLEDGEMENTS

I am very grateful to my research advisor, Dr. Roy A. McCann, for his substantial assistance in many aspects. I have been attracted by his profound and intriguing insight into a control system world, and I ended up being a control systems engineer with full of happiness. I would like to thank to my advisory committee members, Dr. Jingxian Wu, Dr. Yue Zhao, and Dr. Mark E. Arnold, for having them on my advisory committee. Also, I offer my appreciation to the colleagues who spent time with me in search of truth in science and engineering. Special thanks to my hometown friends who bring me a lot of joy.

I wish to express my deepest gratitude and love to my parents, wife, brothers, and all other family members. Their love and support are everything to me.

TABLE OF CONTENTS

Chapter 1	Introduction	1
1.1	Power Inverters in Renewable Energy and Grid Integration	1
1.2	Dissertation Motivation	3
1.3	Dissertation Objectives	7
1.4	Dissertation Organization	9
Chapter 2	Background	10
2.1	Introduction.....	10
2.2	NCREPT Microgrid System Overview	10
2.3	Direct-Quadrature-Zero (dq0) Transformation.....	14
2.3.1	Direct Transformation: abc to $dq0$	15
2.3.2	Indirect Transformation: abc to $\alpha\beta0$ and $\alpha\beta0$ to $dq0$	16
Chapter 3	LCL Filter Design	18
3.1	Introduction.....	18
3.2	LCL Filter Mathematical Model.....	19
3.3	LCL Filter Design Methodology	23
3.3.1	Resonance Frequency Condition	23
3.3.2	Maximum Value of the Total Inductance	25
3.3.3	Maximum Value of the LCL Filter Capacitance	25
3.3.4	Minimum DC-Link Voltage	26
3.3.5	Tuning of the Inverter-Side Inductance	29
3.3.6	Tuning of the Grid-Side Inductance	30

3.4	LCL Filter Parameter Verification.....	31
3.5	LCL Filter Design Procedure.....	32
3.6	LCL Filter Design With Robustness Against Grid Impedance Variation	35
Chapter 4 Damping Methods for Internal Stability		39
4.1	Introduction.....	39
4.2	Passive Damping Methods.....	39
4.3	Filter-Based Damping Methods	44
4.3.1	Notch Filter	46
4.3.2	Low-Pass Filter	49
4.3.3	All-Pass Filter	51
4.4	State Feedback-Based Damping Methods	52
4.4.1	Capacitor Current Feedback	54
4.4.2	Capacitor Voltage Feedback.....	55
4.4.3	Inverter-Side Current Feedback.....	55
4.4.4	Grid-Side Current Feedback	56
Chapter 5 Control System Design Wth Active Damping		59
5.1	Discrete-Time Model of Active Damping Current Controller	59
5.2	Identification of the Active Damping Regions	62
5.3	Controller and Gain Determination	63
5.4	Capacitor Current Damping Gain Determination	65
5.5	Design of Current Controller and Active Damping Gain	66
5.6	Stability Anaysis of Capacitor-Current-Feedback Acive Damping	81
Chapter 6 Delay Compensation		92

6.1	VSI With an LCL Filter Discrete-Time Model.....	92
6.2	Design of Kalman Estimators	94
6.3	Simulation Results When f_r is Above f_{crit}	103
6.4	Simulation Results When f_r is Below f_{crit}	113
Chapter 7 Model Predictive Control.....		126
7.1	Introduction.....	126
7.2	Modeling of a Three-Phase Inverter for Model Predictive Control.....	127
7.2.1	Modeling of Grid Currents in abc -Frame	127
7.2.2	Modeling of Grid Currents in $\alpha\beta$ -Frame	130
7.2.3	Modeling of Grid Currents in dq -Frame	130
7.3	Cost Function	131
7.4	MPC Discrete Model With an Embedded Integrator.....	132
7.5	Prediction of State and Output Variables Within a Prediction Horizon	134
7.6	Cost Function Minimization	136
7.7	Closed-loop Control System.....	137
Chapter 8 Conclusion.....		142
References.....		144
Appendices.....		154
Appendix A: NCREPT Microgrid System Parameters.....		154

LIST OF FIGURES

Figure 1.1. AC microgrid testbed dc-bus voltage: (a) the variable-voltage variable-frequency drive (b) the regenerative drive.....	4
Figure 1.2. AC microgrid testbed phase current.....	5
Figure 2.1. NCREPT test facility building at the Arkansas engineering research center.....	10
Figure 2.2. NCREPT one-line diagram.....	11
Figure 2.3. Cascaded converters-based microgrid system.....	12
Figure 2.4. Single-phase equivalent circuit for the modified microgrid.....	13
Figure 2.5. Back-to-back topology for the regenerative and the variable-voltage variable-frequency drives.....	14
Figure 3.1. (a) A three-phase grid-connected VSI with an LCL filter. (b) Single-phase equivalent circuit.....	20
Figure 3.2. Single-phase equivalent circuit without the inductor internal resistances.....	21
Figure 3.3. Three-phase inverter as a hex bridge.....	27
Figure 3.4. Bode magnitude and phase plots for the LCL filter system with or without the internal resistances of the filter inductors.....	34
Figure 3.5. Bode diagram of the LCL filter system with the minimum grid inductance or with the maximum grid inductance.....	38
Figure 4.1. Placements of a damping resistor of six typical passive damping methods.....	39
Figure 4.2. Placements of a damping resistor of six typical passive damping methods.....	42
Figure 4.3. Closed-loop current control block diagram of digital filter-based active damping with two current feedback strategies: (a) inverter-side current feedback (ICF) (b) grid-side feedback (GCF).....	45
Figure 4.4. Bode diagrams of notch-filter-based damping method with two different feedback strategies: (a) inverter-side current feedback (ICF) (b) grid-side feedback (GCF).....	48
Figure 4.5. Bode diagram of the low-pass filter of which cutoff frequency is located at the LCL filter resonance frequency.....	50

Figure 4.6. Block diagrams of various state feedback-based damping methods: (a) capacitor current feedback, (b) capacitor voltage feedback, (c) inverter-side current feedback, and (d) grid-side current feedback	53
Figure 4.7. Equivalent circuit of state feedback-based damping methods	57
Figure 5.1 Grid-connected voltage source inverter with an LCL filter and an active damping current controller.....	59
Figure 5.2 Single-phase equivalent current controller architectures. (a) A single-loop feedback current controller. (b) Dual-loop controller with capacitor-current active damping	59
Figure 5.3. Bode diagram of the loop gain of single-loop grid-current control with variations in grid inductance.....	73
Figure 5.4. Stability analysis with root loci of variations in active damping gain K_{ad} for different cases in terms of resonance frequency (f_{res}) relative to the critical frequency (f_{crit})	75
Figure 5.5 (a) Bode diagrams of the forward-path transfer functions of the single- and dual-loop current controllers. Root loci of the dual-loop current controller with respect to active damping gain K_{ad} : (b) resonance frequency is higher than the critical resonance frequency, (c) resonance frequency is at the critical frequency, (d) resonance frequency is lower than the critical frequency.....	77
Figure 5.6 Active damping applied VSI with an LCL filter in a stiff grid with a step change in active power at 0.2 s and a step change in reactive power at 0.3 s and subsequent active damping off at 0.4 s. (a) Grid currents. (b) Grid voltages. (c) Grid phase-a current. (d) Injected active and reactive powers	79
Figure 5.7. Active damping applied VSI with an LCL filter in a weak grid with a step change in active power at 0.2 s and a step change in reactive power at 0.3 s and subsequent active damping off at 0.4 s. (a) Grid currents. (b) Grid voltages. (c) Grid phase-a current. (d) Injected active and reactive powers	80
Figure 5.8. Control block diagram of the LCL filter-equipped grid-connected inverter with capacitor-current-proportional-feedback active damping.....	82
Figure 5.9. Representation of the LCL filter-equipped grid-connected inverter with equivalent virtual impedance of the capacitor-current-proportional-feedback active damping. (a) Block diagram. (b) Virtual impedance equivalent circuit	83
Figure 5.10. Magnitude curves of R_{eq} and X_{eq} as a function of frequency.....	85
Figure 5.11. Bode diagrams of the loop gain of the system when $f_r > f_s/6$: (a) uncompensated, compensated, and compensated with active damping (b) compensated, compensated with active damping, and compensated with excessive active damping	87

Figure 5.12. Bode diagrams of the loop gain of the system when $f_r < f_s/6$, $L_g = 60 \mu\text{H}$: (a) uncompensated, compensated, and compensated with active damping (b) compensated, compensated with active damping, and compensated with excessive active damping	88
Figure 6.1 (a) Proposed control system with active damping of one-sample-ahead estimated capacitor current by the Kalman a priori estimator. (b) Block diagram of the Kalman a priori estimator. (c) Block diagram of the Kalman a posteriori estimator.....	97
Figure 6.2. Magnitude curves of R_{eq} and X_{eq} as a function of frequency.....	98
Figure 6.3. Bode diagrams of the loop gain of the system employing one-sample-ahead capacitor-current-estimate-proportional-negative feedback with active damping disabled, active damping enabled, or strong active damping enabled: (a) when $f_r > f_s/6$, (b) when $f_r < f_s/6$, $L_g = 60 \mu\text{H}$	99
Figure 6.4 Root loci of the dual-loop control systems with respect to the active damping K_{ad} for a given K_p of 0.00024 A^{-1} . (a) With the capacitor-current-estimate-feedback active damping employing the a posteriori Kalman estimator when $f_r > f_{crit}$, $L_g = 0 \mu\text{H}$. (b) With the one-sample-ahead capacitor-current-estimate-feedback active damping employing the a priori Kalman estimator when $f_r > f_{crit}$, $L_g = 0 \mu\text{H}$. (c) The same as (a) when $f_r < f_{crit}$, $L_g = 60 \mu\text{H}$ (d) The same as (b) when $f_r < f_{crit}$, $L_g = 60 \mu\text{H}$	101
Figure 6.5 (a) Grid-injected three-phase currents when $f_r > f_{crit}$, and the one-sample-ahead capacitor-current-estimate active damping is disabled at 50 ms and enabled at 150 ms. (b) Current THD after active damping is disabled	104
Figure 6.6 Grid-side three-phase currents for three different types of active damping schemes with an active damping gain of $K_{ad} = 0.0001 \text{ A}^{-1}$ when $f_r > f_{crit}$. (a) Capacitor-current-feedback active damping. (b) Current THD. (c) Capacitor-current-estimate-feedback active damping. (d) Current THD. (e) One-sample-ahead capacitor-current-estimate-feedback active damping. (f) Current THD	105
Figure 6.7 Grid-side three-phase currents for three different types of active damping schemes with an increased active damping gain of $K_{ad} = 0.0003 \text{ A}^{-1}$ when $f_r > f_{crit}$. (a) Capacitor-current-feedback active damping. (b) Current THD. (c) Capacitor-current-estimate-feedback active damping. (d) Current THD. (e) One-sample-ahead capacitor-current-estimate-feedback active damping. (f) Current THD	106
Figure 6.8 Three-phase currents and their estimates in the dq frame for three different types of active damping schemes with an active damping gain of $K_{ad} = 0.0001 \text{ A}^{-1}$ when $f_r > f_{crit}$. Capacitor-current-feedback active damping: (a) inverter-side currents, (b) grid-side currents. Capacitor-current-estimate-feedback active damping: (c) inverter-side currents, (d) grid-side currents. One-sample-ahead capacitor-current-estimate-feedback active damping: (e) Inverter-side currents (f) Grid-side currents	108

Figure 6.9 Three-phase currents and their estimates in the dq frame for three different types of active damping schemes with an increased active damping gain of $K_{ad} = 0.0003 \text{ A}^{-1}$ when $f_r > f_{crit}$. Capacitor-current-feedback active damping: (a) inverter-side currents, (b) grid-side currents. Capacitor-current-estimate-feedback active damping: (c) inverter-side currents, (d) grid-side currents. One-sample-ahead capacitor-current-estimate-feedback active damping: (e) Inverter-side currents (f) Grid-side currents109

Figure 6.10 One-sample-ahead-current estimates for the one-sample-ahead capacitor-current-estimate-feedback active damping system. With an active damping gain of $K_{ad} = 0.0001 \text{ A}^{-1}$: (a) inverter-side current estimates, (b) grid-side current estimates. With an increased active damping gain of $K_{ad} = 0.0003 \text{ A}^{-1}$: (c) inverter-side current estimates, (d) grid-side current estimates110

Figure 6.11 Three-phase capacitor currents or estimates for three different types of active damping schemes with an active damping gain of $K_{ad} = 0.0001 \text{ A}^{-1}$ when $f_r > f_{crit}$. Capacitor-current-feedback active damping: (a) measured capacitor currents, (b) current THD. Capacitor-current-estimate-feedback active damping: (c) capacitor-current estimates, (d) current THD. One-sample-ahead capacitor-current-estimate-feedback active damping: (e) one-sample-ahead capacitor-current estimates, (f) current THD.....111

Figure 6.12 Three-phase capacitor currents or estimates for three different types of active damping schemes with an active damping gain of $K_{ad} = 0.0003 \text{ A}^{-1}$ when $f_r > f_{crit}$. Capacitor-current-feedback active damping: (a) measured capacitor currents, (b) current THD. Capacitor-current-estimate-feedback active damping: (c) capacitor-current estimates, (d) current THD. One-sample-ahead capacitor-current-estimate-feedback active damping: (e) one-sample-ahead capacitor-current estimates, (f) current THD.....112

Figure 6.13 (a) Grid-injected three-phase currents when $f_r < f_{crit}$ with a grid inductance of $60 \mu\text{H}$, and the one-sample-ahead capacitor-current-estimate-feedback active damping is disabled at 50 ms and enabled at 150 ms. (b) Current THD after active damping is disabled113

Figure 6.14 Grid-side three-phase currents for three different types of active damping schemes with an active damping gain of $K_{ad} = 0.0001 \text{ A}^{-1}$ when $f_r < f_{crit}$ with a grid inductance of $60 \mu\text{H}$ (a) Capacitor-current-feedback active damping. (b) Current THD. (c) Capacitor-current-estimate-feedback active damping. (d) Current THD. (e) One-sample-ahead capacitor-current-estimate-feedback active damping. (f) Current THD114

Figure 6.15 Grid-side three-phase currents for three different types of active damping schemes with an increased active damping gain of $K_{ad} = 0.0003 \text{ A}^{-1}$ when $f_r < f_{crit}$ with a grid inductance of $60 \mu\text{H}$. (a) Capacitor-current-feedback active damping. (b) Current THD. (c) Capacitor-current-estimate-feedback active damping. (d) Current THD. (e) One-sample-ahead capacitor-current-estimate-feedback active damping. (f) Current THD.....115

Figure 6.16 Three-phase currents and their estimates in the dq frame for three different types of active damping schemes with an active damping gain of $K_{ad} = 0.0001 \text{ A}^{-1}$ when $f_r < f_{crit}$ with a grid inductance of $60 \mu\text{H}$. Capacitor-current-feedback active damping: (a) inverter-side currents, (b) grid-side currents. Capacitor-current-estimate-feedback active damping: (c) inverter-side

currents, (d) grid-side currents. One-sample-ahead capacitor-current-estimate-feedback active damping: (e) Inverter-side currents (f) Grid-side currents.....116

Figure 6.17 Three-phase currents and their estimates in the dq frame for three different types of active damping schemes with an increased active damping gain of $K_{ad} = 0.0003 \text{ A}^{-1}$ when $f_r < f_{crit}$ with a grid inductance of $60 \mu\text{H}$. Capacitor-current-feedback active damping: (a) inverter-side currents, (b) grid-side currents. Capacitor-current-estimate-feedback active damping: (c) inverter-side currents, (d) grid-side currents. One-sample-ahead capacitor-current-estimate-feedback active damping: (e) Inverter-side currents (f) Grid-side currents.....117

Figure 6.18 One-sample-ahead-current estimates for the one-sample-ahead capacitor-current-estimate-feedback active damping system. With an active damping gain of $K_{ad} = 0.0001 \text{ A}^{-1}$: (a) inverter-side current estimates, (b) grid-side current estimates. With an increased active damping gain of $K_{ad} = 0.0003 \text{ A}^{-1}$: (c) inverter-side current estimates, (d) grid-side current estimates118

Figure 6.19 Three-phase capacitor currents or estimates for three different types of active damping schemes with an active damping gain of $K_{ad} = 0.0001 \text{ A}^{-1}$ when $f_r < f_{crit}$ with a grid inductance of $60 \mu\text{H}$. Capacitor-current-feedback active damping: (a) measured capacitor currents, (b) current THD. Capacitor-current-estimate-feedback active damping: (c) capacitor-current estimates, (d) current THD. One-sample-ahead capacitor-current-estimate-feedback active damping: (e) one-sample-ahead capacitor-current estimates, (f) current THD.....119

Figure 6.20 Three-phase capacitor currents or estimates for three different types of active damping schemes with an active damping gain of $K_{ad} = 0.0003 \text{ A}^{-1}$ when $f_r < f_{crit}$ with a grid inductance of $60 \mu\text{H}$. Capacitor-current-feedback active damping: (a) measured capacitor currents, (b) current THD. Capacitor-current-estimate-feedback active damping: (c) capacitor-current estimates, (d) current THD. One-sample-ahead capacitor-current-estimate-feedback active damping: (e) one-sample-ahead capacitor-current estimates, (f) current THD.....120

Figure 6.21 Three-phase grid-side currents and their estimates in the dq frame for two different types of active damping schemes with an active damping gain of $K_{ad} = 0.0001 \text{ A}^{-1}$ when $f_r < f_{crit}$ with a grid inductance of $60 \mu\text{H}$. (a) Current-state grid-side-current estimates for the capacitor-current-estimate-feedback active damping system (b) One-sample-ahead grid-side-current estimates of the one-sample-ahead capacitor-current-estimate-feedback active damping system121

Figure 6.22 A step change in supply power to the grid for the one-sample-ahead capacitor-current-estimate active damping system when $f_r > f_{crit}$: (a) grid-side currents, (b) grid-side currents in the dq frame, (c) active and reactive powers. When $f_r < f_{crit}$, $L_g = 60 \mu\text{H}$. (d) grid-side currents, (e) grid-side currents in the dq frame, (f) active and reactive powers122

Figure 6.23. Grid-side current THDs of the one-sample-ahead capacitor-current-estimate-feedback active damping system with variation in grid inductance.125

Figure 7.1. Block diagram of a three-phase inverter with a model predictive control system128

Figure 7.2. Model predictive control application to a grid-connected inverter132

Figure 7.3 FCS-MPC for the VSI when $f_r < f_{crit}$, $L_g = 60 \mu\text{H}$. (a) With the L filter. (b) Current THD. (c) With the LCL filter without active damping. (d) Current THD. (e) With the LCL filter with active damping. (f) Current THD140

LIST OF TABLES

Table 2.1. System Component and Parameter Values	13
Table 3.1. Grid-Connected Inverter and LCL Filter System Parameters	33
Table 3.2. Robust LCL Filter Parameters Against Grid Inductance Variation.....	36
Table 4.1. Passive Damping Methods and Transfer Functions	40
Table 4.2. Passive Damping Methods and Damping Resistance Selection.....	42
Table 5.1. Grid-Connected Inverter of the Regenerative Drive and LCL Filter System Parameters.....	69
Table 6.1. The Stable Operation Regions of the Active Damping Gain.....	123
Table 6.2. Grid-Side Current THDs for Three Different Types of the Active Damping Methods.....	124

CHAPTER 1 INTRODUCTION

1.1 Power Inverters in Renewable Energy and Grid Integration

In an effort to reduce fossil fuel consumption and carbon dioxide emissions, microgrid systems consisting of distributed power generators have been widely employed. Nonetheless, the power quality characteristics of distributed generators (DGs) are highly affected by unpredictable environmental conditions, which have adverse impacts on the power quality of the microgrid [1]. A back-to-back (BTB) converter system is one of the most broadly used power converter topologies that are utilized to provide the capability of improving the power quality of microgrids. The converter's ability of active and reactive power supply via bidirectional power flow control helps to regulate the frequency and voltage of microgrids with high stability [2]. A BTB converter consists of two voltage source inverters (VSI) which are individually accompanied by an inductive-capacitive-inductive (LCL) filter to attenuate pulse width modulation (PWM) harmonics. Inverter switching actions cause the PWM harmonics. The LCL filter leads to a reduction in overall size and weight when compared with a conventional inductive (L) filter [3]–[10]. However, LCL filters introduce substantial complexity from a control perspective due to a resonance phenomenon caused by the filter elements which creates a pair of system poles located on the closed-loop stability boundary. Therefore, designing a control system for a grid-connected VSI with an LCL filter is a very challenging task [11]–[33]. In particular, a weak grid implying a grid with a lower short circuit ratio (SCR) can lead to voltage fluctuations at the inverter terminals and consequently cause inverter instability [34]–[38]. The literature [23] demonstrates a decrease in the grid inductance does not necessarily improve the stability of grid-connected VSIs. It also claims that the system stability is a function of both the

grid R/X ratio and grid inductance. Additionally, despite the grid-side inductor of the LCL filter is in series with the grid impedance, they have different effects on the stability of the system [39].

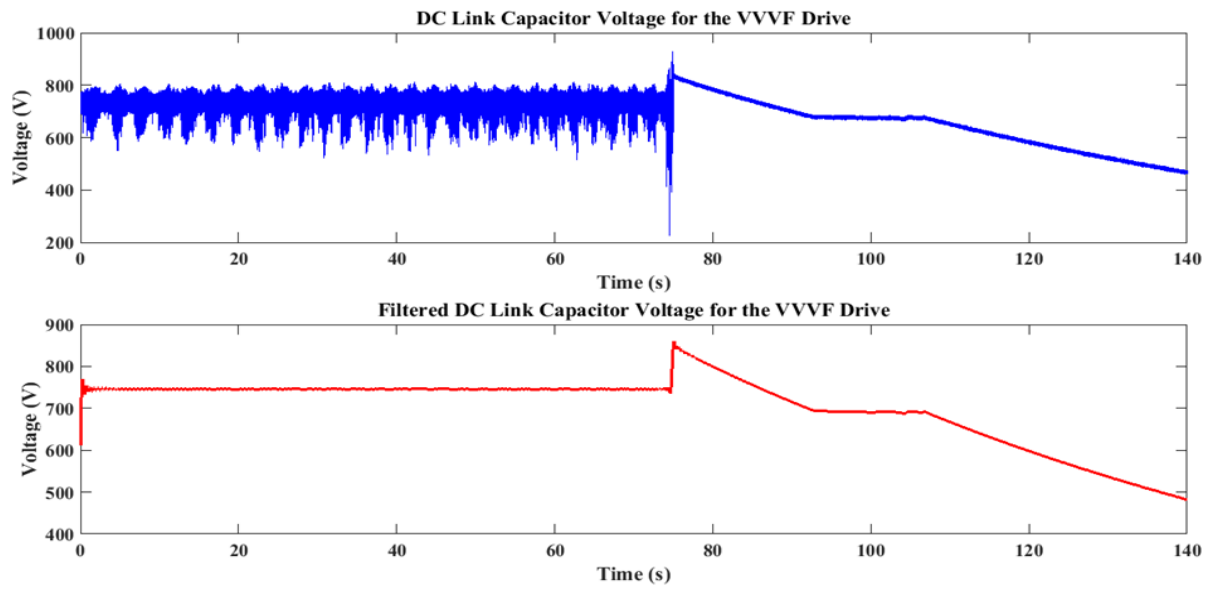
There are many types of model predictive control (MPC) under different names but they all have a similarity, which is to predict future events and take control actions based on objective function minimization [40]–[42]. Since predictive control drew a growing attention almost three decades ago, research and development activities in finite control set MPC (FCS-MPC) have become substantially active for the last decade [42], [43]. As the consequences of the intensive study, advanced analysis techniques and practical tests for FCS-MPC have been performed for a wide range of power conversion applications [41]. FCS-MPC has many advantages over classical linear controller, which are nonlinear nature, modulator-free structure and high-performance operation [42], [44]. These merits suggest that FCS-MPC could be applied in a wide variety of systems in place of conventional control methods which are quite vulnerable to uncertainties in practice [45]–[47]. Non-linearity of systems limits the closed-loop performance because the conventional methods develop controllers based on a linearized model [42].

For a grid-connected VSI, current control is commonly performed with a linear proportional integral (PI) controller in the synchronous reference frame. The controller has been designed based on the fixed resonance frequency of the output LCL filter. However, the filter resonance is also affected by the equivalent grid impedance and is therefore subject to change depending on grid conditions. This further complicates designing a robust PI controller. As a solution of the issue, a combined control strategy including MPC has high expectations since the dynamics of the LCL filter are decoupled by the MPC and therefore current controller design can be simplified with a reduced model of the system [48].

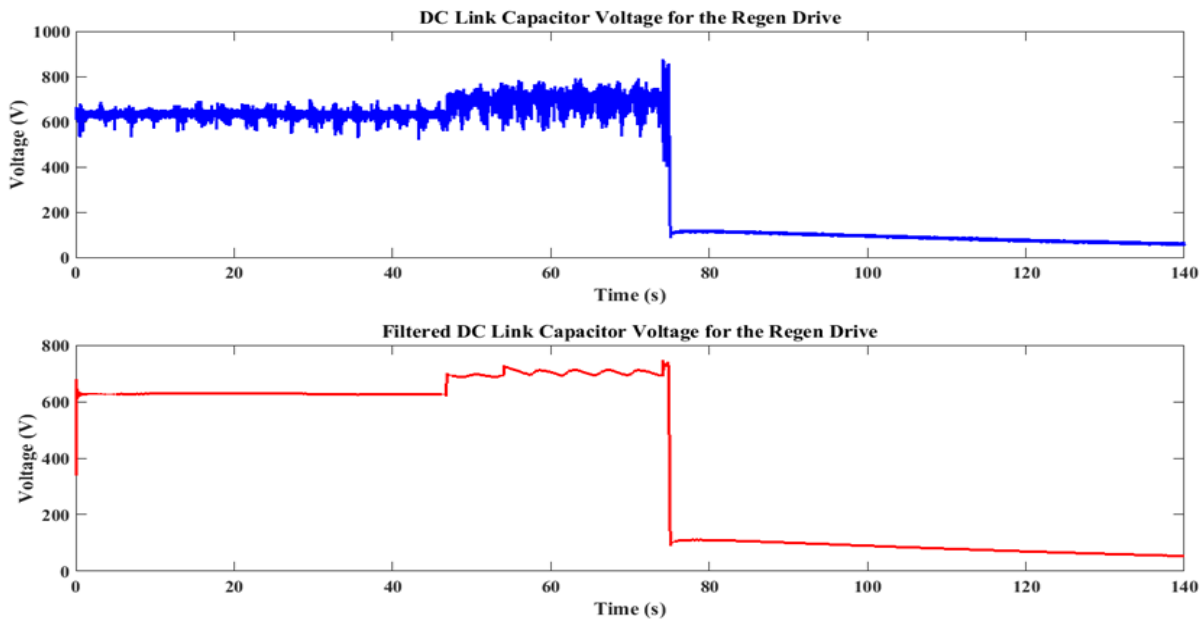
1.2 Dissertation Motivation

Integration of renewable resources into an existing grid forms a microgrid, which can operate either in grid-connected or isolated mode. As such, an AC grid-connected 13.8 kV, 2 MVA microgrid laboratory testbed exists at the National Center for Reliable Electric Power Transmission (NCREPT) located at the University of Arkansas Research Park. The microgrid contains two BTB converters, which are called variable-voltage variable-frequency (VVVF) and regenerative drives. The individual BTB converter consists of an active front end rectifier and an inverter sharing a common dc-link capacitor to ensure the power decoupling of the converter system. In addition, an LCL filter is connected to the each side of the converter not only for harmonic attenuation but also as an important power conversion interface. However, the grid-connected three-phase inverter system is prone to becoming unstable due to resonance from the LCL filter and grid impedance variations. Besides, the dc-bus voltage is hardly kept constant by the action of its controller during large power variation transients. Sometimes the dc-bus voltage suddenly fails to maintain its stability as shown in Figure 1.1. With consideration of the dc-bus voltage fluctuation and the resonance effect, a designed controller for the inverter should ensure robust performance in steady-state and dynamic response. The requirement for a robust controller was motivated by the very low bandwidth controller causing very slow response of the system and the instability of the microgrid laboratory testbed.

With respect to resonance damping methods for improving the internal stability of individual inverter, passive damping (PD) methods can be applied by adding a resistor in series or parallel with the element of an LCL filter. Nonetheless, the presence of an additional passive element causes inevitable damping losses and degraded harmonics attenuation ability in high-



(a)



(b)

Figure 1.1. AC microgrid testbed dc-bus voltage: (a) the variable-voltage variable-frequency drive (b) the regenerative drive.

frequencies. Furthermore, complex PD methods which are realized by adding a shunt capacitor or inductor in the capacitor branch of an LCL filter diminish power losses and regain the filtering

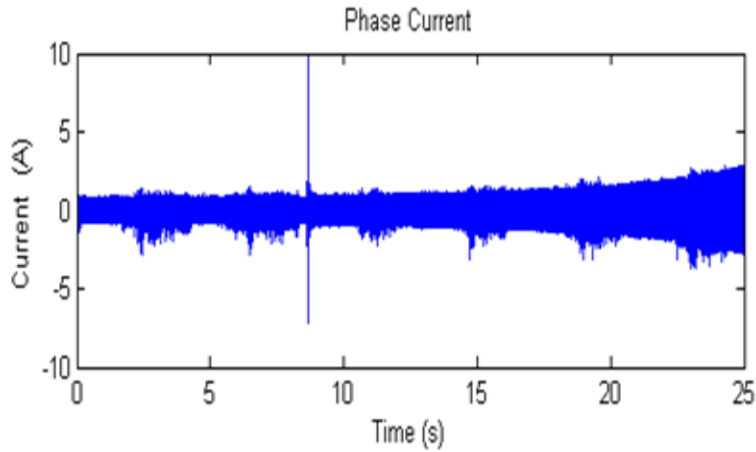


Figure 1.2. AC microgrid testbed phase current.

performance, yet the advantages are compromised by increased size and weight of the LCL filter [22]. In contrast to PD methods, active damping strategies have high efficiency and flexibility. Digital filter-based active damping methods are applicable to suppress LCL filter resonance, without an extra cost for sensors, while the robustness of the methods are poor [22]. Feeding back the filter state variables is very effective and popular for resonance active damping. Among state feedback-based active damping methods, proportional feedback of the filter capacitor current has been widely used due to its effectiveness and simplicity. This damping method has been revealed to be equivalent to a virtual resistance connected in parallel with the filter capacitor [49].

Designing current control for an LCL-filtered VSI is complicated by potential instability which is attributed to digital delays and inverter switching action coupled with the resonance frequency of the filter and grid impedance. When a single loop grid-current-controlled system is under a condition that the filter resonance frequency, f_r , is higher than the critical frequency, $f_s/6$, where f_s is the sampling frequency, the stability of the system is ensured without any damping

applied. However, the undamped resonance peak brings about low bandwidth, yielding slow dynamics. A worse scenario is that the undamped resonance peak is shifted at frequencies lower than the critical frequency due to variations in the filter parameters and grid impedance, causing system instability [50]. Therefore, it still draws a lot of attention to employ a robust and suitable damping solution. The most widely used active damping method, capacitor current proportional feedback, is discovered to be inequivalent to pure resistance. It is rather regarded as virtual impedance due to the digital delays. The impedance consists of frequency-dependent resistance and reactance. In nature, the resistance contributes to damping of the resonance, and the reactance shifts the LCL filter resonance frequency to a new system resonance frequency. However, the equivalent resistance becomes negative in the frequency range between the critical frequency, $f_s/6$, and the half-sampling frequency, $f_s/2$. This, in turn, introduces open-loop poles in the right-half-plan (RHP) and thus causes nonminimum phase characteristics. In consequence, strict gain margin requirements have to be met at the filter resonance frequency and the critical frequency to ensure system stability [51], [52].

In regard to the virtual impedance, it is crucial to retain positive equivalent resistance ensuring minimum phase behavior in a wide frequency range for lenient gain margin requirements. Accordingly, stability and robustness of the system can be enhanced regardless of variations in grid impedance. Many studies have been done in order to extend the frequency range where positive equivalent resistance is achieved [53]–[65], and they can be categorized into two schemes. One type of the strategies which have been reported is to reduce the digital control delays. Shifting the sampling instants toward the PWM reference update instants and multiple sampling by increasing the sampling frequency have been performed for that sake. Nonetheless, the methods suffer from aliasing and unwanted switching noise distortion [53],

[54]. The other solution is adoption of a model-based observer [55], [56] or a phase-lead compensator [57]–[65] to compensate for the digital control delays. However, it is revealed that these methods are able to compensate for a maximum delay of a half-sampling period, implying the positive equivalent resistance is extended up to $f_s/4$. Besides, the methods do not have robustness enough to deal with grid impedance variations.

In accordance with the suggested methods, for the sake of a stable grid-connected inverter operation, a linear PI current controller can be applied with active damping, but incorporating varying grid impedance into the controller design is very challenging. As a superb way of mitigating the adverse effects resulting from time-varying grid impedance, MPC in which the dynamics of an LCL filter are decoupled is considered as a promising solution. Within the bandwidth of MPC, an inverter and the LC part of a filter can be treated as an ideal controlled voltage source [48]. Thus, the system for current control can be reduced to a system consisting only of the grid-side filter inductor and grid impedance. Consequently the simplified system allows for ease of controller design with a linear PI controller in the synchronous reference frame or a PR controller in the stationary reference frame.

1.3 Dissertation Objectives

The object of this research is to design a robust control system for a BTB converter, especially a three-phase inverter connected to a grid, which is apt to become unstable due to resonance from an LCL filter and grid impedance variations. The controller should ensure robust performance in steady-state and dynamic response. The developed control scheme is then applied to the two BTB converters, a variable-voltage variable-frequency (VVVF) and regenerative drives, at the National Center for Reliable Energy Power Transmission Center

(NCREPT). Once the installed linear PI control scheme which has a very small bandwidth causing very slow dynamic response of the system is replaced by the developed control, the inverters' improved static and dynamic performance enhances stability margin of the microgrid system and in return raise its power-rating capacity.

Furthermore, dynamics of a control system in a grid-tied VSI becomes more complex when connected to a weak grid. The large grid impedance of a weak grid is liable to deteriorate the stability and effectiveness of a once-designed current controller for a grid-tied VSI with an LCL filter. Therefore, it is an important task to make the control system be robust not only against grid impedance variations but also against a weak grid condition.

As DG penetration has increased, use of reactive power injection to grids continues to grow to support grid voltage and to diminish the possibility of voltage collapse. Advanced grid ancillary services in the near future will demand negative sequence current injection when needed and rated current to take the most out of reactive power injection. In this regard, adequate and robust control schemes should be developed to meet the improved service requirements. Furthermore, it is aimed that injected current should be controlled within quality specifications at any instant to avoid disconnection from a grid.

As an alternative to linear PI-based control, MPC is deemed to have several advantages and potential abilities to cope with complex resonance effects resulting from an LCL filter connected to a grid-tied inverter. Additionally, varying grid impedance which is a very arduous factor for controller design can be taken into account by decoupling the dynamics of an LCL filter in MPC strategy. MPC is also expected to allow for easy compensation of nonlinear effects, such as time delays and keep the ability of prioritizing fast and assured dynamic performance

under disturbed conditions. It is vital that developed control schemes for an inverter should deal with not only the resonance issues and ancillary services but also nonlinear effects.

1.4 Dissertation Organization

First, LCL filter design for a grid-connected VSI is investigated in chapter 3. A variety of damping methods, passive, filter-based, and state-feedback-based active damping, for enhancing the internal stability are subsequently discussed. Furthermore, design of a control system including capacitor-current-feedback active damping is studied in chapter 5. An a priori Kalman estimator is designed and incorporated into the active damping system in order to compensate for the computation time delay in the digitally controlled system. In addition, an active damping system employing an a posteriori Kalman estimator is compared to the capacitor-current-feedback active damping system in chapter 6. Subsequently, simulation results using Matlab/Simulink are discussed for three different types of active damping methods. They are capacitor-current-feedback active damping, capacitor-current-estimate-feedback active damping using the a posteriori Kalman estimator, and one-sample-ahead capacitor-current-estimate active damping utilizing the a priori Kalman estimator. As a promising approach, MPC is also introduced and implemented for a VSI with an LCL filter system. Conclusions are made in chapter 8.

CHAPTER 2 BACKGROUND

2.1 Introduction

This chapter offers a brief description and background of the microgrid system and the BTB converters in the system at NCREPT. It introduces the BTB converters in more detail and highlights the roll of the converters in the microgrid. In addition, a brief discuss of the direct-quadrature-zero ($dq0$) transformation is given. Useful equations which explicitly give the direct axis and quadrature axis components are derived for a balanced three phase system. The $dq0$ transformation is utilized to transform the alternating current states to direct current, which simplifies the analysis and controller development.

2.2 NCREPT Microgrid System Overview

The NCREPT is a \$5million test facility, which is at the Arkansas Research and Technology Park along with the University of Arkansas Engineering Research Center (ENRC). This facility was built in 2005 as a result of the 2003 Northeast Blackout and has ever since used for research into investigating advanced power electronics solutions for the electric power grid



Figure 2.1. NCREPT test facility building at the Arkansas engineering research center [66].

and transportation applications. In Figure 2.1, two photographs show NCREPT building, the service entrance transformer and the facility transformers.

The facility transformers are utilized for the microgrid testbed configuration. Fig. 5 shows a one-line diagram schematic representing the microgrid testbed, and in Fig. 6 the bay area inside the facility is shown. NCREPT serves as a cost-effective test facility for universities, businesses and national labs with a pay-per-use structure. Research areas include but are not limited to designing and testing of advanced solid-state solutions for control technologies with a focus on grid reliability, power interface applications, transportation such as automotive and aerospace, and energy exploration. Other centers associated with NCREPT are the grid-connected advanced power electronics systems (GREPES), the vertically integrated center for transformative energy research (VICTER) and the high density electronic center (HiDEC). A microgrid testbed has been built at NCREPT to promote research in the areas of microgrid, smart-grid systems, and distributed energy integration to the grid [66].

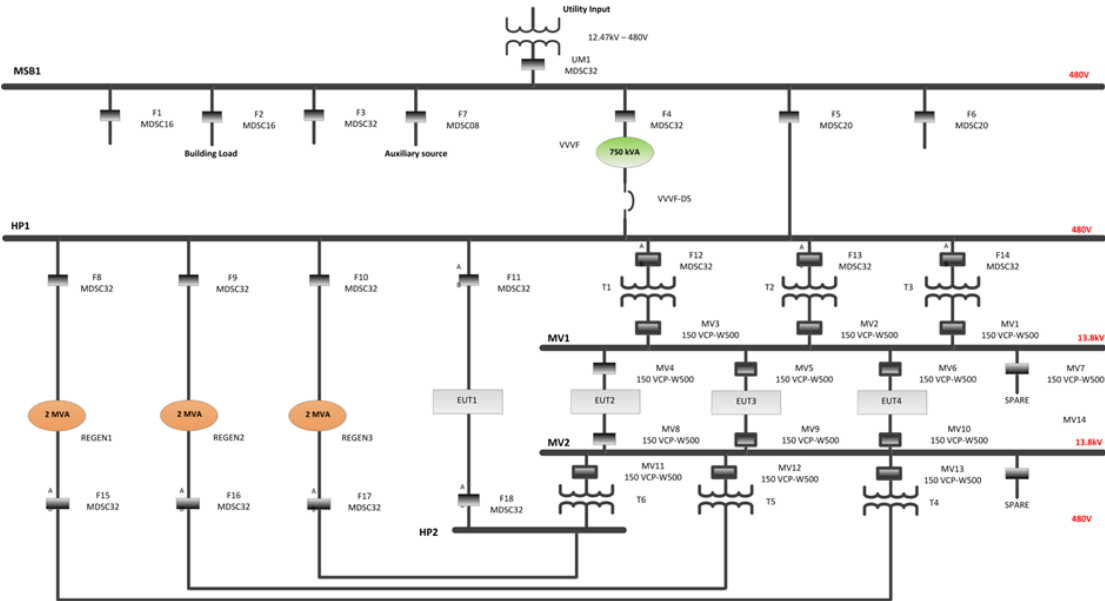


Figure 2.2. NCREPT one-line diagram [66].

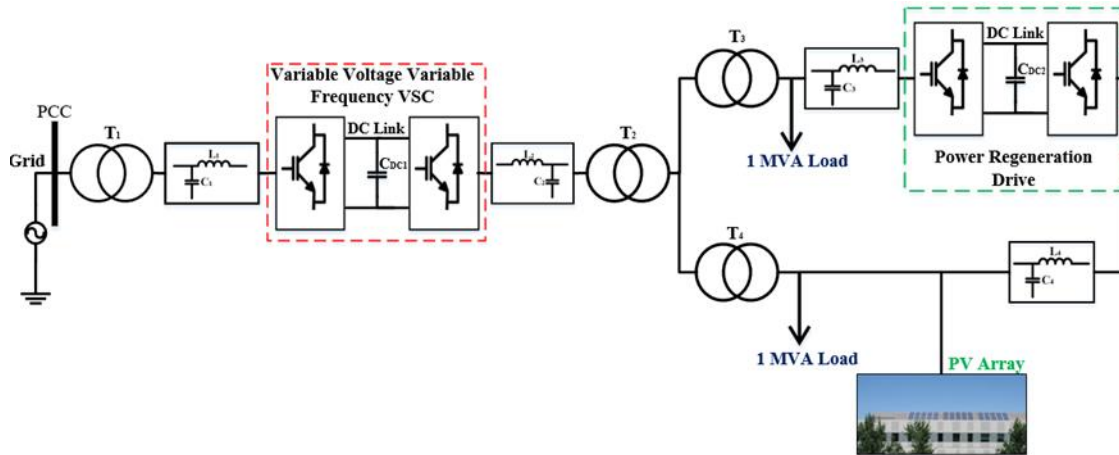


Figure 2.3. Cascaded converters-based microgrid system [66].

The NCREPT facility is designed to allow different microgrid configurations and can therefore be used to test many types of devices and designs, for instance, an AC microgrid shown in Figure 2.2 and an ac-dc hybrid one.

This research focuses on control system design for the two inverter systems of the BTB converters in the microgrid at NCREPT. A few modifications have been made to the microgrid in order to concentrate on the inverters operation. A photovoltaic array (PV) system has been added as a backup power source and two loads have been connected to the microgrid. The resulting modified microgrid is shown in Figure. 2.3. A per-phase equivalent circuit of the microgrid system is depicted in Figure 2.4. The PV array and its output inverter are modelled as a three-phase current source for simplicity. This analysis assumes that the PV array system constitutes an independent stable source capable of supplying a given power to the rest of the system. In addition, each load and the adjacent shunt capacitor forming an LC filter are modelled in Figure as a parallel shunt RC circuit. Table 2.1 summarizes the equivalent overall component values for the circuit demonstrated in Figure 2.4, and appendix A provides the details for these components and their

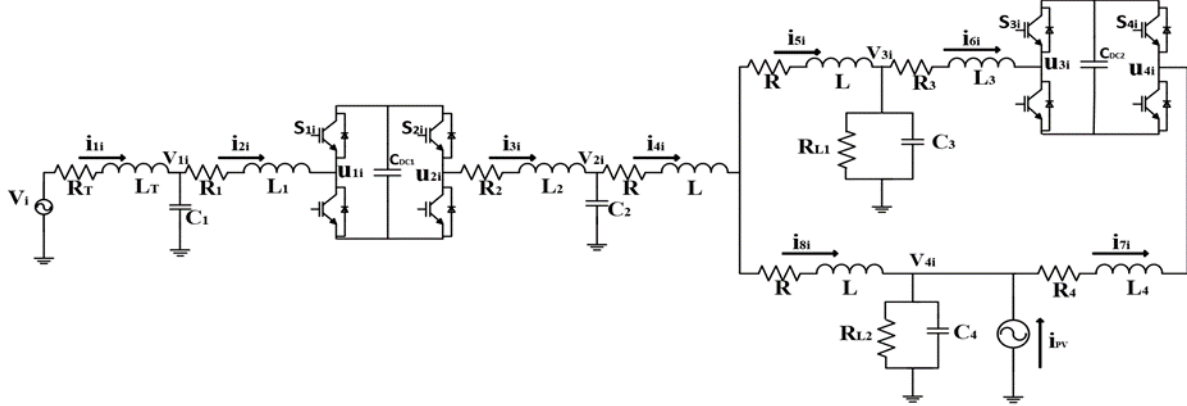


Figure 2.4. Single-phase equivalent circuit for the modified microgrid [66].

Table 2.1. System Component and Parameter Values [66]

Component	Symbol	Nominal Value		Component	Symbol	Nominal Value		
Service XFR	R_T	0.23	m Ω	3 MV XFR	R	0.23	m Ω	
	L_T	6.1	μ H			L	6.1	μ H
LC Filter 1	R_1	207	m Ω	LC Filter 4	R_4	3.8	m Ω	
	L_1	110	μ H			L_4	20	μ H
	C_1	2880	μ F			C_4	1440	μ F
LC Filter 2	R_2	207	m Ω	Load 1	R_{L1}	0.23	Ω	
	L_2	110	μ H	Load 2	R_{L2}	0.23	Ω	
	C_2	2880	μ F	VVVF dc-link cap.	C_{dc1}	25200	μ F	
LC Filter 3	R_3	3.2	m Ω	Regen dc-link cap.	C_{dc2}	37800	μ F	
	L_3	20	μ H	System frequency	Ω	120π	rad/s	
	C_3	1440	μ F	System voltage	V_{RMS}	480	V	

arrangement on the physical system at NCREPT.

The back-to-back converter topology of both the regenerative (REGEN) and the variable-voltage variable-frequency (VVVF) drives are shown in Figure 2.5.

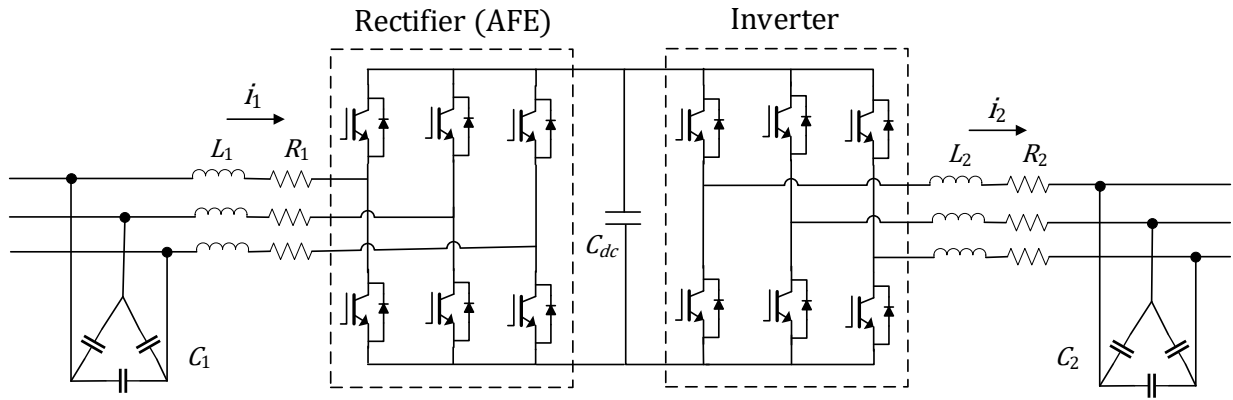


Figure 2.5. Back-to-back topology for the regenerative and the variable-voltage variable-frequency drives [66].

2.3 Direct-Quadrature-Zero ($dq0$) Transformation

The well-known $dq0$ transformation constitutes a mathematical transmutation, which is often used to simplify the analysis of three-phase quantities (voltages, currents, fluxes, etc...). The transformation is accomplished through a mathematical projection of the three-phase phasors onto a rotating reference frame such as it is shown in Fig. 9. The transformation results in two non-zero constants (d and q) and one zero component if the reference frame rotates at the same frequency as that of the three-phase quantities and if the latter are balanced. It is important to note that the $dq0$ transformation differs from the Park's one in that the former is power invariant and the latter is not. However, for the following mathematical derivations Park's transformation is used for simplicity since they only differ by a constant multiplicand.

2.3.1 Direct Transformation: abc to $dq0$

For a balanced voltage triple phase system, the transformation of a, b and c quantities is given by Equation (2.1) [24].

$$\begin{bmatrix} x_d \\ x_q \end{bmatrix} = \frac{2}{3} \begin{bmatrix} \cos(\theta) & \cos(\theta - \frac{2\pi}{3}) & \cos(\theta + \frac{2\pi}{3}) \\ -\sin(\theta) & -\sin(\theta - \frac{2\pi}{3}) & -\sin(\theta + \frac{2\pi}{3}) \end{bmatrix} \begin{bmatrix} x_a \\ x_b \\ x_c \end{bmatrix} \quad (2.1)$$

where $\begin{cases} x_a = X_p \cos \theta_g \\ x_b = X_p \cos(\theta_g - \frac{2\pi}{3}) \\ x_c = X_p \cos(\theta_g + \frac{2\pi}{3}) \end{cases}$ and θ_g is the grid angle.

It follows from (2.1) that:

$$\begin{aligned} x_d &= \frac{2}{3} \left(\cos \theta x_a + \cos\left(\theta - \frac{2\pi}{3}\right) x_b + \cos\left(\theta + \frac{2\pi}{3}\right) x_c \right) \\ &= \frac{2}{3} \left(X_p \cos \theta \cos \theta_g + X_p \cos\left(\theta - \frac{2\pi}{3}\right) \cos\left(\theta_g - \frac{2\pi}{3}\right) + X_p \cos\left(\theta + \frac{2\pi}{3}\right) \cos\left(\theta_g + \frac{2\pi}{3}\right) \right) \\ &= \frac{2}{3} \left(\frac{2}{3} \left(3 \cos(\theta - \theta_g) + \cos(\theta + \theta_g) + \cos\left(\theta + \theta_g - \frac{4\pi}{3}\right) + \cos\left(\theta + \theta_g + \frac{4\pi}{3}\right) \right) \right) \\ x_d &= \frac{2}{3} \left(\frac{3X_p}{2} \cos(\theta - \theta_g) \right) = X_p \cos(\theta - \theta_g) \end{aligned} \quad (2.2)$$

$$\begin{aligned} x_q &= \frac{2}{3} \left(-\sin \theta x_a - \sin\left(\theta - \frac{2\pi}{3}\right) x_b - \sin\left(\theta + \frac{2\pi}{3}\right) x_c \right) \\ &= \frac{2}{3} \left(-X_p \sin \theta \cos \theta_g - X_p \sin\left(\theta - \frac{2\pi}{3}\right) \cos\left(\theta_g - \frac{2\pi}{3}\right) - X_p \sin\left(\theta + \frac{2\pi}{3}\right) \cos\left(\theta_g + \frac{2\pi}{3}\right) \right) \\ &= \frac{2}{3} \left(-\frac{X_p}{2} \left[3 \sin(\theta - \theta_g) + \sin(\theta + \theta_g) + \sin\left(\theta + \theta_g - \frac{4\pi}{3}\right) + \sin\left(\theta + \theta_g + \frac{4\pi}{3}\right) \right] \right) \\ x_q &= \frac{2}{3} \left(-\frac{3X_p}{2} \sin(\theta - \theta_g) \right) = -X_p \sin(\theta - \theta_g) \end{aligned} \quad (2.3)$$

The phase difference is constant if both θ and θ_g have the same frequency, and it is given by Equation (2.4). Where θ is the rotation angle for the rotating reference frame, and θ_g is the electrical angle of the three-phase quantities. In this case, both the direct axis component x_d and the quadrature axis component x_q are constants.

$$\phi = \theta - \theta_g \quad (2.4)$$

2.3.2 Indirect Transformation: abc to $\alpha\beta 0$ and $\alpha\beta 0$ to $dq0$

By using an intermediate transformation, the same results can be obtained.

First, the transformation from abc to $\alpha\beta$ is accomplished using Equation (2.5) as follows:

$$\begin{bmatrix} x_\alpha \\ x_\beta \end{bmatrix} = \frac{2}{3} \begin{bmatrix} 1 & -\frac{1}{2} & -\frac{1}{2} \\ 0 & \frac{\sqrt{3}}{2} & -\frac{\sqrt{3}}{2} \end{bmatrix} \begin{bmatrix} x_a \\ x_b \\ x_c \end{bmatrix}. \quad (2.5)$$

$$\begin{aligned} x_\alpha &= \frac{2}{3} \left(x_a - \frac{1}{2}x_b - \frac{1}{2}x_c \right) \\ &= \frac{2}{3} \left(X_p \cos \theta_g - \frac{1}{2}X_p \cos \left(\theta_g - \frac{2\pi}{3} \right) - \frac{1}{2}X_p \cos \left(\theta_g + \frac{2\pi}{3} \right) \right) = \frac{2}{3} \left(\frac{3}{2}X_p \cos \theta_g \right) \\ &= X_p \cos \theta_g \end{aligned}$$

$$x_\alpha = X_p \cos \theta_g. \quad (2.6)$$

$$\begin{aligned} x_\beta &= \frac{2}{3} \left(0x_a + \frac{\sqrt{3}}{2}x_b - \frac{\sqrt{3}}{2}x_c \right) \\ &= \frac{2}{3} \left(0 + \frac{\sqrt{3}}{2}X_p \cos \left(\theta_g - \frac{2\pi}{3} \right) - \frac{\sqrt{3}}{2}X_p \cos \left(\theta_g + \frac{2\pi}{3} \right) \right) = \frac{2}{3} \left(\frac{3}{2}X_p \sin \theta_g \right) = X_p \sin \theta_g \end{aligned}$$

$$= X_p \sin \theta_g$$

$$x_\beta = X_p \sin \theta_g . \quad (2.7)$$

In the same manner, the transformation from $\alpha\beta$ to dq is accomplished using Equation (2.8) as follows:

$$\begin{bmatrix} x_d \\ x_q \end{bmatrix} = \begin{bmatrix} \cos(\theta) & \sin(\theta) & 0 \\ -\sin(\theta) & \cos(\theta) & 0 \end{bmatrix} \begin{bmatrix} x_\alpha \\ x_\beta \end{bmatrix} . \quad (2.8)$$

$$x_d = \cos(\theta) x_\alpha + \sin(\theta) x_\beta = X_p \cos(\theta) \cos \theta_g + X_p \sin(\theta) \sin \theta_g$$

$$= X_p \left(\frac{1}{2} (\cos(\theta - \theta_g) + \cos(\theta + \theta_g)) + \frac{1}{2} (\cos(\theta - \theta_g) - \cos(\theta + \theta_g)) \right)$$

$$x_d = X_p \cos(\theta - \theta_g) . \quad (2.9)$$

$$x_q = -\sin(\theta) x_\alpha + \cos(\theta) x_\beta = -X_p \sin(\theta) \cos \theta_g + X_p \cos(\theta) \sin \theta_g$$

$$= X_p \left(-\frac{1}{2} (\sin(\theta + \theta_g) - \sin(\theta - \theta_g)) + \frac{1}{2} (\sin(\theta + \theta_g) + \sin(\theta - \theta_g)) \right)$$

$$x_q = X_p \sin(\theta - \theta_g) . \quad (2.10)$$

From the above derivations, it can be concluded that both the direct and indirect transformations yield the same results since (2.2) is the same as (2.9) and (2.3) equals (2.10).

CHAPTER 3 LCL FILTER DESIGN

3.1 Introduction

As power inverters have been widely used to maximize the power transfer from renewable energy sources, it is crucial to maintain the required quality of injected grid current and voltage at the point of common coupling (PCC). In order to meet the required specifications of injected current, a filter is needed at the interface between an inverter and a grid. It reduces harmonics of the output current of the inverter, thereby avoiding grid oscillation or even destabilization of the grid-connected inverter system [67]. A simple series inductor as a filter can be used, but the harmonics attenuation is hardly satisfactory. Furthermore, a high voltage drop across the inductor is inevitable and bulky size of it is another shortcoming [68]. With the reasons, an LCL filter is used in place of a conventional L filter. The LCL filter achieves a greater attenuation compared to the L filter along with cost savings, given the overall weight and size reduction of the components. It leads to good performance in the range of power levels up to hundreds of kilowatts, with the use of small values of inductance and capacitance. The remarkable harmonic attenuation ability of the LCL filter enables the use of lower switching frequencies to meet harmonic constraints as defined by standards such as IEEE-519 and IEEE-1547 [67]. According to the constraints, the preferred properties of an LCL filter are superior current harmonic attenuation, fast dynamic response, low voltage drop across the filter, high power factor, and low volume and weight. In order to design an effective LCL filter it is necessary to have an appropriate mathematical model of the filter, a systematic method for designing the filter, and consideration of passive damping requirements [69].

Several LCL filter design methodologies have been presented and studied in literature. However, only a few research works have tried to develop robust LCL filter designs which are available for different grid conditions such as weak or stiff grids. In fact, grid impedance varies substantially depending on the grid configuration associated with low, medium or high voltage lines, wire length and grid conditions. An inverter output LCL filter gives rise to resonance, which causes in most cases instability of the inverter system. Therefore, stable operation of an inverter followed by an LCL filter is commonly ensured through active damping control. Nonetheless, it is also possible to maintain stable operation of the inverter system without active or passive damping by placing the resonance frequency of the LCL filter in a stable region. This strategy favorably allows simple control with the grid current feedback alone for the inverter system to operate with stability [69].

The aim of this work is to provide a simple, robust, and additionally systematic LCL filter design methodology. The proposed design method is applicable to high power inverters as well as low power ones.

3.2 LCL Filter Mathematical Model

The circuit of a three-phase grid-connected power inverter followed by an LCL filter is presented in Figure 3.1(a). As depicted in this figure, the LCL filter is used to interface between the grid and the inverter. The LCL filter consists of L_i , C_f , and L_o , which are respectively the inverter-side inductance, the capacitance of the filter, and the filter grid-side inductance. The internal resistance of the inverter-side inductor is referred as R_i , and the internal resistance of the filter grid-side inductor is denoted by R_o . The grid impedance comprises the inductive part, L_g and the resistive part, R_g . In addition, the filter grid-side inductance L_o and the inductance of the

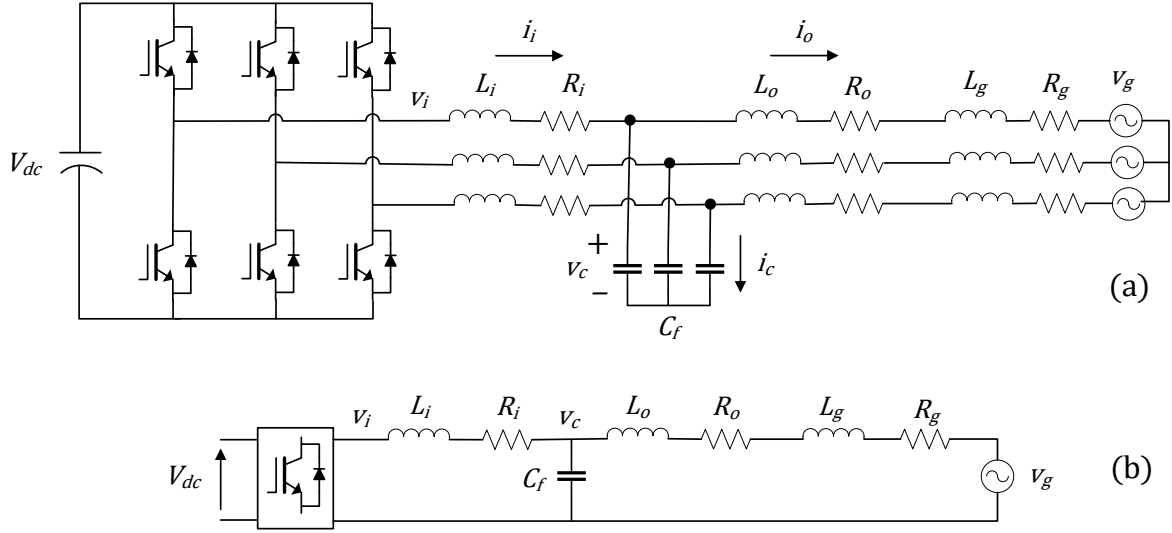


Figure 3.1. (a) A three-phase grid-connected VSI with an LCL filter. (b) Single-phase equivalent circuit.

grid impedance L_g are lumped to be L_o^g . Similarly, the internal resistance of the filter grid-side inductor R_o and the internal resistance of the grid inductor R_g are lumped to be represented by R_o^g .

The equivalent single-phase circuit of the grid-connected inverter with the LCL filter is shown in Figure 3.1(b), where the inverter is supplied with a constant dc voltage V_{dc} . From the figure, the LCL filter equations are obtained as

$$i_i = \frac{v_i - v_c}{L_i s + R_i} \quad (3.1)$$

$$i_o = \frac{v_c - v_g}{L_o^g s + R_o^g} \quad (3.2)$$

$$v_c = \frac{i_c}{C_f s} \quad (3.3)$$

The transfer function for the LCL filter is the relationship between the filter output current i_o and the two input voltages v_i and v_g . The transfer function can be obtained by the superposition principle. The transfer function of the ratio of the filter output i_o to the input v_i is obtained by setting the v_g input equal to zero, given as Equation (3.4). Analogously, with the v_i equal to zero, the ratio of the filter output i_o to the input v_g is found to be Equation (3.5).

$$G_1 = \left. \frac{i_o}{v_i} \right|_{v_g = 0} = \frac{1}{L_i L_o^g C_f s^3 + C_f (L_o^g R_i + L_i R_o^g) s^2 + (R_i R_o^g C_f + L_i + L_o^2) s + R_i + R_o^g}. \quad (3.4)$$

$$G_2 = \left. \frac{i_o}{v_g} \right|_{v_i = 0} = \frac{-(L_i C_f s^2 + R_i C_f s + 1)}{L_i L_o^g C_f s^3 + C_f (L_o^g R_i + L_i R_o^g) s^2 + (R_i R_o^g C_f + L_i + L_o^2) s + R_i + R_o^g}. \quad (3.5)$$

The transfer function between the filter output current i_o and the input voltages v_i and v_g is obtained through superposition of G_1 and G_2 , given as

$$i_o = \frac{L_i C_f v_g s^2 + R_i C_f v_g s + v_i + v_g}{L_i L_o^g C_f s^3 + C_f (L_o^g R_i + L_i R_o^g) s^2 + (R_i R_o^g C_f + L_i + L_o^2) s + R_i + R_o^g}. \quad (3.6)$$

The main objective of the LCL filter is to attenuate the high-order current harmonics resulting from switching action. The equivalent single-phase circuit with the internal resistances of the inductors ignored is represented in Figure 3.2.

An important transfer function is the ratio between the grid current and the input voltage, that is, the output voltage of the inverter, which is expressed by Equation (3.7) with the grid

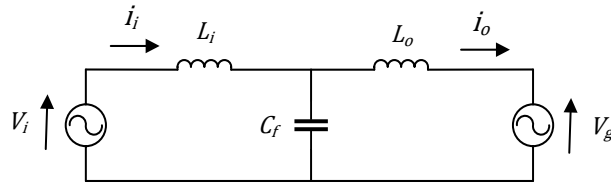


Figure 3.2. Single-phase equivalent circuit without the inductor internal resistances.

voltage being assumed to be an ideal voltage source and neglected. From this equation, the LCL filter resonance frequency, which corresponds to zero impedance, is given by Equation (3.8).

$$G_{LCL} = \frac{i_o}{v_i} = \frac{1}{L_i L_o^g C_f s^3 + (L_i + L_o^g) s}. \quad (3.7)$$

$$\omega_{res}^2 = \frac{L_i + L_o^g}{L_i L_o^g C_f}. \quad (3.8)$$

Damping resistance can be located in series with the filter capacitor. With some algebraic manipulation, the transfer with the damping resistance becomes

$$G_{dLCL} = \frac{i_o}{v_i} = \frac{R_f C_f s + 1}{L_i L_o^g C_f s^3 + R_f C_f (L_i + L_o^g) s^2 + (L_i + L_o^g) s}. \quad (3.9)$$

Since the LCL filter resonance frequency is much lower than the switching frequency, it is reasonable to neglect the capacitor impedance at the switching frequency. Therefore, only the impedance of the inductances, the inverter-side inductance and the lumped one of the filter grid-side inductance and the grid inductance, is seen from an inverter point of view [70]. Based on the approximation, the relationship between the inverter output current i_i and the inverter output voltage v_i is expressed in Equation (3.10). According to Equations (3.7) and (3.10), the transfer function between the grid-injected filter output current i_o and the inverter output current i_i at the far higher frequencies compared to the filter resonance frequency is given by (3.11). At the switching frequency, Equation (3.11) becomes equal to Equation (3.12). As the switching frequency increases away from the filter resonance frequency, the component of the switching frequency is attenuated for the filter output current. This implies that the LCL filter removes the switching frequency component effectively from the filter output current as the switching frequency grows higher above the resonance frequency.

$$\frac{i_i}{v_i} = \frac{1}{(L_i + L_o^g)s}. \quad (3.10)$$

$$\frac{i_o}{i_i} = \frac{i_o v_i}{v_i i_i} = \frac{L_i + L_o^g}{L_i L_o^g C_f s^2 + L_i + L_o^g}. \quad (3.11)$$

$$\left| \frac{i_{osw}}{i_{isw}} \right| = \frac{Z_{LC}^2}{|\omega_{res}^2 - \omega_{sw}^2|}. \quad (3.12)$$

$$Z_{LC}^2 = \frac{L_i + L_o^g}{L_i L_o^g C_f}. \quad (3.13)$$

3.3 LCL Filter Design Methodology

LCL filter design methodology is aimed to meet grid code requirements by efficient attenuation of high-order current harmonic components of the grid-injected current. Therefore, several features should be taken into account in designing an LCL filter such as current ripple, filter size, and switching ripple attenuation.

The following parameters are needed for the LCL filter design: line-to-line rms grid voltage v_g , rated active power P , dc-link voltage V_{dc} , grid frequency f_g , switching frequency of an inverter f_{sw} , which is assumed to be half the sampling frequency f_s .

3.3.1 Resonance Frequency Condition

The filter inductances L_i and L_o can be regarded constant since the currents through the inductors do not exceed their corresponding saturation currents. However, the grid inductance L_g varies under different grid conditions [71]. It also includes the leakage inductance of the transformer. Due to variations in the grid inductance L_g , the resonance frequency caused by the LCL filter has its limits given by Equation (3.14).

$$f_{res_min} = \frac{1}{2\pi} \sqrt{\frac{L_i + L_o + L_{g_max}}{L_i C_f (L_o + L_{g_max})}} \leq f_{res}(L_g) \leq f_{res_max} = \frac{1}{2\pi} \sqrt{\frac{L_i + L_o + L_{g_min}}{L_i C_f (L_o + L_{g_min})}}. \quad (3.14)$$

In order to avoid a resonance problem, the sampling frequency f_s and the grid frequency f_g which have a substantial impact on the degree of resonance intensification should be considered, providing the boundaries shown in Equation (3.15) for the resonance frequency. The resonance frequency should be less than half of the sampling frequency f_s and ten times greater than the grid frequency f_g . This constraint prevents the LCL filter from amplifying switching noises and enables the filter output current to contain only low-order harmonic components.

$$10f_g \leq f_{res_min} \leq f_{res}(L_g) \leq f_{res_max} = \frac{f_s}{2}. \quad (3.15)$$

When PI current control with grid current feedback is employed for an inverter with an LCL filter, two critical frequencies f_{c_min} and f_{c_max} should be taken into consideration for system stability. The minimum critical frequency f_{c_min} is defined to be $f_s/6$, while the maximum critical frequency is equal to $f_s/2$ in Equation (3.16). It is concluded that PI current control with grid current feedback ensures the system to achieve a stable response without active or passive damping when the resonance frequency f_{res} is within the interval $[f_{c_min}, f_{c_max}]$ [72].

$$f_{c_min} = \frac{f_s}{6} \leq f_{res}(L_g) \leq f_{c_max} = \frac{f_s}{2}. \quad (3.16)$$

Consequently, the range of f_{res} variations should be placed within the region shown in Equation (3.17) which is deduced from Equations (3.15) and (3.16).

$$10f_g \leq f_{c_min} < f_{res_min} \leq f_{res}(L_g) \leq f_{res_max} < f_{c_max} = \frac{f_s}{2}. \quad (3.17)$$

3.3.2 Maximum Value of the Total Inductance

The smaller the total inductance of an LCL filter is the better overall system performance becomes. A small inductance value reduces not only line losses but also the voltage drops across the inductors. This improves the speed of response of the system. To this end, the total inductance, L_i plus L_o , is selected to be lower than 0.2 pu as expressed in Equation (3.18), where L_{Tbase} is the base inductance, and Z_{base} is the base impedance shown in (3.19) and (3.20), respectively. Accordingly, the maximum value of the total inductance is expressed in terms of the grid voltage and frequency and the rated active power P .

$$L_{T_max} = (L_i + L_o)_{max} = 0.2L_{Tbase} . \quad (3.18)$$

$$L_{Tbase} = \frac{Z_{base}}{2\pi f_g} . \quad (3.19)$$

$$Z_{base} = \frac{v_{gl-l}^2}{P} . \quad (3.20)$$

$$L_{T_max} = 0.2 \frac{v_{gl-l}^2}{2\pi f_g P} . \quad (3.21)$$

3.3.3 Maximum Value of the LCL Filter Capacitance

The LCL filter capacitor is designed so that the maximum power factor variation seen by the grid is less than or equal to 5%. The reactive power Q_C absorbed by the capacitor is computed by Equation (3.23). Thus, the maximum capacitance value is obtained from Equations (3.22) and (3.24).

$$|Q_C| \leq 0.05|P| . \quad (3.22)$$

$$Q_C = -v_{gl-l}^2 c_f \omega_g . \quad (3.23)$$

$$C_{f_max} = 0.05 \frac{P}{2\pi f_g v_{gl-l}^2}. \quad (3.24)$$

It is noted that when the capacitance value is too low, the inductance values should be very high. Hence, it is recommended to start with a capacitance equal to one half of the maximum value, and then if some of the constraints remain unsatisfied, raise it up to the maximum value.

3.3.4 Minimum DC-Link Voltage

For a fundamental signal at a low frequency, the LCL filter can be approximated to an inductor only configuration since the impedance of the capacitor becomes very high. Accordingly, the LCL filter is represented as an inductor with a value L_T equal to the sum of the two inductance values L_i and L_o with their internal resistances ignored. For the approximated configuration, the relationship between the converter output voltage V_i and the grid voltage V_g is given in Equation (3.25) in complex form.

$$V_i = V_g + jL_T \omega_g I_o. \quad (3.25)$$

The maximum magnitude of the inverter voltage V_{i_max} is obtained by Equation (3.26).

$$V_{i_max} = \sqrt{V_{g_max}^2 + (L_{T_max} \omega_g I_{o_max})^2}, \quad (3.26)$$

where

$$I_{o_max} = \frac{\sqrt{2}P}{3v_g}. \quad (3.27)$$

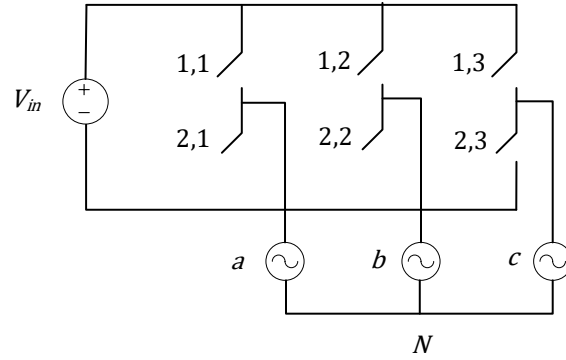


Figure 3.3. Three-phase inverter as a hex bridge.

A three-phase inverter can be drawn as a group of three half bridges to form the hex bridge in Figure 3.3. The switch state matrix $Q(t)$ for this inverter has six elements, $q_{1,1}$ through $q_{1,3}$ and $q_{2,1}$ through $q_{2,3}$. The switches must act in a complementary manner to meet KVL and KCL constraints, such that $q_{1,1} + q_{2,1} = 1$, $q_{1,2} + q_{2,2} = 1$, and $q_{1,3} + q_{2,3} = 1$. In the PWM process, the duty ratios for three-phase sinusoidal modulation are given in Equation (3.28). They must fall between 0 and 1 and need to average 1/2 to avoid any dc component, where m is the amplitude of the modulation depth of the PWM signal [73].

$$\begin{aligned}
 d_{1,1} &= \frac{1}{2} + \frac{m}{2} \cos(\omega t) \\
 d_{1,2} &= \frac{1}{2} + \frac{m}{2} \cos\left(\omega t - \frac{2\pi}{3}\right) \\
 d_{1,3} &= \frac{1}{2} + \frac{m}{2} \cos\left(\omega t - \frac{4\pi}{3}\right)
 \end{aligned} \tag{3.28}$$

Notice that the inverter produces line-to-line output voltages. Given the configuration of the hex bridge, the three-phase line-to-line output voltages are obtained in Equation (3.29).

$$\begin{aligned}
v_{iab} &= q_{1,1}q_{2,2}V_{in} - q_{2,1}q_{1,2}V_{in} \\
&= (q_{1,1} + q_{2,2} - 1)V_{in} \\
v_{ibc} &= q_{1,2}q_{2,3}V_{in} - q_{2,2}q_{1,3}V_{in} \\
&= (q_{1,2} + q_{2,3} - 1)V_{in} \\
v_{ica} &= q_{1,3}q_{2,1}V_{in} - q_{2,3}q_{1,1}V_{in} \\
&= (q_{1,3} + q_{2,1} - 1)V_{in}.
\end{aligned} \tag{3.29}$$

The fundamental frequency moving averages, when the switching frequency is high and the duty ratios are those in Equation (3.28), are obtained given the KCL and KVL constrains [73].

$$\begin{aligned}
\bar{v}_{iab} &= (d_{1,1} + d_{2,2} - 1)V_{in} \\
&= (d_{1,1} + 1 - d_{1,2} - 1)V_{in} \\
&= \left[\frac{1}{2} + \frac{m}{2} \cos(\omega t) - \frac{1}{2} - \frac{m}{2} \cos\left(\omega t - \frac{2\pi}{3}\right) \right] V_{in} \\
&= \frac{m\sqrt{3}}{2} V_{in} \cos\left(\omega t + \frac{\pi}{6}\right) \\
\bar{v}_{ibc} &= (d_{1,2} + d_{2,3} - 1)V_{in} \\
&= (d_{1,2} + 1 - d_{1,3} - 1)V_{in} \\
&= \left[\frac{1}{2} + \frac{m}{2} \cos\left(\omega t - \frac{2\pi}{3}\right) - \frac{1}{2} - \frac{m}{2} \cos\left(\omega t - \frac{4\pi}{3}\right) \right] V_{in} \\
&= \frac{m\sqrt{3}}{2} V_{in} \cos\left(\omega t - \frac{\pi}{2}\right) \\
\bar{v}_{ica} &= (d_{1,3} + d_{2,1} - 1)V_{in} \\
&= (d_{1,3} + 1 - d_{1,1} - 1)V_{in} \\
&= \left[\frac{1}{2} + \frac{m}{2} \cos\left(\omega t - \frac{4\pi}{3}\right) - \frac{1}{2} - \frac{m}{2} \cos(\omega t) \right] V_{in} \\
&= \frac{m\sqrt{3}}{2} V_{in} \cos\left(\omega t - \frac{7\pi}{6}\right)
\end{aligned} \tag{3.30}$$

This describes a three-phase set of voltages. The voltages are also expressed as a set of line-to-neutral voltages.

$$\begin{aligned}
v_{ian} &= \frac{m}{2} V_{in} \cos(\omega t) \\
v_{ibn} &= \frac{m}{2} V_{in} \cos\left(\omega t - \frac{2\pi}{3}\right) \\
v_{icn} &= \frac{m}{2} V_{in} \cos\left(\omega t - \frac{4\pi}{3}\right)
\end{aligned} \tag{3.31}$$

This confirms that a three-phase inverter can deliver three-phase output, controlled by means of PWM and low pass filtered. From the relationship between the input voltage V_{in} and the line-to-neutral inverter output voltages, the dc-link voltage V_{dc_min} is determined based on the maximum magnitude of the inverter voltage V_{i_max} with the amplitude of the modulation depth of the PWM signal m equal to 1, which yields

$$V_{dc_min} = 2V_{i_max} . \tag{3.32}$$

3.3.5 Tuning of the Inverter-Side Inductance

The inverter-side inductance is specifically designed in order to diminish inverter output current ripple. The current ripple results from the pulsed output voltage of the inverter. The maximum current ripple at the inverter output is given by [67]

$$\Delta I_{i_max} = \frac{2V_{dc}}{3L_i} (1 - m)mT_{sw} , \tag{3.33}$$

where m is the amplitude of the modulation depth of the PWM. It can be observed that the maximum peak-to-peak current ripple occurs at $m = 0.5$, then

$$\Delta I_{i_max} = \frac{V_{dc}}{6f_{sw}L_i} , \tag{3.34}$$

where L_i is the inverter-side inductance. A 20% ripple of the rated current for the design parameter is the maximum limit for the inverter output current, which yields

$$\Delta I_{i_max} = 0.2 I_{o_max}, \quad (3.35)$$

where

$$I_{o_max} = \frac{\sqrt{2}P}{3v_g}. \quad (3.36)$$

The minimum inverter-side inductance L_{i_min} obtained based on Equations (3.34) and (3.35) is expressed as

$$L_{i_min} = \frac{V_{dc}}{6f_{sw}\Delta I_{i_max}}. \quad (3.37)$$

3.3.6 Tuning of the Grid-Side Inductance

The grid-side inductance is selected in order to limit the grid current harmonics according to the grid code requirements such that the total harmonic distortion (THD) should be under 5% [69]. The relationship between the inverter-side inductance and the grid-side one can be defined with a parameter r

$$L_o = rL_i, \quad (3.38)$$

where $0 \leq r \leq r_{max}$ and $r_{max} = \frac{L_{T_max}}{L_i} - 1$.

Substituting the grid-side inductance expressed in terms of r and L_i for the L_o and supposing the grid inductance L_g equal to zero in Equation (3.13) yield the harmonic attenuation rate at the switching frequency from Equation (3.12)

$$\delta = \left| \frac{i_{osw}}{i_{isw}} \right| = \frac{1}{|1 + r(1 - L_i C_f \omega_{sw}^2)|}, \quad (3.39)$$

thus

$$r = \frac{1 + \delta}{\delta(L_i C_f \omega_{sw}^2 - 1)}. \quad (3.40)$$

By substituting for r in Equation (3.38), the grid-side inductance L_o is given by

$$L_o = \frac{L_i(1 + \delta)}{\delta(L_i C_f \omega_{sw}^2 - 1)}. \quad (3.41)$$

3.4 LCL Filter Parameter Verification

The current at the input of the LCL filter contains not only a fundamental current but also high frequency harmonics from the switching actions. The objective of the LCL filter is to attenuate these harmonics as much as possible and allow only the fundamental current at the output of the filter. The high frequency harmonics should flow through the low impedance path composed by the filter capacitor rather than flow into the grid. To this purpose, the conditions given by Equations (3.42) and (3.43) must be satisfied for the obtained LCL filter parameters.

For fundamental frequency signals

$$\underbrace{\frac{1}{2\pi f_g C_f}}_{x_{C_f}} \gg \underbrace{2\pi f_g L_o}_{x_{L_o}} \quad (3.42)$$

and for high frequency components

$$\underbrace{\frac{1}{2\pi f_{sw} C_f}}_{x_{C_f}} \ll \underbrace{2\pi f_{sw} L_o}_{x_{L_o}}, \quad (3.43)$$

where X_{C_f} and X_{L_o} are the filter capacitive reactance and the filter grid-side inductive reactance, respectively.

3.5 LCL Filter Design Procedure

The preceding study provides a design procedure for an LCL filter. The specifications are $v_g = 480$ Vrms, line-to-line rms grid voltage; $P = 2$ MW, rated active power; $V_{dc} = 900$ V, dc-link voltage; $\omega_g = 2\pi \times 60$ rad/s, grid angular frequency; $f_{sw} = 4$ kHz, switching frequency; and $\delta = 0.2$ (20 %), attenuation factor. Therefore, a base impedance of 0.12Ω is obtained from Equation (3.20). The fact that the total inductive reactance of an LCL filter should be less than 0.2 pu with respect to the base impedance gives a total inductance of $L_{T_max} = 61 \mu\text{H}$ using Equation (3.21).

- 1) Using 20 % allowed ripple of the rated current, Equation (3.37) gives a minimum inverter-side inductance of $L_{i_min} = 55 \mu\text{H}$.
- 2) The maximum capacitance value is $1,151 \mu\text{F}$ using Equation (3.24). Since a low capacitance value requires a high inductance value, it is recommended to start with about one-half of the maximum value, which is $500 \mu\text{F}$. Subsequently, if some constraints are not met, the capacitance value can be increased up to the maximum limit.
- 3) Selecting a current ripple attenuation of $\delta = 20 \%$ with respect to the ripple on the inverter-side allows L_o to be $20 \mu\text{H}$.
- 4) Substituting the computed parameters $L_{i_min} = 55 \mu\text{H}$, $C_f = 500 \mu\text{F}$, and $L_o = 20 \mu\text{H}$ for L_i , C_f , and L_o in Equation (3.8) gives $f_{res} = 1,859$ Hz, which meets the boundary condition of the resonance frequency by Equation (3.17).
- 5) The two conditions by Equations (3.42) and (3.43) associated with harmonic attenuation of the LCL filter are satisfied with respect to the chosen LCL filter parameter values.

The parameter values for the LCL filter system are presented in Table 3.1.

Table 3.1. Grid-Connected Inverter and LCL Filter System Parameters

Description	Symbol	Value
Rated power	P	2 MW
Grid frequency	f_g	60 Hz
PWM carrier frequency	f_{sw}	4 kHz
Sampling frequency	f_s	8 kHz
Phase grid voltage	V_g	277 Vrms
DC link voltage	V_{dc}	900 V
Inverter-side inductance	L_i	55 μ H
Grid-side inductance	L_o	20 μ H
Filter capacitance	C_f	500 μ F

Based on Equation (3.7) with the parameter values in Table 3.1, the Bode magnitude and phase plots of the filter output grid-side current to the filter input voltage is displayed in Figure 3.4. In addition, the internal resistances of the inductors of the LCL filter can be accounted for and, the transfer function is given

$$G_{LCLR} = \frac{i_o}{v_i} = \frac{1}{L_i L_o^g C_f s^3 + C_f (L_i R_o^g + L_o^g R_i) s^2 + (L_i + L_o^g + C_f R_i R_o^g) s + R_i + R_o^g}. \quad (3.44)$$

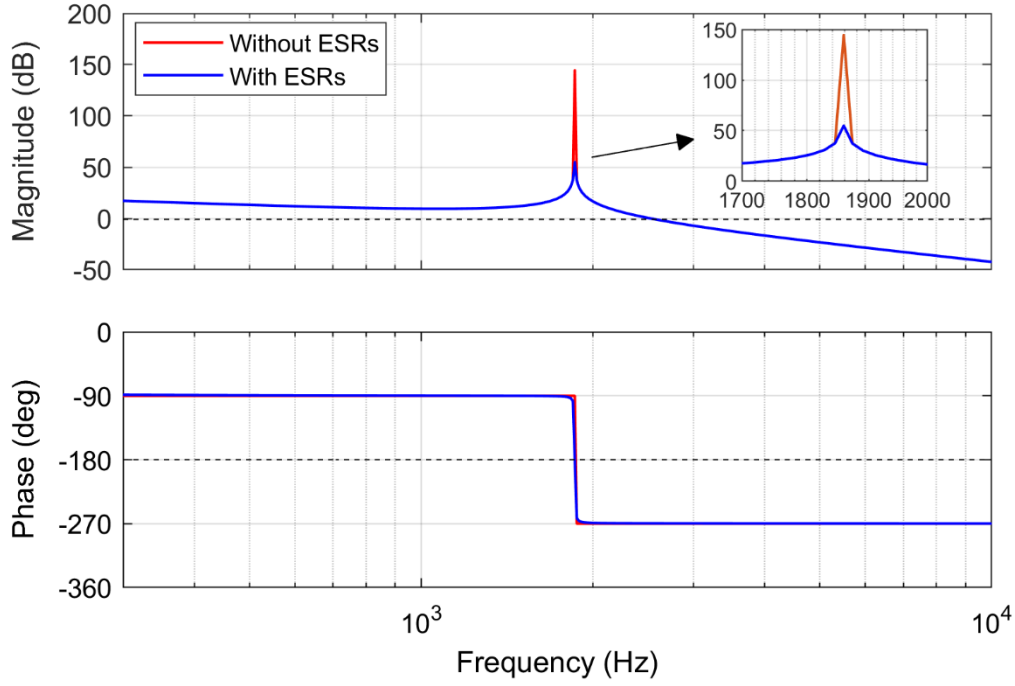


Figure 3.4. Bode magnitude and phase plots for the LCL filter system with or without the internal resistances of the filter inductors.

The transfer function of the LCL filter system with the obtained values substituted for the parameters is given by Equation (3.45). In addition to the parameter values, the internal resistances of the inductors $3.2 \text{ m}\Omega$ and $0.23 \text{ m}\Omega$ for R_i and R_o^g , respectively are plugged into Equation (3.44), and the numerical transfer function is shown in Equation (3.46). In both cases, the grid impedance is neglected.

$$G_{LCL} = \frac{i_o}{v_i} = \frac{1}{5.5 \times 10^{-13} s^3 + 7.5 \times 10^{-5} s}. \quad (3.45)$$

$$G_{LCLR} = \frac{i_o}{v_i} = \frac{1}{5.5 \times 10^{-13} s^3 + 3.83 \times 10^{-11} s^2 + 7.5 \times 10^{-5} s + 0.00343}. \quad (3.46)$$

It is noticeable in the figure that the amplitude of the resonance peak caused by the LCL filter is substantially attenuated by the internal resistances of the inductors. The magnitude

analysis indicates that if the resonance frequency component is contained in the inverter output voltage, then the grid current would include undesirable harmonics.

The resonance frequency of an LCL filter is normally selected at least on the order of 10 times the grid frequency so that the output current should not be excited at the grid frequency. When an inverter input reference signal is pure sinusoidal and a switching frequency is an odd-multiple of the grid frequency, it is advantageous to set the filter resonance frequency at an even-multiple of the grid frequency. This is due to the fact that PWM harmonics predominantly exist at odd-multiple frequencies.

3.6 LCL Filter Design With Robustness Against Grid Impedance Variation

The grid inductance may vary particularly in a weak power system, which can lead to varying LCL resonance frequency. According to Equation (3.14) the minimum resonance frequency f_{res_min} and the maximum resonance frequency f_{res_max} are calculated with the L_{g_max} equal to infinity and the L_{g_min} equal to zero, respectively.

$$f_{res_min} = f_{res}|_{L_g \rightarrow \infty} = \frac{1}{2\pi} \sqrt{\frac{1}{L_i C_f}}, \quad (3.47)$$

$$f_{res_max} = f_{res}|_{L_g = 0} = \frac{1}{2\pi} \sqrt{\frac{L_i + L_o}{L_i L_o C_f}}. \quad (3.48)$$

The inverter-side inductance L_i is determined by Equation (3.37) for the same reason, that is, limiting the ripple amplitude of the inverter output current. When the minimum resonance frequency f_{res_min} is equal to the minimum critical frequency $f_{c_min} = 1,333$ Hz for 8 kHz sampling frequency, it gives the maximum filter capacitance C_{f_max} , which is 259 μ F. Subsequently, the minimum value L_{o_min} is obtained by Equation (3.48) when the maximum resonance frequency is

set equal to the maximum critical frequency f_{c_max} , which is 4 kHz. It is calculated to be $6.88 \mu\text{H}$. By using these conditions along with the LCL filter parameter verification Equations (3.42) and (3.43), the parameter values for the LCL filter can be selected such that the filter resonance frequency is always within the stability region regardless of grid inductance variations.

Table 3.2. Robust LCL Filter Parameters Against Grid Inductance Variation

Description	Symbol	Value
Inverter-side inductance	L_i	$55 \mu\text{H}$
Minimum grid-side inductance	L_{o_min}	$6.88 \mu\text{H}$
Maximum filter capacitance	C_{f_max}	$259 \mu\text{F}$

The displayed bode diagram in Figure 3.4 is the case when the grid impedance is completely neglected. The resonance peak in the magnitude plot implies the maximum resonance frequency for the LCL filter system. It is necessary to take into account when the grid impedance is excessively high, so it is called a weak grid. The definition of a weak grid varies in literature but in most cases a weak grid refers to a low short-circuit ratio (SCR) value. However, defining a specific SCR value for a weak grid is incoherent. Instead, the weak grid SCR values range from 2.5 to 10. This is because different applications and scenarios consider grid strength in many different manners. In context of grid-connected power electronics, a weak grid is often described to have a large grid inductance value. Connection of power electronics to a weak grid is of particular interest, as the grid weakness imposes unexpected challenges for stable operation. In large distribution generation systems or high-voltage dc links, the nominal power may be very

high in comparison with their short-circuit power. Thus, SCR values for such systems are considerably low. These conditions are commonly regarded as ultra weak grids, where the SCR values range from 1 to 2.5 [74].

Assuming the worst case for a grid-connected inverter with an LCL filter, the grid impedance resulting in the SCR equal to 1 can be thought of as the highest possible impedance. Consequently, the grid impedance causes the potential minimum resonance frequency of the system under grid impedance variations. For 2 MW and 60 Hz 480 V line-to-line rms grid voltage, the highest grid impedance is computed to be 0.12 Ω . It is reasonably assumed to be only an inductive reactance, which gives 318 μH . This obtained grid inductance is added to the grid-side inductance to be a lumped inductance L_o^g of 338 μH . The numerical transfer function for this case as shown in Equation (3.49) is obtained by using Equation (3.7).

$$G_{LCL} = \frac{i_o}{v_i} = \frac{1}{4.815 \times 10^{-12} s^3 + 3.93 \times 10^{-4} s}. \quad (3.49)$$

The bode magnitude plot in Figure 3.5 explicitly indicates that as the grid inductance varies from 0 H to 318 μH , which is the highest possible value in practice, the resonance frequency significantly decreases to be close to the theoretical minimum value f_{res_min} of 1,333 Hz. This is calculated by Equation (3.47) with the grid inductance set to infinity. Although this is the extreme case of grid variations, grid impedances actually vary in a wide range. Accordingly, wide-ranging variation in the resonance frequency of any inverter equipped with an LCL filter escalates the likelihood of instable operation. The design of control systems under this condition becomes a challenging task because control interactions is more prominent in weak grid areas. This is due to the fact that each device attempting to control a specific electrical quantity or point

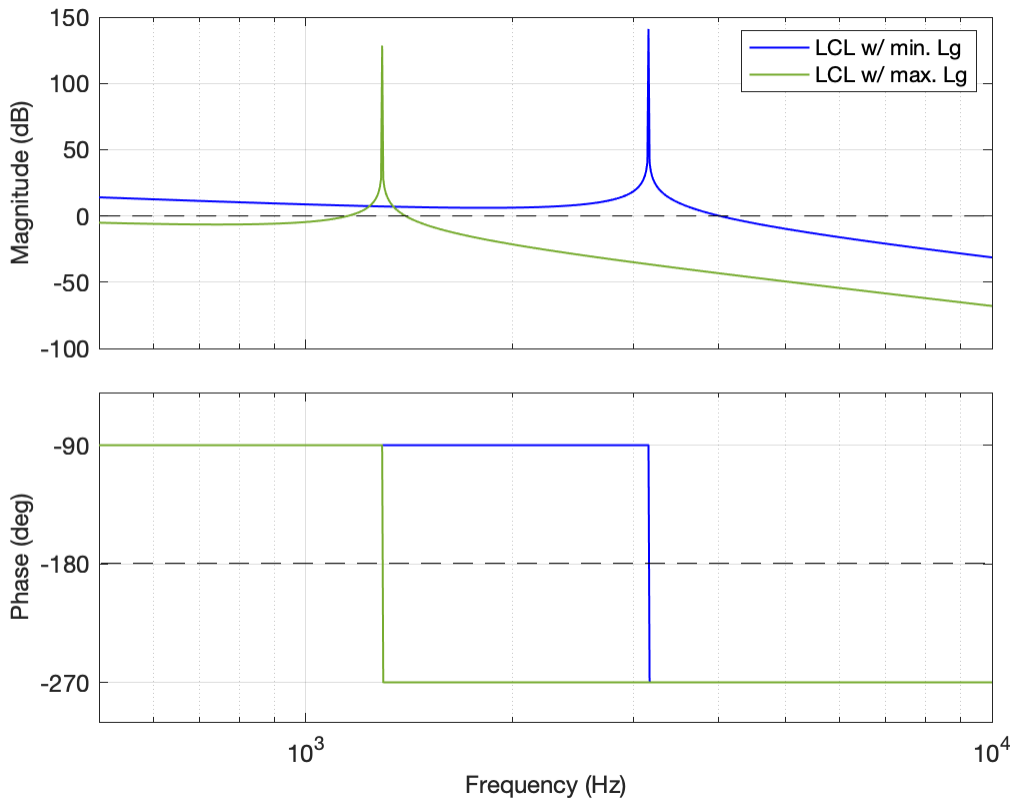


Figure 3.5. Bode diagram of the LCL filter system with the minimum grid inductance or with the maximum grid inductance.

on the bulk power system has more impact on other devices. Conversely, in stiff parts of the system, each device affects insignificantly in changing that quantity on other devices.

CHAPTER 4 DAMPING METHODS FOR INTERNAL STABILITY

4.1 Introduction

It is well known that the stability of the internal current control loop of individual inverter is exacerbated because of a resonance peak caused by an LCL filter being equipped with the inverter. Accordingly, various damping methods are able to be employed to enhance damping of the resonance effect. One category of the methods is passive damping (PD), which involves actual resistors in series or parallel with the LCL filter branches. Filter based damping and state feedback based damping methods are also used. The main disadvantage of PD method applications is inevitable power losses, and the unfavorable factor produced by the latter two damping methods is mainly due to the digital control delay [75].

4.2 Passive Damping Methods

For the purpose of suppressing the LCL filter resonance peak, six typical PD methods can be utilized by adding a resistive element in series or parallel into the individual LCL filter branch as shown in Figure 4.1. Damping resistors R_1 , R_3 , and R_5 are in series with L_1 , C , and L_2

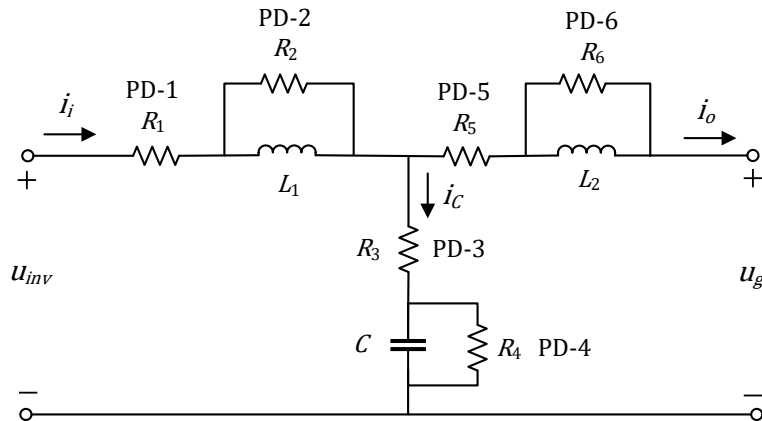


Figure 4.1. Placements of a damping resistor of six typical passive damping methods [75]

respectively. R_2 , R_4 , and R_6 are the damping resistors in parallel with L_1 , C , and L_2 , respectively. Moreover, R_1 and R_5 can be considered as the equivalent resistances of L_1 , and L_2 , respectively.

As for PD-1, PD-2, and PD-3 methods, due to the augmented resistor additional zeros are incorporated into the transfer functions in Table 4.1, which reduces the high frequency attenuation slope compared with that of the undamped LCL filter [76]. The attenuation ability of high frequency harmonics is unaffected for PD-1 and PD-5 methods, whereas the large damping losses are occurred due to the directed path of the power flux through R_1 and R_5 . Meanwhile, the utilization ratio of dc voltage and the dynamic tracking performance are degraded because the low-frequency gain is diminished. Therefore, PD-1 and PD-5 methods are not appropriate for practical application. Besides, relatively large resistances are required in PD-2 and PD-6 to achieve damping, with lessened harmonics attenuation ability. Notably, PD-4 has the best

Table 4.1. Passive Damping Methods and Transfer Functions [75]

Methods	Transfer functions from the LCL filter input voltage to the output current
PD-1	$G_{LCL1} = \frac{i_o}{u_{inv}} = \frac{1}{L_1 L_2 C s^3 + L_2 C R_1 s^2 + (L_1 + L_2)s + R_1}$
PD-2	$G_{LCL2} = \frac{i_o}{u_{inv}} = \frac{L_1 s + R_2}{L_1 L_2 C R_2 s^3 + L_1 L_2 s^2 + R_2 (L_1 + L_2)s}$
PD-3	$G_{LCL3} = \frac{i_o}{u_{inv}} = \frac{C R_3 s + 1}{L_1 L_2 C s^3 + C R_3 (L_1 + L_2) s^2 + (L_1 + L_2)s}$
PD-4	$G_{LCL4} = \frac{i_o}{u_{inv}} = \frac{R_4}{L_1 L_2 C R_4 s^3 + L_1 L_2 s^2 + R_4 (L_1 + L_2)s}$
PD-5	$G_{LCL5} = \frac{i_o}{u_{inv}} = \frac{1}{L_1 L_2 C s^3 + L_1 C R_5 s^2 + (L_1 + L_2)s + R_5}$
PD-6	$G_{LCL6} = \frac{i_o}{u_{inv}} = \frac{L_2 s + R_6}{L_1 L_2 C R_4 s^3 + L_1 L_2 s^2 + R_6 (L_1 + L_2)s}$

filtering performance of the six PD methods, with invariable frequency characteristics, yet the damping losses are relatively high due to the effect of point of common coupling voltages [77].

In terms of power losses, effective damping and filtering performance, PD-3 using a small resistance in series with the capacitor is most appropriate in comprehensive comparison with the other PD methods although its ability of high frequency harmonics attenuation is degraded. The minimum value of R_3 is determined as 20 % of the capacitor impedance at the resonance frequency to make sure sufficient stability margin of the system. In addition, the maximum value of R_3 is chosen as the capacitor impedance at the switching frequency, which ensures effective high frequency harmonics attenuation [78].

The comparison of the appropriate PD methods and the selection conditions of the damping resistances are described in Table 4.2, where ω_r is the resonance angular frequency of the LCL filter, k_p is the proportional coefficient of current controller, and K_{pwm} is the gain of the inverter.

Apparently, the power losses caused by PD-3 are inevitable in any applications. The currents flowing through the damping resistor R_3 can be sorted into the fundamental, switching harmonics, and resonance components. The power losses are mainly due to the fundamental and resonance currents [79]. Based on PD-3, several complex PD methods are suggested to decrease a certain amount of damping losses without losing the high frequency harmonics attenuation ability [75]. This is realized by adding a shunt capacitor or inductor in the capacitor branch. The passive elements are represented in blue in Figure 4.2.

The complex PD shown in Figure 4.2(a) in which a shunt inductor is in parallel with the resistor in the capacitor branch minimizes the power losses caused by the fundamental current.

Table 4.2. Passive Damping Methods and Damping Resistance Selection [75]

Methods	Damping resistance selection
PD-2	$0 < R_2 < \frac{(L_1 + L_2) + \sqrt{(L_1 + L_2)^2 + 4K_{PWM}^2 k_p^2 L_1 C}}{2K_{PWM} k_p C}$
PD-3	$\frac{L_2 f_{sw}}{6\pi L_1 f_r C \omega_r} \leq R_3 \leq \frac{1}{2\pi f_{sw} C}$
PD-4	$0 < R_4 < \frac{L_1 + L_2}{K_{PWM} k_p C}$
PD-6	$0 < R_6 < \frac{(L_1 + L_2) + \sqrt{(L_1 + L_2)^2 + 4K_{PWM}^2 k_p^2 L_2 C}}{2K_{PWM} k_p C}$

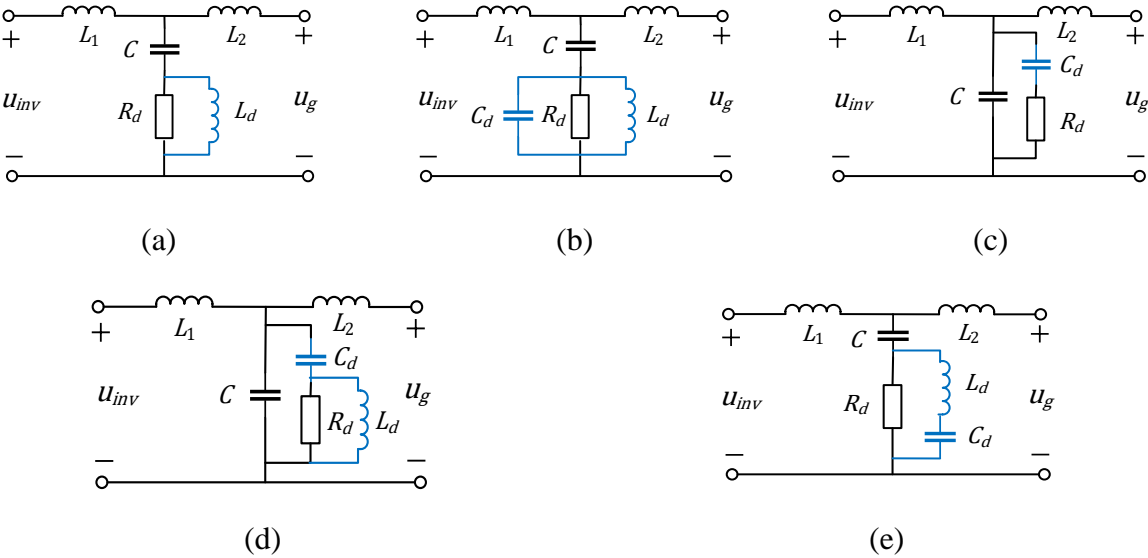


Figure 4.2. Placements of a damping resistor of six typical passive damping methods [75]

This is due to the fact that the inductive reactance of L_d is much less than the resistance of R_d , providing a low impedance path. In addition, the damping resistor R_d should be the dominant path of resonance current to ensure the system damping [78]. The power losses caused by switching frequency current harmonics can be decreased by employing an additional damping capacitor in parallel with the damping inductor shown in Figure 4.2(b). For low damping losses and suitable damping the conditions of $R_d \gg 1/(C_d\omega_{sw})$ and $R_d \ll 1/(C_d\omega_{sw})$ should be met, respectively [78]. The complex method shown in Figure 4.2(c) has the high frequency harmonics attenuation slope of the filter of -60 dB/dec, yet two possible resonance peaks may be induced due to variations in R_d . Moreover, the total capacitance of the complex method should be consistent with the capacitance of the undamped LCL filter [80]. A tradeoff between the damping performance and the power losses can be achieved with the condition $C/C_d = 1$ [81]. In Figure 4.2(d), the fundamental frequency component of the current is bypassed by the L_d and the switching frequency component of the current is bypassed by the C_d . Thus the damping losses on R_d are minimized because the only minor resonance current flows through R_d [79]. In addition, by tuning the damping inductor and capacitor at the switching frequency in Figure 4.2(e), the switching current harmonic is almost bypassed owing to the introduced low impedance path, diminishing the power losses significantly [82].

In summary, in order to reduce the power losses caused by the damping resistor, the fundamental and the switching frequency currents which flow through the damping resistor can be bypassed through the additional damping inductor and capacitor. Nevertheless, the resonance current should be flowed through the resistor branch for sufficient PD, thus the corresponding power losses cannot be avoided. In comparison, the

power losses of the complex PD methods in Figure 4.2(b) and (d) are lowest because of the maximum bypass of current components realized by the additional path. Among the complex methods, employing only an additional capacitor shown in Figure 4.2(c) is easiest to be implemented due to the fact that the consideration of the complicated inductor design is not needed.

Despite of all the advantages, the complex PD methods are not highly preferred due to the overall complexity of circuit topology and parameter design as well as the increased cost and volume of the complex PD LCL filters. Furthermore, the power losses caused by the damping cannot be eliminated completely. Therefore, methods of modifying control algorithm without any additional passive elements and power losses have become increasingly popular in recent years, which ensures the resonance damping and overcome the shortcomings of PD methods.

4.3 Filter-Based Damping Methods

There is a notable approach to attaining the LCL filter resonance peak damping by inserting a digital filter with special functions in the forward path of current control loop. The methods called filter-based active damping. As mentioned previously, the PD causes a decrease of the overall system efficiency due to the power losses. Moreover, it reduces the filter effectiveness since it is very difficult to operate the damping in a selective way at those frequencies where the system actually resonates. Although selective passive damping methods are also possible, the effectiveness of them is uncertain. Active damping is implemented with modification of the controller parameters or the controller structure of a system. It increases the magnitude and phase margins around the resonance frequency [22]. In comparison with the PD

methods, active damping methods are more selective in their action and do not dissipate power. Although they are more sensitive to parameter uncertainties, the sensitivity can be compensated for with an addition of suitable functions to the controller structure.

Digital filter-based active damping methods without any additional passive elements and sensors are introduced. The digital filters mainly used are types of notch filter, low-pass filter, and the all-pass filter. The control block diagram of the filter-based active damping is shown in Figure 4.3, and the close-loop control scheme can be performed with either inverter-side current feedback (ICF) or grid-side current feedback (GCF). The digital filter represented by $F(s)$ shown in Figure 4.3 is normally cascaded to the current controller $G_c(s)$ in the forward path. In general, $G_c(s)$ is a proportional integral (PI) or a proportional resonant (PR) controller, which is implemented in either synchronous reference frame or stationary frame to track the current reference i_{ref} without steady state error. $G_d(s)$ is digital control delay including the sampling and computation process equivalent to a time delay of δT_s ($0 < \delta < 1$) and another time delay of

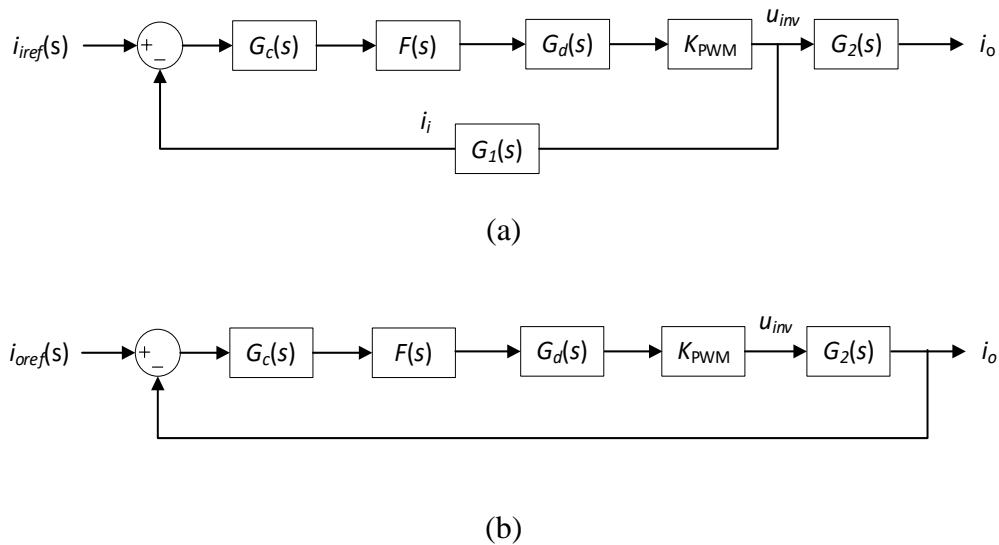


Figure 4.3. Closed-loop current control block diagram of digital filter-based active damping with two current feedback strategies: (a) inverter-side current feedback (ICF) (b) grid-side feedback (GCF).

approximately $0.5T_s$ due to the PWM processing, which can be modeled as a zero-order hold (ZOH) [83]. The gain of the inverter is denoted as K_{PWM} . In Figure 4.3 $G_1(s)$ and $G_2(s)$ are the transfer functions between the inverter output voltage u_{inv} and the inverter-side current i_i and grid-side current i_o , respectively.

4.3.1 Notch Filter

The system structure shown in Figure 3.2 allows the transfer functions of the LCL filter from the inverter output voltage u_{inv} to the inverter output current i_i and to the grid injected current i_o , which are given as

$$G_1(s) = \left. \frac{i_i}{u_{inv}} \right|_{v_g = 0} = \frac{(L_o + L_g)C_f s^2 + 1}{L_i(L_o + L_g)C_f s^3 + (L_i + L_o + L_g)s}, \quad (4.1)$$

$$G_2(s) = \left. \frac{i_o}{u_{inv}} \right|_{v_g = 0} = \frac{1}{L_i(L_o + L_g)C_f s^3 + (L_i + L_o + L_g)s}, \quad (4.2)$$

with $\omega_{res} = 2\pi f_{res}$ being the resonant angular frequency of the LCL filter

$$\omega_{res} = 2\pi f_{res} = \sqrt{\frac{L_i + L_o + L_g}{L_i(L_o + L_g)C_f}}. \quad (4.3)$$

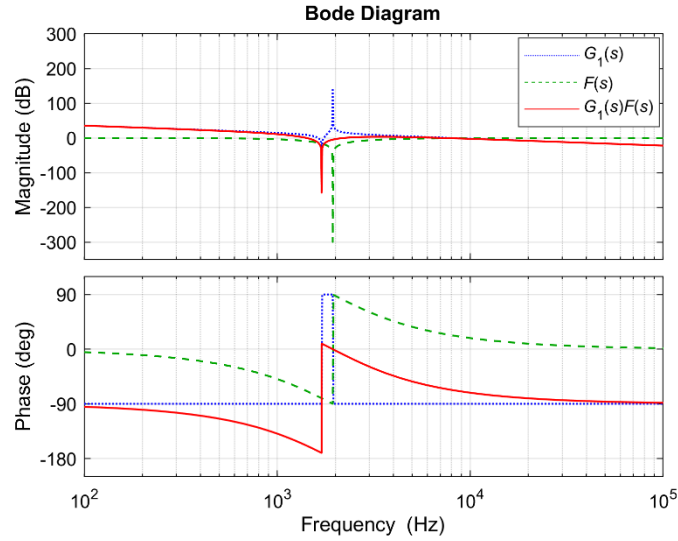
A conventional notch filter corresponding to $F(s)$ in Figure 4.3 has the transfer function

$$F_{notch}(s) = \frac{s^2 + \omega_n^2}{s^2 + qs + \omega_n^2}, \quad (4.4)$$

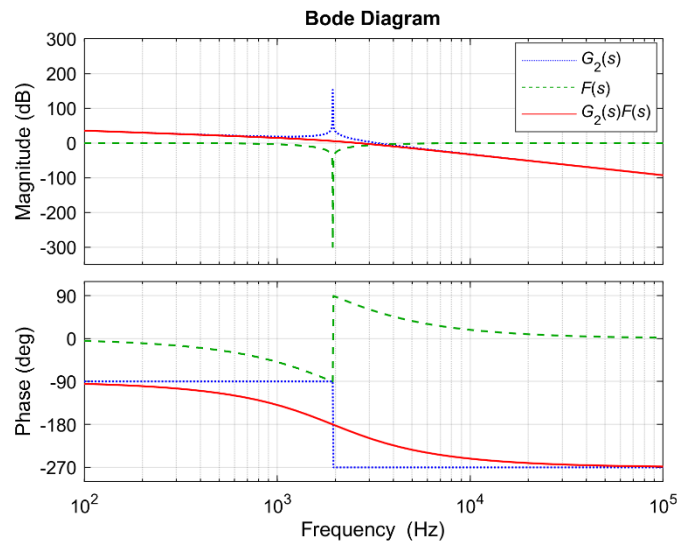
where q is the quality factor of the notch filter determining the 3-dB rejection bandwidth, and $\omega_n = 2\pi f_n$ is the notch frequency. For the purpose of canceling out the resonant peak of a designed LCL filter, the notch frequency is placed at the resonance frequency of the LCL filter (i.e. $\omega_n =$

ω_{res}). Technically, this method is a zero-pole cancellation of system transfer function, in which the zero of a notch filter cancels out the unstable pole of an LCL filter, attenuating the resonance peak of the magnitude frequency curve of the system.

The Bode diagrams of ICF and GCF transfer functions are shown in Figure 4.4, including with and without the notch-filter-based damping method, respectively. The LCL filter consists of L_i , C_f , and L_o , which are $20 \mu\text{H}$, $1,440 \mu\text{F}$, and $6.1 \mu\text{H}$, respectively. According to Equation (4.3), the resonance frequency of the LCL filter is computed to be $1,940 \text{ Hz}$. Without consideration of control time delay, the system employing ICF method without a notch filter is inherently stable since the phase-frequency curve does not cross -180° . In contrast, the system adopting GCF scheme without a notch filter is unstable because the gain magnitude is far above 0 dB at the frequency where the phase-frequency curve crosses downward -180° as shown in Figure 4.4 (b). The notch filter frequency f_n is determined in order to counteract the resonance frequency peak, which results in the condition $f_n = f_{res}$. With this strategy, the added zeros from the notch filter cancel out the unstable poles of the GCF containing the LCL filter. The effect is obviously revealed by the smoothly decreased magnitude-frequency curve of $G_2(s)F(s)$ in Figure 4.4(b). At the same time, the phase curve of the GCF with no notch filter which has a phase change of 180° from -90° to -270° at the resonance frequency of $1,940 \text{ Hz}$ is compensated for by the notch filter. As a result, the phase curve gradually drops from -90° to -270° , which still crosses -180° at the resonance frequency with the magnitude being above 0 dB . However, the gain at the phase crossover frequency can be tuned easily to be below 0 dB by proper adjustment of the controller gain. With the suitably designed controller, the system does



(a)



(b)

Figure 4.4. Bode diagrams of notch-filter-based damping method with two different feedback strategies: (a) inverter-side current feedback (ICF) (b) grid-side feedback (GCF).

not have a -180° crossing with the gain above 0 dB, indicating a stable system according to the Nyquist criterion [83].

However, as is shown in Figure 4.4, the notch filter with a small q has a narrow rejection bandwidth and an almost infinite negative gain around the notch frequency,

which results in high sensitivity to the shift of a resonance frequency. Thus a slight error in the location of the notch frequency can cause a significant loss of the capability to attenuate the LCL filter resonant peak. A self-commissioning notch filter which estimates the resonance frequency and tunes the notch frequency in real time can be employed to enhance the system robustness. However, the accuracy of estimation results highly relies on the system model. Besides, the phase deviation resulting from the notch filter can cause system stability reduction and even instability. Furthermore, the notch effect is also susceptible to the parasitic resistances of the LCL filter. Thus, the internal resistances of the inductors need to be taken into account for the parameter tuning procedure of notch filter. In addition, the notch frequency is subjected to digital implementations of the notch filter. There are two general methods to implement the notch filter in digital control. One is an indirect method in which the filter is designed in the s-domain, and then a discretization method is applied to the designed notch filter, leading to a digital notch filter. Alternatively, a digital notch filter can be designed directly in the z-domain in order to reduce the phase and magnitude errors which are generated by discretizing the s-domain models.

4.3.2 Low-Pass Filter

An intuitive choice for filtering is employing a low-pass filter (LPF) of the first or second order. The transfer function of a second-order LPF is expressed as

$$F_{LPF}(s) = \frac{\omega_n^2}{s^2 + 2D\omega_n s + \omega_n^2}, \quad (4.5)$$

where ω_n is the natural frequency and D is the damping coefficient, usually chosen to be $1/\sqrt{2}$.

As for low-pass filters, the selection of the cutoff frequency is not only a crucial task but also a

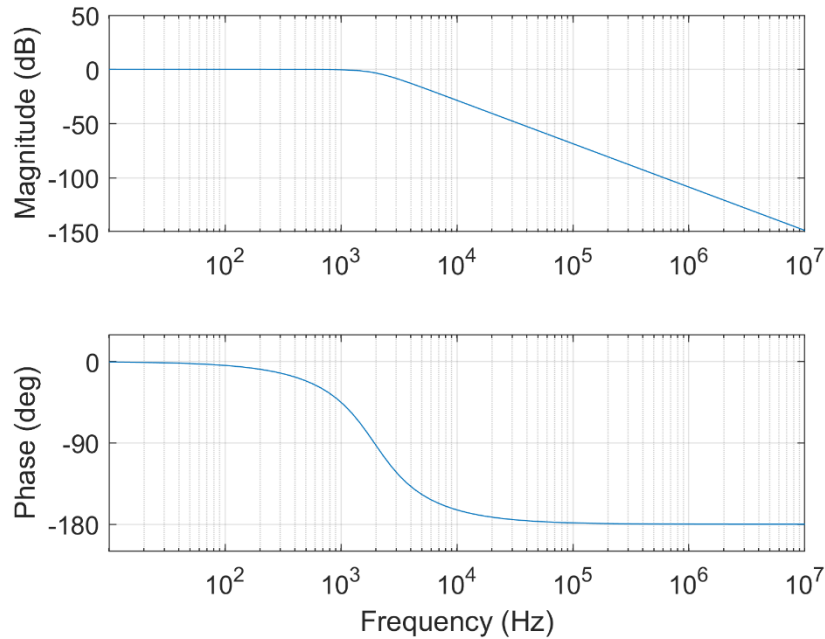


Figure 4.5. Bode diagram of the low-pass filter of which cutoff frequency is located at the LCL filter resonance frequency.

tradeoff between the control bandwidth and the stability margin of the system. For the LCL filter resonance damping, the cutoff frequency of a LPF can be selected to be placed at the LCL filter resonance frequency of 1,940 Hz shown in Figure 4.5. The phase curve falls from 0° and crosses -90° at the cutoff frequency. Once it reaches to -180° , it remains unchanged. Typically, system stability suffers from a phase lag which is introduced by low-pass filtering. However, in the case where resonance damping is required, a phase lag caused by a LPF can make contribution to proper damping for the system with GCF. The essence of the resonance damping by employing the LPF is to shift the phase-frequency curve of the system outside of the unstable frequency region where the gain is below zero, thereby stabilizing the entire system.

Nonetheless, the cutoff frequency restrains the bandwidth in closed-loop operation. As the resonance frequency becomes close to the desired closed-loop bandwidth, the resonance damping effect resulting from the low-pass filter diminishes.

4.3.3 All-Pass Filter

A proper phase lag which increases the phase margin of the system at the resonance frequency can be introduced by an all-pass filter. Nevertheless, the use of the filter brings about the degradation of the dynamic performance and robustness of the system. The general equation of the all-pass is given.

$$F_{all-pass}(s) = e^{j\phi_d}, \quad (4.6)$$

where ϕ_d is the phase lag introduced by the all-pass filter.

From the aforementioned applications of the three different filter-based damping methods, a comprehensive comparison is conducted to illustrate their merits and drawbacks. The notch filter leads to superior damping performance as well as simple implementation. However, it is considerably sensitive to variations in the resonance frequency of an LCL filter. In addition, the internal resistances of the inductors should be taken into account for tuning process. The application of the LPF ensures stability for the system with grid current feedback and robustness against the grid parameter variations. It also has drawbacks in regard to the closed-loop bandwidth. The cutoff frequency of the LPF limits the control bandwidth. Furthermore, the closer to the closed-loop bandwidth the resonance frequency becomes the less the resonance damping effect becomes. The sufficient damping requires a proper phase lag resulting from the judicious selection of the cutoff frequency. As for the all-pass filter, high frequency noise is not amplified, and the controller design is relatively simple. However, degraded transient

performance and aggravated system robustness are hardly avoided. In comparison, the notch filter is thought to be more effective due to the considerable suppression performance with respect to the resonance peak. The other methods relying on the phase lead or phase lag are more complicated to be implemented because the phase lead or phase lag should be carefully incorporated into the system.

4.4 State Feedback-Based Damping Methods

In addition to the primary control variables of closed-loop which are used to decrease the steady state error of the system, an extra state variable can also be fed back for the purpose of the system damping. In the inverter system equipped with the LCL filter shown in Figure 3.2, the available supplemental feedback variable for the system damping can be the capacitor current, the capacitor voltage, the inverter-side current or the grid-side current. The control block diagrams of the system with different state feedback are shown in Figure 4.6. In the figure, G_{ad_ic} , G_{ad_uc} , G_{ad_ii} , and G_{ad_io} are feedback gain to adjust the damping effect. The two transfer functions of $G_{ic}(s)$ and $G_{uc}(s)$ are the ratio of the capacitor current, i_C , to the inverter output voltage, u_{inv} , and the capacitor voltage, u_C , to the inverter output voltage, u_{inv} , respectively. The transfer functions are expressed as

$$G_{ic}(s) = \frac{i_C}{u_{inv}} = \frac{1}{sL_i} \frac{s^2}{s^2 + \omega_r^2}, \quad (4.7)$$

$$G_{uc}(s) = \frac{u_C}{u_{inv}} = \frac{1}{L_i C_f} \frac{1}{s^2 + \omega_r^2}, \quad (4.8)$$

where ω_r is the resonance angular frequency of the LCL filter. It is noteworthy that the state feedback-based damping is equivalent to virtual impedance-based damping where the impedance

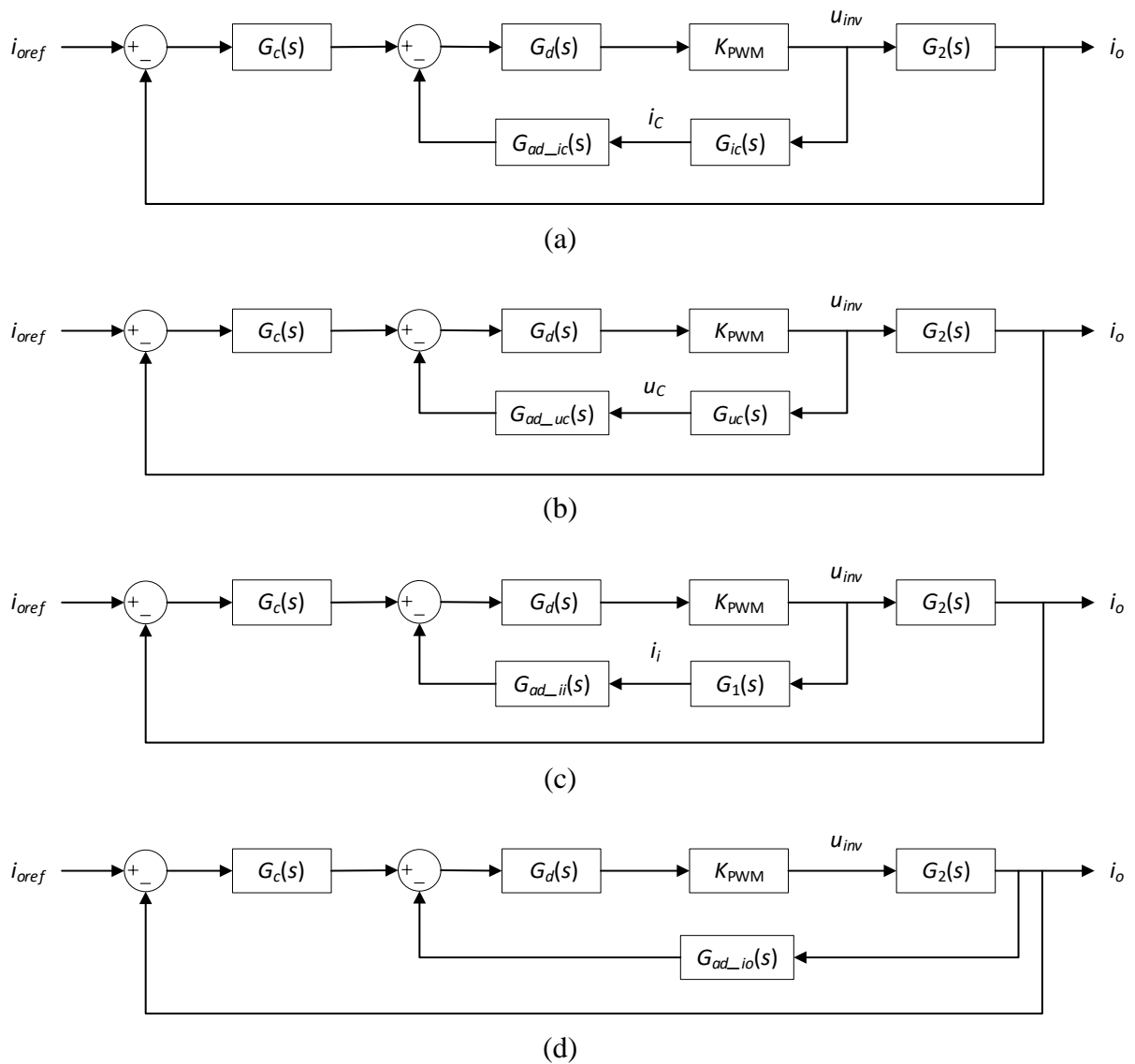


Figure 4.6. Block diagrams of various state feedback-based damping methods: (a) capacitor current feedback, (b) capacitor voltage feedback, (c) inverter-side current feedback, and (d) grid-side current feedback.

is in series or parallel with the LCL filter branch. Therefore, the different state feedback and its corresponding virtual impedance are investigated together.

4.4.1 Capacitor Current Feedback

The system can be stabilized due to the dampened resonance peak resulting from capacitor current feedback which is adjusted by the proportional gain, G_{ad_ic} [84]. In this scenario, the capacitor current feedback is equivalent to adding a virtual impedance in parallel with the filter capacitor. The virtual impedance can be expressed in terms of the feedback proportional gain, the inverter gain, the control delay, and the elements of the LCL filter as follows [85], [86]:

$$Z_{ic}(s) = R_{ic} // jX_{ic} = \frac{L_i}{K_{PWM}C_f G_{ad_ic} G_d(s)}. \quad (4.9)$$

The virtual reactance, X_{ic} , have an effect on the shift of the LCL filter resonance peak [85], [86], and the virtual resistance play a role in damping the resonance peak. Nonetheless, the active damping can be invalid when the virtual resistance, R_{ic} , has a negative characteristic. This phenomenon occurs when the resonance peak is located above the critical frequency that is subjected to the sampling frequency. In order to solve the instability issue, various approaches such as the adoption of PI feedback [87] and the first-order high-pass filter (HPF) feedback [88] have been introduced. When a second-order HPF with R_{ic} gain is employed in place of the proportional gain, the capacitor current feedback becomes equal to a virtual pure resistor R_{ic} in series with the filter capacitor [89]. However, the approximate derivative characteristics of the HPF deteriorate the high-frequency noise, and the control algorithm becomes considerably complicated [75]. Instead of direct use of the capacitor current for feedback, the first-order derivative of the capacitor voltage which is equivalent to the capacitor current can be used. It also emulates a virtual impedance in parallel with the filter capacitor. However, the direct derivative operation is not only ineffective but also burdensome in digital controllers. Hence, a

HPF or a lead-lag network which performs indirect derivation can be adopted to approximate the direct derivation. Notwithstanding the advantage of the indirect derivation, a large phase error introduced by the HPF and vulnerability of the lead-lag network to weak grids reduce their usefulness.

4.4.2 Capacitor Voltage Feedback

Besides the direct or indirect derivative of the capacitor voltage, proportional feedback of the capacitor voltage can also be used to provide proper resonance damping as shown in Figure 4.6(b). This scheme simulates a virtual resistor in parallel with the filter capacitor [90]. Nonetheless, the effectiveness of this method on resonance damping is quite deficient compared with that of the capacitor voltage derivative feedback.

4.4.3 Inverter-Side Current Feedback

In general, ICF is utilized for overcurrent protection of inverters. The proportional ICF shown in Figure 4.6(c) is feasible to simulate an equivalent virtual impedance in series with the inverter-side inductance [91]. When a first-order HPF is employed for the feedback coefficient, G_{ad_ii} , the expression of the virtual impedance is given as

$$Z_{ii}(s) = R_{ii} + jX_{ii} = K_{\text{PWM}}G_{ad_ii}(s). \quad (4.10)$$

Unfavorably, the feedback might cause additional resonance between the capacitor and the grid-side inductor due to the grid voltage harmonics. Furthermore, the dynamic tracking ability is degraded owing to the decreased low-frequency gain [92].

4.4.4 Grid-Side Current Feedback

The main merit of employing GCF for active damping is that only one current sensor is required for both the grid-injected current tracking and the resonance damping. The LCL filter resonance peak can be attenuated by applying second-order derivative feedback of the grid-injected current. The implementation difficulty of direct derivation can be avoided by application of a first-order HPF with a negative gain in the GCF damping loop [93]–[95]. However, it results in a reduction of the control bandwidth of the system and dynamic performance degradation for the system with low resonance frequency [96], [97]. It is known that the first-order HPF-based damping method emulates a virtual impedance in parallel with the filter capacitor, as follows [98]:

$$Z_{io_HPF}(s) = R_{io_HPF} + jX_{io_HPF} = \frac{L_i L_o s^2}{G_{ad_io}(s) K_{PWM}}. \quad (4.11)$$

Besides, the feedback coefficient G_{ad_io} can also be a second-order generalized integrator (SOGI) with a negative gain, where the GCF is equivalent a virtual impedance in series with the grid-side inductance [99], and the virtual impedance is derived as

$$Z_{io_SOGI}(s) = R_{io_SOGI} + jX_{io_SOGI} = \frac{G_{ad_io}(s) G_d(s) K_{PWM}}{s^2 L_1 C_f}. \quad (4.12)$$

The phase lead characteristics of the SOGI is utilized to achieve the approximate derivative operation.

From the aforementioned state feedback-based active damping methods, four types of placement of the virtual impedances in the LCL filter branches are realized as shown in Figure 4.7. According to the damping effectiveness and the resistor placements of the PD methods, the state feedback methods corresponding to addition of the impedance Z_{V3} in parallel with the

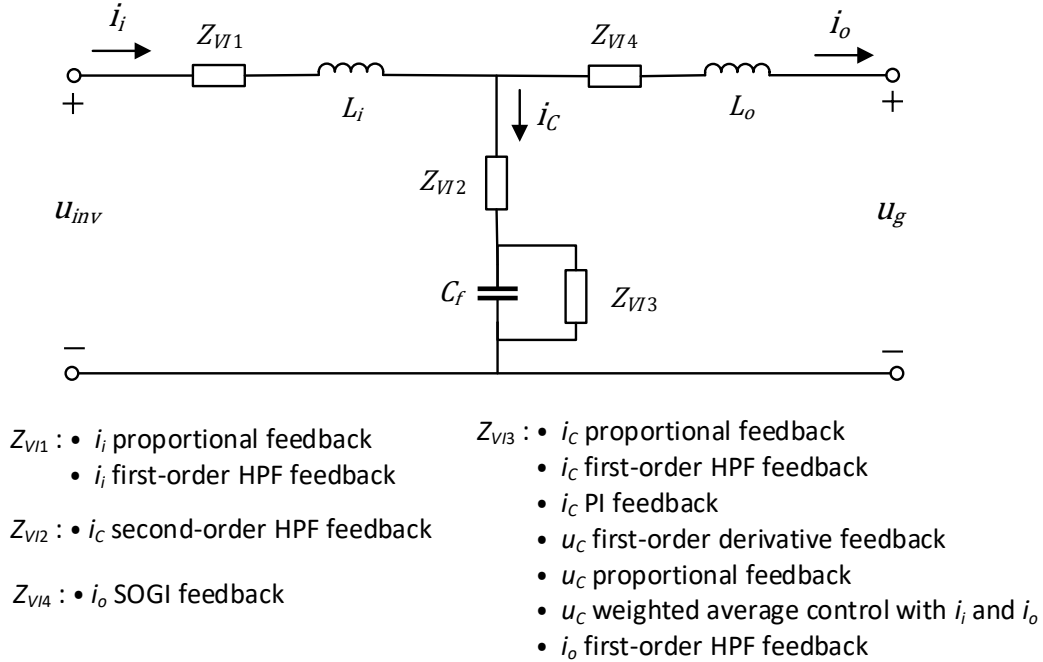


Figure 4.7. Equivalent circuit of state feedback-based damping methods.

capacitor are considered to be most effective. The LCL filter with the virtually added impedance Z_{V13} resulting from the state feedback methods has the same topology structure as that of PD-4 in Figure 4.1.

Among the damping methods relating to Z_{V13} , the derivative feedback of the capacitor voltage has the advantage of lowest hardware cost since it does not require extra current sensor. Nonetheless, its effectiveness is vulnerable to high-frequency noise and voltage distortion at PCC. Moreover, the damping performance is slightly aggravated due to the fact that the approximate derivation is usually utilized in place of the direct derivative feedback. Although the first-order HPF feedback of the grid-injected current is economically attractive, the effectiveness of this method might be obviated by the influence of amplified high-frequency noise. From the detailed comparison, it is concluded that the proportional capacitor current feedback is preferred

and widely used compared to the various state feedback methods. This is due to merits of robust and relatively simple control system and sufficient damping performance [75].

Technically, the single loop ICF can be considered as the virtual impedance in series with the inverter-side inductor. Similarly, the single loop GCF can be regarded as the virtual impedance in parallel with the capacitor of the LCL filter [100], [101]. The digital control delay introduced by algorithm execution has a considerable effect on the characteristics of the virtual resistance. It is worth pointing out that the resonance peak caused by the LCL filter can be damped only under the positive virtual resistance conditions, regardless of any types of damping methods [85].

CHAPTER 5 CONTROL SYSTEM DESIGN WITH ACTIVE DAMPING

5.1 Discrete-Time Model of Active Damping Current Controller

The general structure of a voltage source inverter (VSI) feeding current into a grid

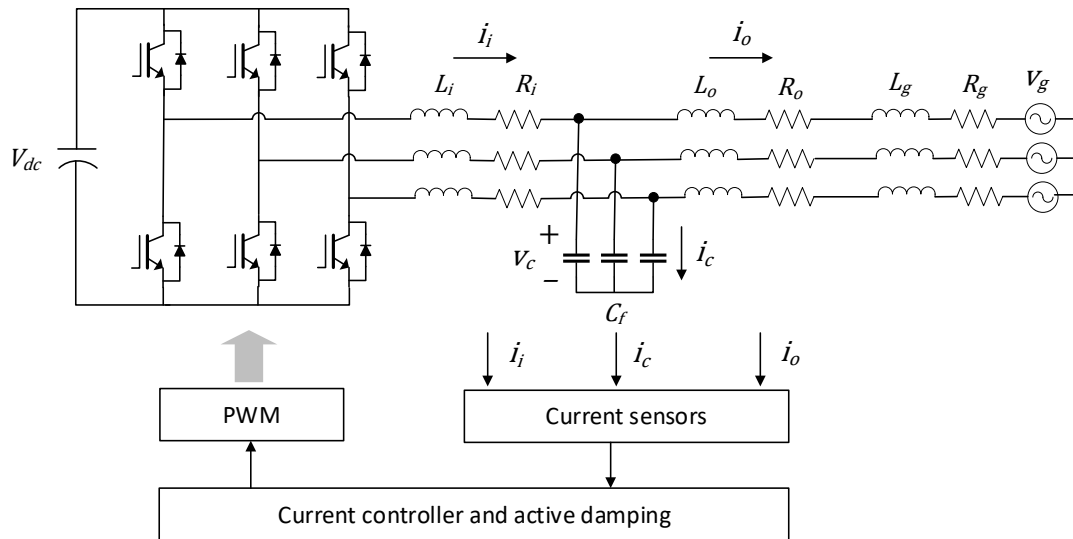


Figure 5.1 Grid-connected voltage source inverter with an LCL filter and an active damping current controller.

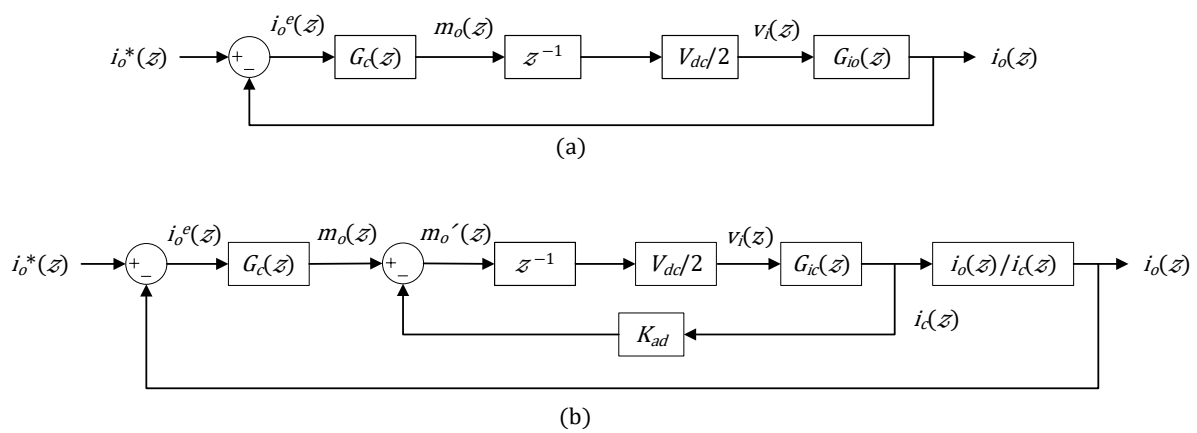


Figure 5.2 Single-phase equivalent current controller architectures. (a) A single-loop feedback current controller. (b) Dual-loop controller with capacitor-current active damping.

through an LCL filter output filter is shown in Figure 5.1. The primary control goal for the system is to regulate the grid current i_o to control the injected power into the grid. Typically, it is claimed that a single-loop feedback control is not adequate for this role because LCL-filter resonance causes controller instability [84]. Figure 5.2(a) shows a single-loop feedback controller which is modeled in the z -domain to account for digital sampling. It is shown in Figure 5.2(b) that a typical dual-loop control system that describes the resonance stability issue by including the active damping feedback of the capacitor current $i_c(z)$ via a damping gain K_{ad} [8]. For both of these controllers, $i_o^*(z)$ is the commanded grid current, $i_o(z)$ is the measured grid current, $G_c(z)$ is the controller transfer function, and the inverter is modeled as a linear $V_{dc}/2$ gain, with a sample delay z^{-1} to take into account the computation delay [8]. For analysis of the control systems of Figure 5.2 the discrete time-transfer functions for the LCL filter of $G_{io}(z)$, $G_{ic}(z)$, and $i_o(z)/i_c(z)$ are required. The first two of these transfer functions are well described in the literature [3], [84] in the s -domain as

$$G_{io}(s) = \frac{i_o(s)}{v_i(s)} = \frac{1}{sL_1} \frac{\gamma_{LC}^2}{(s + \omega_{res}^2)}, \quad (5.1)$$

$$G_{ic}(s) = \frac{i_c(s)}{v_i(s)} = \frac{1}{sL_1} \frac{s^2}{(s + \omega_{res}^2)}, \quad (5.2)$$

where $\omega_{res} = \sqrt{(L_i + L_o^g)/(L_i L_o C_f)}$ and $\gamma_{LC} = \sqrt{(1/(L_o^g C_f))}$. The filter grid-side inductance L_o and the inductance of the grid impedance L_g are lumped to be L_o^g .

Note that the winding resistance and core loss of the inductors have been neglected in Equations (5.1) and (5.2) to represent a worst undamped case [8]. The third transfer function relating i_o to i_c can be obtained by taking the ratio of Equations (5.1) and (5.2), i.e.,

$$\frac{i_o(s)}{i_c(s)} = \frac{G_{io}(s)}{G_{ic}(s)} = \frac{\gamma_{LC}^2}{s^2}. \quad (5.3)$$

Applying the zero-order-hold (ZOH) transform to (5.1) and (5.2) with a sampling period of $T_s = 1/f_s$ yields z -domain LCL filter transfer functions for i_o and i_c :

$$G_{io}(z) = \frac{i_o(z)}{v_i(z)} = \frac{T_s}{(L_i + L_o^g)(z - 1)} - \frac{\sin(\omega_{res}T_s)}{\omega_{res}(L_i + L_o^g)} \times \frac{z - 1}{z^2 - 2z \cos(\omega_{res}T_s) + 1}, \quad (5.4)$$

$$G_{ic}(z) = \frac{i_c(z)}{v_i(z)} = \frac{\sin(\omega_{res}T_s)}{\omega_{res}L_i} \times \frac{z - 1}{z^2 - 2z \cos(\omega_{res}T_s) + 1}. \quad (5.5)$$

To discretize Equation (5.3), it should be recognized that the grid current in Figure 5.2(b) results from the cascaded connection of $G_{ic}(z)$ and $i_o(z)/i_c(z)$. Since the grid and capacitor currents are practically sampled at the same time instant, the delay attributed to this process is taken into account by the ZOH transformation. Hence, $i_o(s)/i_c(s)$ is discretized using an impulse-invariant transformation [8], so that no additional delay is introduced to the system model, yielding

$$\frac{i_o(z)}{i_c(z)} = \frac{\gamma_{LC}^2 T_s^2 z}{(z - 1)^2}. \quad (5.6)$$

It is common to use a proportional plus resonance (PR) controller, which is equivalent to synchronous dq frame proportional plus integral [4], to eliminate steady-state tracking errors at the fundamental frequency ω_o . The transfer function of the PR controller with the proportional gain K_p and resonant time constant T_r yields

$$G_c(s) = K_p \left(1 + \frac{1}{T_r} \frac{s}{(s^2 + \omega_o^2)} \right). \quad (5.7)$$

The suitable discretization strategy for this controller is the Tustin transform with prewarping [8], which gives an equivalent discrete time controller transfer function of

$$G_c(z) = K_p \left(1 + \frac{1}{T_r} \frac{\sin(\omega_o T_s)}{2\omega_o} \frac{z^2 - 1}{(z^2 - 2z\cos(\omega_o T_s) + 1)} \right). \quad (5.8)$$

These transfer functions can now be combined to yield open-loop forward-path expressions for the controllers of Figure 5.2 so that control system analysis techniques, such as frequency response and root locus, can be utilized. For the single-loop controller shown in Figure 5.2(a), the forward-path transfer function is readily obtained as

$$\frac{i_o(z)}{i_o^e(z)} = z^{-1} V_{dc}/2G_c(z)G_{io}(z), \quad (5.9)$$

where $i_2^e(z) = i_2^*(z) - i_2(z)$ is the regulated current error. For the active damping controller shown in Figure 5.2(b), first the analysis is carried out by closing the inner capacitor-current-feedback active damping loop, i.e.,

$$\frac{i_c(z)}{m_o(z)} = \frac{V_{dc}/2G_{ic}(z)}{z + K_{ad}V_{dc}/2G_{ic}(z)}. \quad (5.10)$$

The forward-path transfer function of the overall system shown in Figure 5.2(b) is obtained by combining this result with transfer functions (5.6) and (5.8), yielding

$$\frac{i_o(z)}{i_o^e(z)} = G_c(z) \times \frac{i_c(z)}{m_o(z)} \times \frac{i_o(z)}{i_c(z)} = G_c(z) \times \frac{V_{dc}/2G_{ic}(z)[i_o(z)/i_c(z)]}{z + K_{ad}V_{dc}/2G_{ic}(z)}. \quad (5.11)$$

5.2 Identification of the Active Damping Regions

The critical frequency below which active damping is required can be obtained by calculating the point at which the phase of the forward-path reaches -180° , i.e.,

$$\angle \frac{i_o}{i_o^e}(z = e^{j\omega T_s}) = \angle e^{-j\omega T_s} V_{dc}/2G_c(e^{j\omega T_s})G_{io}(e^{j\omega T_s}) = -\pi. \quad (5.12)$$

The controller resonance frequency is over a decade below the crossover frequency and, hence, has little effect on this frequency. The LCL resonance makes no phase contribution until the resonance frequency is actually reached and thus $\angle G_{io}(e^{j\omega T_s})$ reduces to $\angle(\frac{1}{e^{j\omega T_s}} - 1)$.

Applying these into Equation (5.12) gives,

$$\angle \frac{i_o}{i_o^e}(z = e^{j\omega T_s}) = -\omega T_s - \frac{\pi}{2} - \frac{\omega T_s}{2} = -\pi \Rightarrow \omega_{crit} = \frac{\pi}{3T_s}. \quad (5.13)$$

5.3 Controller and Gain Determination

When an LCL resonance frequency is above the critical frequency ω_{crit} , obtained from Equation (5.13), active damping is not needed because sufficient resonant pole damping is ensured by single-loop control. Therefore, the PR controller defined by Equation (5.7) can be used as a grid current controller without further damping. Gain limitation for this region of stable operation is the position where the low-frequency poles are within the unit circle. Note that the poles are not produced from the resonant effect of an LCL filter but from series inductance and delays. This can be thought as a simple L filter system. Hence, in case an LCL resonance frequency is above the critical frequency, controller gains can be computed based on a standard L filter, where L is the sum of inverter-side and grid-side inductances [4]. With the fact that the magnitude and phase contribution of an LCL filter resonance is insignificant at the crossover frequency, the system response is dominated by the series inductance. Hence the only low-frequency component of the system model Equation (5.4) is required, and the single loop forward-path transfer function reduces to

$$\frac{i_o(z)}{i_o^e(z)} = z^{-1} V_{dc} / 2K_P \frac{T_s}{(z-1)(L_i + L_o^g)}. \quad (5.14)$$

The relation of the crossover frequency and phase margin is found as

$$\begin{aligned}
\angle \frac{i_o}{i_e}(z = e^{j\omega_c T_s}) &= \angle \frac{\frac{V_{dc}}{2K_p T_s}}{(L_i + L_o^g)} \frac{1}{e^{j\omega_c T_s}(e^{j\omega_c T_s} - 1)} \\
&= -\frac{\pi}{2} - \frac{\omega_c T_s}{2} - \omega_c T_s \\
&= -\frac{\pi}{2} - \frac{3}{2}\omega_c T_s.
\end{aligned} \tag{5.15}$$

Hence,

$$\phi_m = \pi + \angle \frac{i_o}{i_e}(z = e^{j\omega_c T_s}) = \frac{\pi}{2} - \frac{3}{2}\omega_c T_s \tag{5.16}$$

$$\Rightarrow \omega_c = \frac{\frac{\pi}{2} - \phi_m}{\frac{3T_s}{2}}. \tag{5.17}$$

The proportional gain is then set to have unity gain at the desired crossover frequency using Equation (5.18).

$$K_p = \left| \frac{(L_i + L_o^g)(e^{j\omega_c T_s} - 1)}{V_{dc}/2T_s} \right|. \tag{5.18}$$

With the approximation of $|e^{j\omega_c T_s} - 1| \approx \omega_c T_s$, this gives

$$K_p \approx \frac{2\omega_c(L_i + L_o^g)}{V_{dc}}. \tag{5.19}$$

The resonant time constant T_r can be obtained from the fact that its phase contribution is small at the crossover frequency [4].

$$T_r = \frac{10}{\omega_c}. \tag{5.20}$$

5.4 Capacitor Current Damping Gain Determination

A bounded range for damping gain K_{ad} can be determined by using the critical resonance frequency, $\omega_{crit} = \pi/(3T_s)$, at which root loci stay on the unit circle, giving a maximum value for the gain K_{ad} . A minimum gain of K_{ad} can be found using Routh's stability criterion [8]. The maximum value of gain K_{ad} can be obtained from the denominator of the closed-loop transfer function (5.11) by setting its magnitude is equal to unity. Substituting $G_{ic}(z)$ from Equation (5.5) and $i_o(z)/i_c(z)$ from Equation (5.6) gives

$$\left| \frac{V_{dc}/2\sin(\omega_{res}T_s)}{V_{dc}/2T_s} \times \frac{K_{ad}(z_0 - 1)^2 + K_p\gamma_{LC}^2 T z_0}{z_0(z_0 - 1)(z_0^2 - 2z_0 \cos(\omega_{res}T_s) + 1)} \right| = 1, \quad (5.21)$$

where z_0 is a specific pole location on the root locus at which the magnitude becomes one as the damping gain increases. $z_0 = 0.5 + j\sqrt{3}/2$ is selected from $z = e^{j\omega_c T_s}$ with $\omega_{crit} = \pi/3T_s$ and substitution into (19) with some mathematical manipulation gives K_{ad_max} :

$$K_{ad_max} = \frac{\omega_{res}L_i}{V_{dc}/2\sin(\omega_{res}T_s)} |1 - 2\cos(\omega_{res}T_s)| + K_p\gamma_{LC}^2 T_s^2. \quad (5.22)$$

K_{ad_min} can be found using the limiting ratio of proportional gain K_p to damping gain K_{ad} from the Routh's stability criterion in [8], which is given as

$$\frac{K_p}{K_{ad}} \leq \frac{L_i + L_o^g}{L_i}, \quad (5.23)$$

$$\Rightarrow K_{ad_min} = \frac{K_p L_i}{L_i + L_o^g}. \quad (5.24)$$

Within these limits for the damping gain, a root locus pole placement strategy can be used to determine the value of K_{ad} which achieves the most damping.

5.5 Design of Current Controller and Active Damping Gain

In three-phase VSI systems, synchronous frame PI (SRFPI) controllers to regulate the grid currents are commonly used in the synchronous rotating frame where the three-phase ac currents are transformed into dc components. Since the overall control system operates on dc quantities, the steady-state error that is typically associated with application of a PI controller to ac quantities is eliminated in using a SRFPI controller in the synchronous dq reference frame. Control systems design in the synchronous dq reference frame has a particular advantage of independent control of real and reactive current components, which in turn allows direct real and reactive power flow control. The transfer function of a SRFPI controller in the synchronous dq reference frame is expressed as

$$[G_c^{dq}(s)] = \begin{bmatrix} K_p + \frac{K_i}{s} & 0 \\ 0 & K_p + \frac{K_i}{s} \end{bmatrix}. \quad (5.25)$$

The equivalent stationary abc frame representation of the SRFPI controller is developed by means of the transformation techniques described in chapter 2 as [102]:

$$[G_c^{abc}(s)] = \frac{2}{3} \begin{bmatrix} K_p + \frac{K_i s}{s^2 + \omega_o^2} & -\frac{K_p}{2} + \frac{-1/2K_i s - \sqrt{3}/2K_i \omega_o}{s^2 + \omega_o^2} & \\ -\frac{K_p}{2} + \frac{-1/2K_i s + \sqrt{3}/2K_i \omega_o}{s^2 + \omega_o^2} & K_p + \frac{K_i s}{s^2 + \omega_o^2} & \\ -\frac{K_p}{2} + \frac{-1/2K_i s - \sqrt{3}/2K_i \omega_o}{s^2 + \omega_o^2} & -\frac{K_p}{2} + \frac{-1/2K_i s + \sqrt{3}/2K_i \omega_o}{s^2 + \omega_o^2} & \\ -\frac{K_p}{2} + \frac{-1/2K_i s + \sqrt{3}/2K_i \omega_o}{s^2 + \omega_o^2} & & \\ -\frac{K_p}{2} + \frac{-1/2K_i s - \sqrt{3}/2K_i \omega_o}{s^2 + \omega_o^2} & & \\ K_p + \frac{K_i s}{s^2 + \omega_o^2} & & \end{bmatrix} \quad (5.26)$$

The main concern with Equation (5.26) is the off-diagonal terms representing cross coupling between phases, which make it hard to attain a single-phase representation.

In contrast, the transfer function matrix of a PR controller in the stationary reference frame which can be adopted in place of a PI controller in the synchronous reference frame is independent between phases. The PR controller transfer function which can be directly applied to ac signals is obtained by transforming a desired dc controller into an equivalent ac controller. The equivalent ac controller has the same frequency response characteristics in the frequency range of concern. The transformation relating a dc controller to an equivalent ac controller is given by [103]

$$G_{AC}(s) = \frac{H_{DC}(s + j\omega_o) + H_{DC}(s - j\omega_o)}{2}. \quad (5.27)$$

In some cases, implementation of the transfer function described in Equation (5.27) is difficult. Therefore, an alternative to the transformation is to make use of the low-pass to band-pass technique developed in network synthesis [103]

$$G_{AC}(s) = G_{DC}\left(\frac{s^2 + \omega_o^2}{2s}\right). \quad (5.28)$$

The good aspect of this approach is that a transformed controller has more tolerance. In addition, the application of this transformation scheme to a single phase system is straightforward [103].

A conventional PI controller transfer function can be transformed into an equivalent ac controller using the transformation of (5.27) as follows [103].

$$G_{DC}(s) = K_p + \frac{K_i}{s} \quad (5.29)$$

$$G_{AC}(s) = K_p + \frac{2K_i s}{s^2 + \omega_o^2} \quad (5.30)$$

Based on the equivalent ac controller, the transfer function matrices of a PR controller in the abc and $\alpha\beta$ reference frames, respectively, which are corresponding to the SRFPI controller in Equation (5.25), are given by

$$[G_c^{abc}(s)] = \begin{bmatrix} K_p + \frac{2K_i s}{s^2 + \omega_o^2} & 0 & 0 \\ 0 & K_p + \frac{2K_i s}{s^2 + \omega_o^2} & 0 \\ 0 & 0 & K_p + \frac{2K_i s}{s^2 + \omega_o^2} \end{bmatrix}, \quad (5.31)$$

$$[G_c^{\alpha\beta}(s)] = \begin{bmatrix} K_p + \frac{2K_i s}{s^2 + \omega_o^2} & 0 \\ 0 & K_p + \frac{2K_i s}{s^2 + \omega_o^2} \end{bmatrix}. \quad (5.32)$$

The obtained transfer functions both have infinite gain at the fundamental frequency ω_o , hence leading to zero steady state error. Another significant aspect in the transfer functions is that there is no off-diagonal terms, indicating phase independence. This allows a three-phase system including a PR controller to be easily reduced to a single-phase equivalent. Consequently, stability analysis and transient performance of the system with the PR controller can be readily carried out using conventional analysis techniques. From the fact that the PR controller has similar performance characteristics to the corresponding SRFPI controller, stability and transient performance analysis for a three-phase system with a SRFPI controller can be well predicted by the single-phase equivalent system which includes the corresponding PR controller in the stationary reference frame.

According to the controller and gain determination methods, PR controllers in continuous and discrete time domains are designed for the grid-connected inverter with the LCL filter of the regenerative drive. The parameters values are given in Table 5.1.

Table 5.1. Grid-Connected Inverter of the Regenerative Drive and LCL Filter System Parameters

Description	Symbols	Values
Rated power	P	2 MVA
Grid frequency	f_g	60 Hz
PWM carrier frequency	f_{sw}	4 kHz
Sampling frequency	f_s	8 kHz
Phase grid voltage	v_g	277 V _{rms}
DC link voltage	V_{dc}	900 V
Inverter-side inductance	L_i	20 μ H
Grid-side inductance	L_o	6.1 μ H
Filter capacitance	C_f	1,440 μ F

The current controller proportional gain K_p has been selected such that the crossover frequency achieves a desired phase margin of $\phi_m = 45^\circ$ according to Equation (5.19), giving resultant values of $K_p = 0.00024 \text{ A}^{-1}$ and $\omega_c = 4189 \text{ rad/s}$. With a resonant time constant $T_r = 0.00238 \text{ s/rad}$, the PR controller in continuous time defined by Equation (5.7) is obtained.

$$G_c^{abc}(s) = \frac{0.00024s^2 + 0.1005s + 34.11}{s^2 + 142129}. \quad (5.33)$$

According to Equation (5.8), applying the Tustin transform with prewarping [8] and a sampling period of $125\mu\text{s}$ gives the equivalent controller transfer function in discrete time, i.e.,

$$G_c^{abc}(z) = \frac{0.0002463z^2 - 0.0004795z + 0.0002337}{z^2 - 1.998z + 1}. \quad (5.34)$$

For application in the synchronous reference frame, using the obtained $K_p = 0.00024 \text{ A}^{-1}$ and $K_i = 0.05042 \text{ rad s}^{-1} \text{ A}^{-1}$, the corresponding SRFPI controller in continuous time is given.

$$G_c^{dq}(s) = 0.00024 + \frac{0.05042}{s} = \frac{0.00024s + 0.05042}{s}. \quad (5.35)$$

With a sampling period of $125 \mu\text{s}$, the SRFPI controller in discrete time is obtained by means of zero-order hold (ZOH) as

$$G_c^{dq}(z) = \frac{0.00024z - 0.000234}{z - 1}. \quad (5.36)$$

For a dc system, a conventional PI transfer function leads to zero steady-state error. Hence, an equivalent ac loss-less resonant compensator can be adopted for an ac grid-connected inverter system. However, the realization of an ideal dc integrator or its corresponding ac equivalent resonant compensator is unfeasible due to component tolerances in analog systems and finite precision in digital systems. Therefore a low-pass transfer function can be applied in place of the ideal integrator as

$$G_{\text{DC}}(s) = K_p + \frac{K_i \omega_i}{s + \omega_i}. \quad (5.37)$$

This transforms using Equation (5.28) into its equivalent ac proportional resonant (PR) current controller as

$$G_c^{abc}(s) = K_p + \frac{2K_i\omega_i s}{s^2 + 2\omega_i s + \omega_o^2}, \quad (5.38)$$

where ω_i is the lower breakpoint frequency of the dc transfer function and ω_o is the fundamental angular frequency. With ω_i equal to $\pi/8$, the current controller transfer function in the stationary reference frame is obtained as

$$G_c^{abc}(s) = \frac{0.00024s^2 + 0.039788s + 34.11}{s^2 + 0.785398s + 142129}. \quad (5.39)$$

The discretization strategy of zero-order hold (ZOH) with a sampling period of 125 μ s is applied to the transfer function, yielding

$$G_c^{abc}(z) = \frac{0.00024z^2 - 0.0004745z + 0.000235}{z^2 - 1.998z + 1}. \quad (5.40)$$

The corresponding continuous time SRFPI transfer function in Equation (5.37) based on the low-pass filter approximation is given using $\omega_i = \pi/8$ and the previously obtained $K_p = 0.00024 \text{ A}^{-1}$ and $K_i = 0.05042 \text{ rad s}^{-1} \text{ A}^{-1}$ as

$$G_c^{dq}(s) = 0.00024 + \frac{0.019799}{s + 0.392699} = \frac{0.00024s + 0.019893}{s + 0.392699}. \quad (5.41)$$

The transfer function in discrete time using the discretization strategy of zero-order hold (ZOH) with a sampling period of 125 μ s is given by

$$G_c^{dq}(z) = \frac{0.00024z - 0.000237}{z - 1}. \quad (5.42)$$

Although the obtained continuous time transfer functions based on an ideal integrator or low-pass filter appear to be somewhat different, their discrete time transfer functions are almost

identical. The discretization results validate the two derived controllers are close enough to be interchangeable.

Nyquist plots are commonly used in the frequency-response representation of linear time-invariant control systems. Nyquist plots are polar plots, whereas Bode diagrams are rectangular plots. Nyquist stability criterion assesses the stability of a closed-loop system from its open-loop frequency response and open-loop poles. The criterion, derived by H. Nyquist, is useful in control engineering since the absolute stability of a closed-loop system can be evaluated graphically from open-loop frequency response curves. Also, there is no need for determining the closed-loop poles. Both analytically obtained open-loop frequency-response curves and experimentally obtained ones can be used for the stability analysis. It can be also used in evaluating the stability of grid-connected inverters. The Nyquist stability criterion equation denotes $Z = P - 2(N_{(+)} - N_{(-)})$, where P and Z denote the numbers of open-loop and closed-loop right-half-plane (RHP) poles, respectively, and $N_{(+)}$ and $N_{(-)}$ denote the numbers of positive and negative -180° crossings, respectively. The sufficient and necessary stability condition requires $Z = 0$.

For the single-loop controller, implying that the active damping is not incorporated, the forward-path transfer function defined by Equation (5.9) does not contain open-loop RHP pole, i.e., $P = 0$. According to the Nyquist stability criterion, in order to ensure stability of the system this requirement, $N_{(+)} - N_{(-)} = 0$, should be satisfied. Which means the number of positive -180° crossings should be equal to the number of negative -180° crossings. The Bode diagram of the forward-path transfer function with the gain K_{ad} set to zero, indicating no capacitor-current-feedback active damping, under variations in grid-side inductance is shown in Figure 5.3.

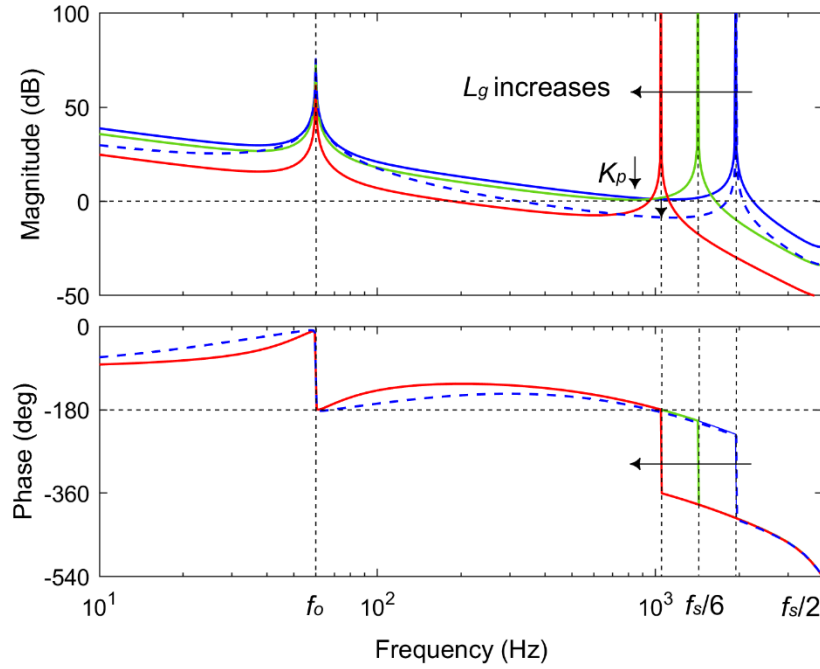


Figure 5.3. Bode diagram of the loop gain of single-loop grid-current control with variations in grid inductance.

As seen, the phase-frequency curves for different grid inductances monotonously fall, thus there is no positive -180° crossing, $N_{(+)} = 0$. In theory, when $f_r < f_s/6$, the negative crossing occurs at f_r , whereas when $f_s/6 < f_r < f_s/2$, the phase-frequency curve crosses -180° at $f_s/6$ due to the phase lag resulting from the time delays. It is not considered as a negative crossing in terms of the Nyquist stability criterion as long as the gain at the frequency is below 0 dB. This can be attained by adjusting the proportional gain K_P . However, as seen in Figure 5.3, -180° crossings are located below $f_s/6$ to some extent. It is thought that this is due to adoption of the first-order padé approximation for the time delays. According to the above analysis, when the resonance frequency of an LCL filter, f_r , is above the critical frequency, the system stability can be ensured by reducing the proportional gain, which corresponds to the blue dashed line in Figure 5.3. It has

no negative -180° crossing because the gain margin is positive at the critical frequency and no additional -180° crossing occurs at its resonance frequency.

As the grid inductance increases, the resonance frequency of the LCL filter shifts to left as shown in Figure 5.3. When the resonance frequency is located below the critical frequency, a -180° crossing occurs at the resonance frequency, f_r . In this case, there is no way of avoiding the negative -180° crossing by adjustments of the gain K_p . In addition, a positive -180° crossing which can cancel out the effect of the negative -180° crossing is not attainable since there is no potential positive -180° crossing. Therefore, active damping should be employed to remove the negative -180° crossing to ensure stability of the system.

Closed-loop pole movement of the single-loop and the dual loop, i.e. with active damping applied, is shown in Figure 5.4. The root loci of the single- and dual-loop systems can be properly determined by plotting the poles of their closed-loop transfer functions. The relevant expressions can be developed by setting the denominators of the closed-loop transfer functions to zero. Note that, for this root locus analysis, the PR controller function $G_c(z)$ is reduced to K_p since the resonance gain has negligible effect above the fundamental frequency, ω_o . The relevant expression for the single-loop controller developed from Equation (5.9) is given as

$$z + V_{dc}/2K_p G_{i_o}(z) = 0. \quad (5.43)$$

The expression for the dual-loop controller from Equation (5.11) is derived as

$$z + K_{ad}V_{dc}/2G_{i_c}(z) + K_p V_{dc}/2G_{i_c}(z)[i_o(z)/i_c(z)] = 0. \quad (5.44)$$

There are three cases in which the locations of the resonance frequencies are different with respect to the critical frequency. When $f_s/6 < f_r < f_s/2$, for the single-loop grid current feedback system, the poles initially track well inside the unit circle. Hence, the system remains

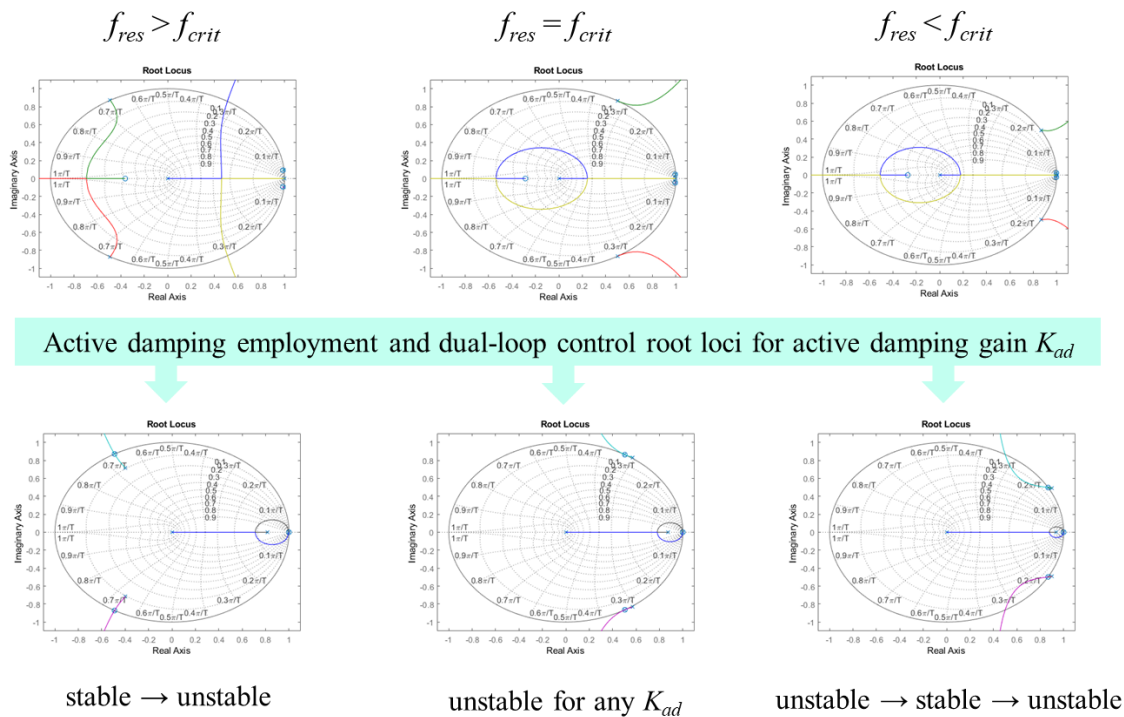


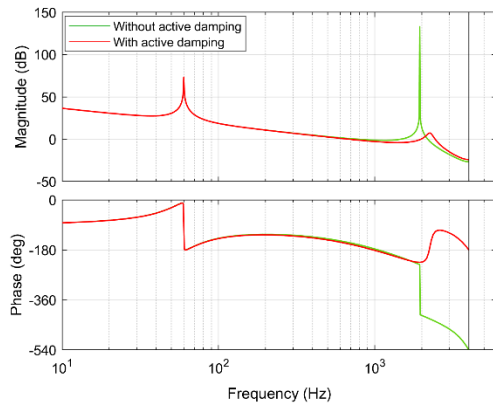
Figure 5.4. Stability analysis with root loci of variations in active damping gain K_{ad} for different cases in terms of resonance frequency (f_{res}) relative to the critical frequency (f_{crit}).

stable until excessive proportional gain K_p is applied. The poles move out of the unit circle as the gain K_p increases beyond the critical value which locates the poles on the boundary of the unit circle. In contrast, when the resonance frequency is at or below the critical frequency, the resonant pole pairs always track away from the unit circle as shown in Figure 5.4. Hence, the system must be unstable irrespective of the proportional gain without active damping

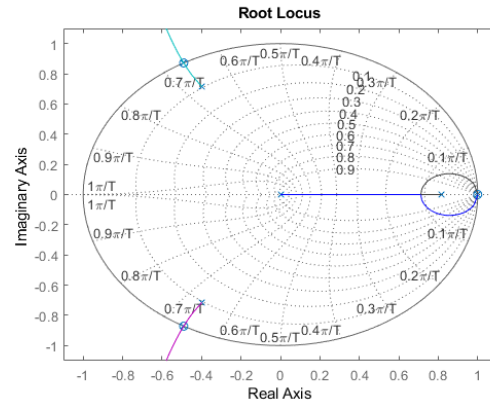
The root loci at the bottom of Figure 5.4 show the effect of capacitor-current-feedback active damping with the dual-loop controller for a fixed given value of K_p . When the LCL filter-induced resonance frequency is below the critical frequency, increasing the damping gain K_{ad} forces the poles which are initially outside the unit circle due to the outer loop gain to track back inside the unit circle, and the system becomes stable. However, too much damping gain can drive

the poles to track back outside the unit circle, and the system lose the stability. In addition, when the resonance frequency is equal to the critical frequency, the resonant poles only touch the unit circle but never enter inside the unit circle, and hence the system never becomes stable regardless of the damping gain K_{ad} .

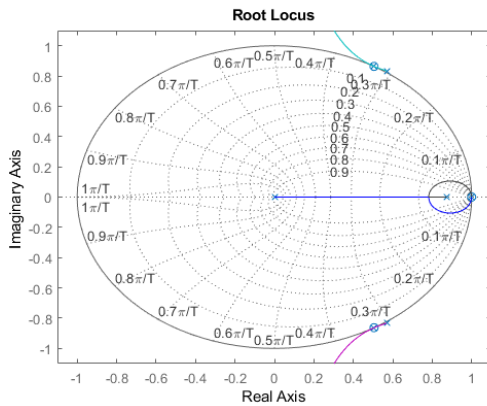
The Bode plot of Figure 5.5(a) shows the frequency responses of the single- and dual-loop current controllers when the resonance frequency is lower than half the sampling frequency. Without active damping (i.e., single loop), the high-frequency LCL filter resonance at 1,940 Hz causes a sharp phase transition through -180° with a very high resonance frequency magnitude. This is an unconditionally unstable situation for any available controller gains. Therefore, the resonance frequency magnitude should be damped such that the magnitude remains below 0 dB for ensuring stability of the system. Incorporating active damping using the dual-loop controller attenuates the resonant peak magnitude below zero magnitude, so that the system can be stabilized with the selected controller gain. There exists a critical LCL filter resonance frequency above which a single-loop controller could achieve a stable response, but below which active damping is required to ensure stability. The critical frequency is obtained using Equation (5.13), which is $f_{crit} = 1,333$ Hz. If an LCL filter resonance frequency is above its critical frequency, a single loop is sufficient for the system to become stable. In the case, the LCL filter resonance frequency is definitely higher than the critical frequency. However, stability does not depend solely on the resonance frequency of the LCL filter because the region of operation tends to shift based on grid conditions. In particular, a weak grid has a significant effect on the resonance frequency with high impedance. A grid inductance of $14 \mu\text{H}$ is assumed and added to the LCL filter system, which lowers the resonance frequency from 1,940 Hz to 1,327 Hz.



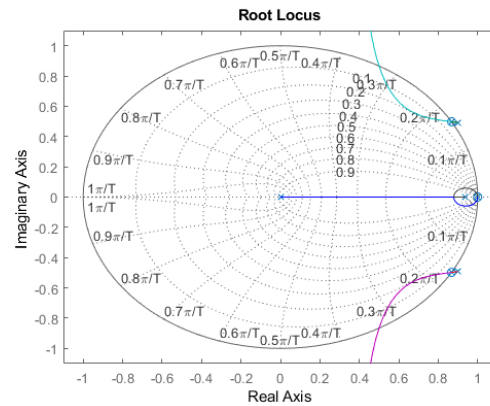
(a)



(b)



(c)



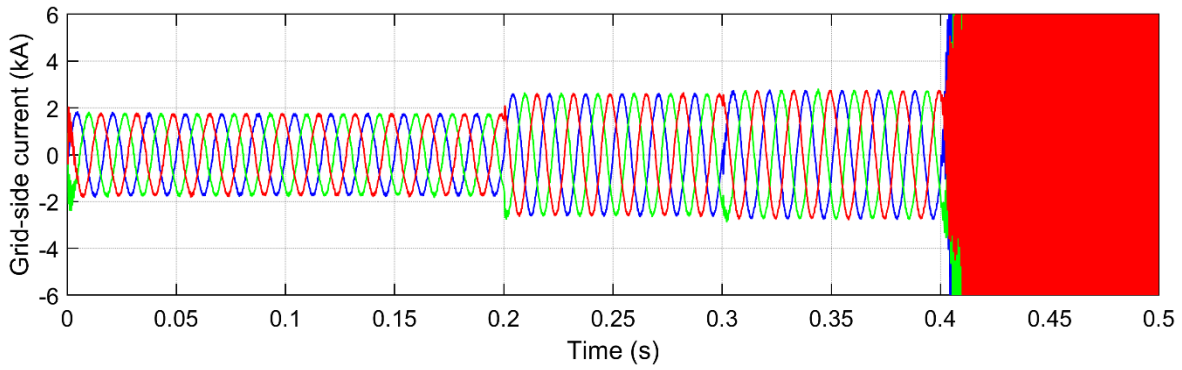
(d)

Figure 5.5 (a) Bode diagrams of the forward-path transfer functions of the single- and dual-loop current controllers. Root loci of the dual-loop current controller with respect to active damping gain K_{ad} : (b) resonance frequency is higher than the critical resonance frequency, (c) resonance frequency is at the critical frequency, (d) resonance frequency is lower than the critical frequency.

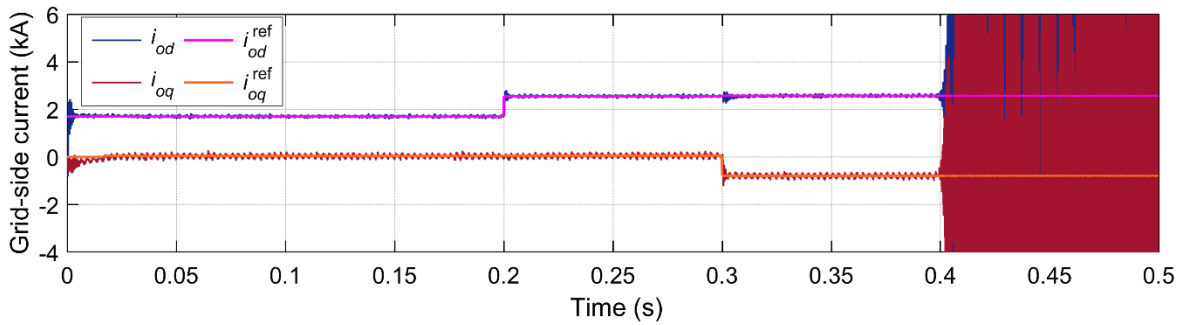
The root loci of the dual-loop systems employing active damping for damping gain K_{ad} are shown in Figure 5.4(b), (c), and (d), with sampling frequencies 4 kHz, 8 kHz, and 16 kHz for (b), (c), and (d) respectively. With the grid inductance accounted for, the system has a resonance frequency of 1,327 Hz. The critical frequencies are 667 Hz, 1,333 Hz, and 2,667 Hz for sampling frequencies of 4 kHz, 8 kHz, and 16 kHz, respectively. When the resonance frequency, 1,327 Hz, is higher than the critical frequency, 667 Hz, in Figure 5.5(b), the roots initially move from the

inside of the unit circle towards the outside as the gain K_{ad} increases. In contrast, when the filter system resonance frequency is at the critical resonance, in this case $f_{crit} = 1,333$ Hz, the resonant pole pairs always move away from the unit circle as shown in Figure 5.5(c). Hence, the system is always unstable irrespective of the controller gain. In case of the LCL resonance frequency being lower than the critical frequency, $f_{crit} = 2,667$ Hz with a sampling frequency of 16 kHz, the resonant poles move inward to have a damping contribution. They move outside the unit circle as the damping gain K_{ad} is increased further shown in Figure 5.5(d). Apparently, there is a maximum damping gain, beyond which the system loses its stability. For the system with a sampling frequency of 16 kHz, a bounded range for the damping gain K_{ad} is determined from Equations (5.22) and (5.24), which gives $K_{ad_min} \leq K_{ad} \leq K_{ad_max}$ with $K_{ad_min} = 0.000186$ A⁻¹ and $K_{ad_max} = 0.000324$ A⁻¹. This means that the limited range of the damping gain K_{ad} allows for effective stability. The best available value for the damping gain is selected to place the two resonance poles as far from the unit circle as possible to achieve the maximum damping. The position of these poles is determined by the solution of the denominator of the characteristic equation (5.31).

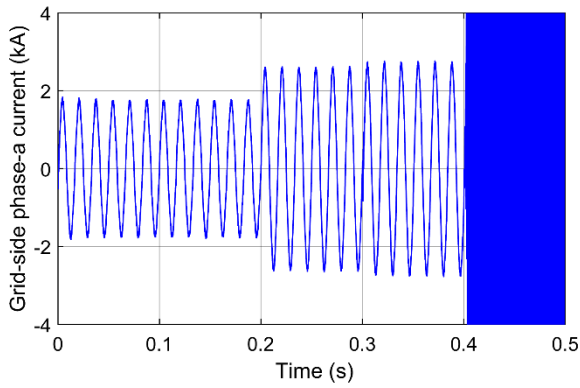
Simulation studies for the grid-tied LCL-filtered VSI system with active damping being applied are carried out using Matlab/Simulink. Voltage and current waveforms injected to a stiff grid of which impedance is negligible are shown in Figure 5.6. Initially an active power of 1 MW is supplied to the grid and subsequently is raised to 1.5 MW at 0.2 s and then 0.5 MVAR reactive power is supplied to the grid from 0.3 s. After the active damping is disabled at 0.4 s, the grid injected currents start to oscillate considerably due to the resonance effect caused from the LCL filter although the system including the controller remains in the stable region in theory.



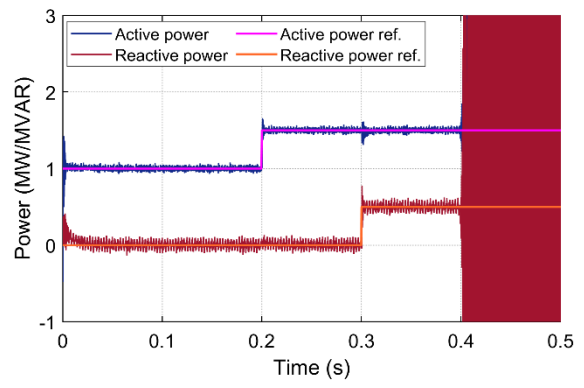
(a)



(b)

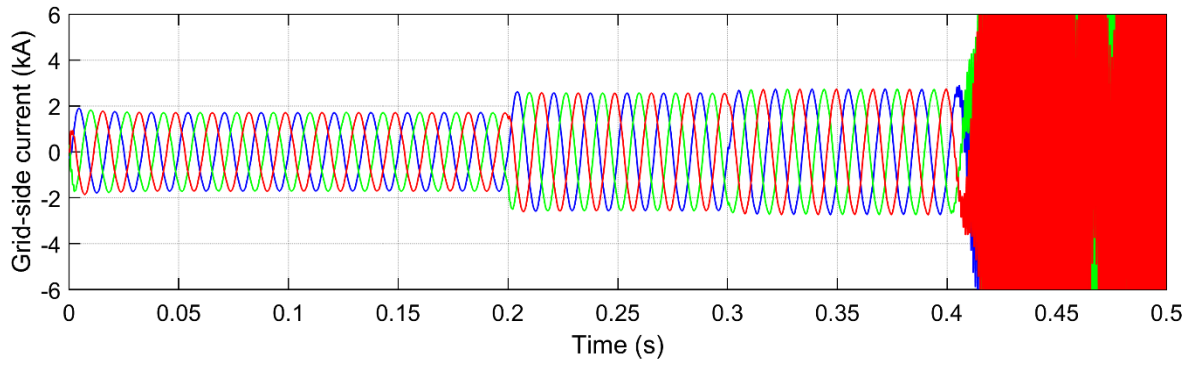


(c)

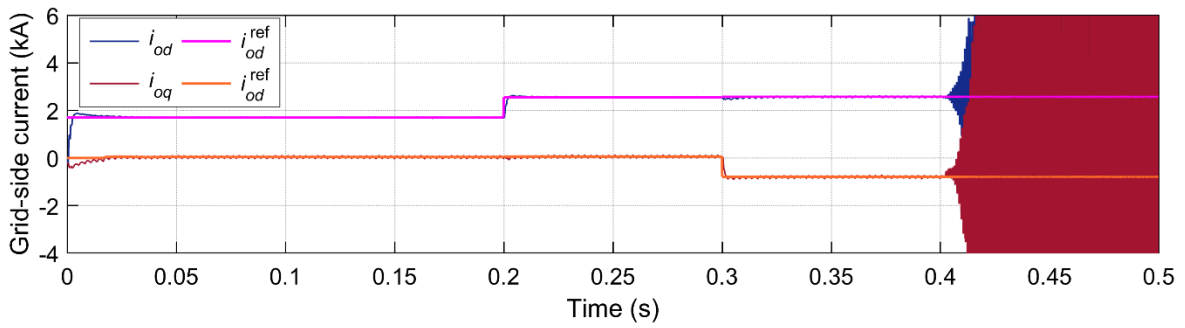


(d)

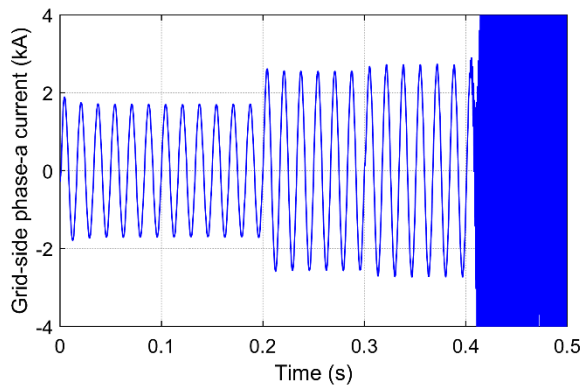
Figure 5.6 Active damping applied VSI with an LCL filter in a stiff grid with a step change in active power at 0.2 s and a step change in reactive power at 0.3 s and subsequent active damping off at 0.4 s. (a) Grid currents. (b) Grid voltages. (c) Grid phase-a current. (d) Injected active and reactive powers.



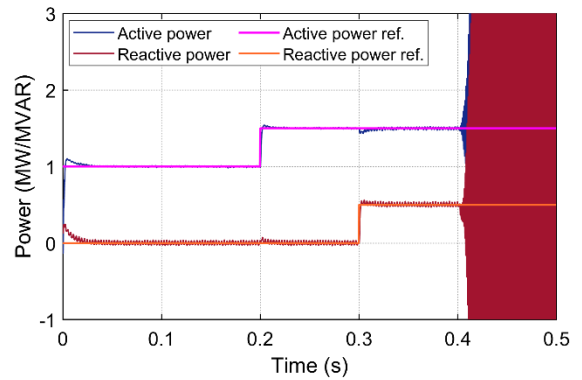
(a)



(b)



(c)



(d)

Figure 5.7. Active damping applied VSI with an LCL filter in a weak grid with a step change in active power at 0.2 s and a step change in reactive power at 0.3 s and subsequent active damping off at 0.4 s. (a) Grid currents. (b) Grid voltages. (c) Grid phase-a current. (d) Injected active and reactive powers.

For comparison, the same system is connected to a weak grid of which impedance consists of only an inductance of $60 \mu\text{H}$. As soon as the active damping feedback is disabled at 0.4 s, large resonant currents occur, which causes instability of the entire system as shown in Figure 5.7. For step changes in active and reactive power, the system has good dynamic responses with short settling times both in the stiff and the weak grids as a consequence of the controller gain being set as high as possible and the properly tuned capacitor-current-proportional-feedback active damping.

5.6 Stability Analysis of Capacitor-Current-Feedback Active Damping

Representation of the grid-connected inverter with the LCL filter in continuous time is shown in Figure 5.8, where $G_d(s)$ denotes the computation and PWM delays as

$$G_d(s) = e^{-(\lambda+0.5)sT_s}, \quad (5.45)$$

where T_s is the sampling period. In the digitally controlled system, there are computation and PWM delays. The computation delay is the time duration from a sampling instant to the corresponding PWM reference update instant. It comprises three types of time delays: an analog-to-digital conversion delay, a delay of computation of a duty ratio, and a duty-ratio update delay. The computation delay can be expressed in general form as λT_s ($0 < \lambda \leq 1$). It is one sampling period ($\lambda = 1$) in case of synchronous sampling with double-update PWM, where sampling takes place twice at the peak and the trough during one switching period. The sampling frequency is two times the switching frequency. When the sampling frequency is the same as the switching frequency, i.e., synchronous sampling with single-update PWM, a sampling period delay of $0.5T_s$ exists, i.e., $\lambda = 0.5$. The PWM delay is attributed to the ZOH effect which keeps the PWM

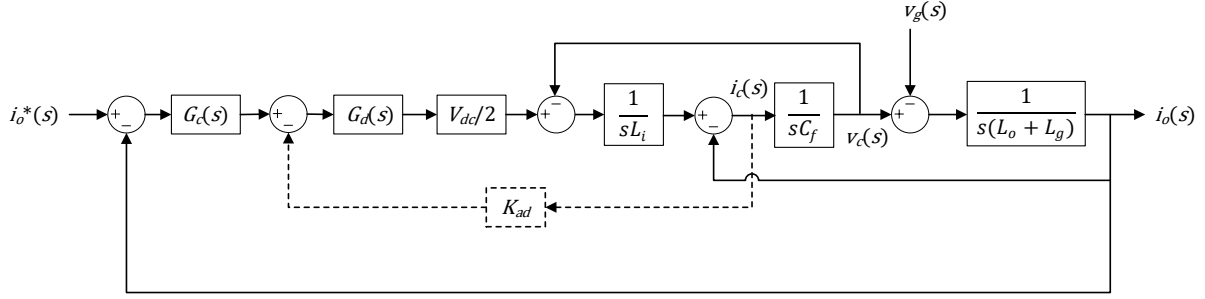


Figure 5.8. Control block diagram of the LCL filter-equipped grid-connected inverter with capacitor-current-proportional-feedback active damping.

reference constant until the next reference update, and it is definitely half the sampling period ($0.5T_s$).

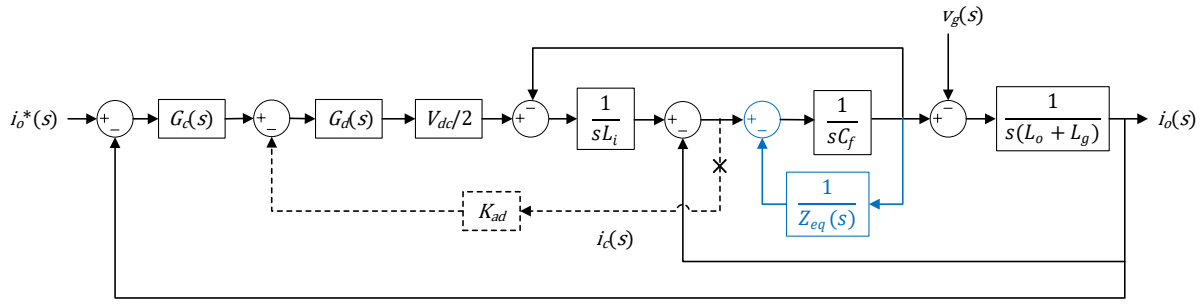
A proportional resonant (PR) current controller is suitable for the controller, $G_c(s)$, of the system and is expressed in Equation (5.38). The steady-state output phase and magnitude errors attained by the controller are approximately zero since the magnitude of the transfer function achieves a relatively high gain at the reference frequency.

Based on Figure 5.8, the loop gain $T(s)$ is derived as

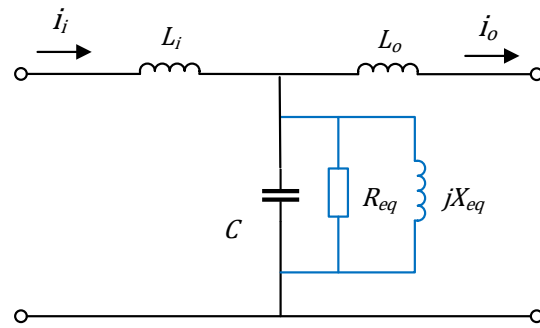
$$T(s) = \frac{G_c(s)}{sL_i(L_o + L_g)C_f} \cdot \frac{V_{dc}/2G_d(s)}{s^2 + \frac{K_{ad}V_{dc}/2G_d(s)}{L_i} + \omega_r^2}, \quad (5.46)$$

where ω_r is the LCL filter angular resonance frequency.

$$\omega_r = \sqrt{\frac{L_i + L_o + L_g}{L_i(L_o + L_g)C_f}}. \quad (5.47)$$



(a)



(b)

Figure 5.9. Representation of the LCL filter-equipped grid-connected inverter with equivalent virtual impedance of the capacitor-current-proportional-feedback active damping. (a) Block diagram. (b) Virtual impedance equivalent circuit.

As observed from Figure 5.8, the transfer function of the delays, $G_d(s)$, is in the forward path of the capacitor-current-feedback loop, which means that the delays definitely have an effect on the capacitor-current-feedback active damping. For a comprehensive investigation of the effect, an equivalent block diagram is attained in Figure 5.9(a) by replacing the capacitor current signal $i_c(s)$ with $v_c(s)$, and relocating its feedback node from the output of $G_c(s)$ to the input of $1/(sC_f)$. Equivalent transformation provides the equivalent virtual impedance Z_{eq} of the capacitor-current-feedback active damping connected in parallel with the filter capacitor as shown in 5.9(b). The virtual impedance Z_{eq} is expressed with the $G_d(s)$ in Equation (5.45) as

$$\begin{aligned}
Z_{eq}(s) &= \frac{L_i}{K_{ad}V_{dc}/2C_f G_d(s)} \\
&= \frac{L_i}{K_{ad}V_{dc}/2C_f} e^{(\lambda+0.5)sT_s}.
\end{aligned} \tag{5.48}$$

Substituting $s = j\omega$ into (5.48) gives

$$\begin{aligned}
Z_{eq}(j\omega) &= \frac{L_i}{K_{ad}V_{dc}/2C_f} \cos(\lambda + 0.5)\omega T_s + j \frac{L_i}{K_{ad}V_{dc}/2C_f} \sin(\lambda + 0.5)\omega T_s \\
&\triangleq R_{eq}(\omega) // jX_{eq}(\omega),
\end{aligned} \tag{5.49}$$

where

$$\begin{aligned}
R_{eq}(\omega) &= \frac{L_i}{K_{ad}V_{dc}/2C_f \cos(\lambda + 0.5)\omega T_s} \\
X_{eq}(\omega) &= \frac{L_i}{K_{ad}V_{dc}/2C_f \sin(\lambda + 0.5)\omega T_s}.
\end{aligned} \tag{5.50}$$

From the equations, Z_{eq} can be thought as parallel connection of a resistance R_{eq} and a reactance X_{eq} as shown in Figure 5.9(b). From the perspective of their effects on the LCL filter resonance peak, the resistance component R_{eq} dampens the LCL filter resonance peak, and the reactance component X_{eq} causes displacement of the peak. Both R_{eq} and X_{eq} contain the angular frequency ω , indicating a frequency-dependent characteristic. Due to the trigonometric functions in R_{eq} and X_{eq} , R_{eq} can be either positive or negative, while X_{eq} can be either inductive or capacitive depending on the signs of the trigonometric functions. According to Equation (5.50), the frequency characteristics of R_{eq} and X_{eq} with the capacitor-current-feedback gain K_{ad} being positive are obtained as seen in Figure 5.10. In case of synchronous sampling with double-update PWM of which λ is equal to 1, R_{eq} is positive in the frequency range of $0 < f < f_s/6$ and negative in the frequency range of $f_s/6 < f < f_s/2$. Thus, the frequency asymptote of R_{eq} at which it turns

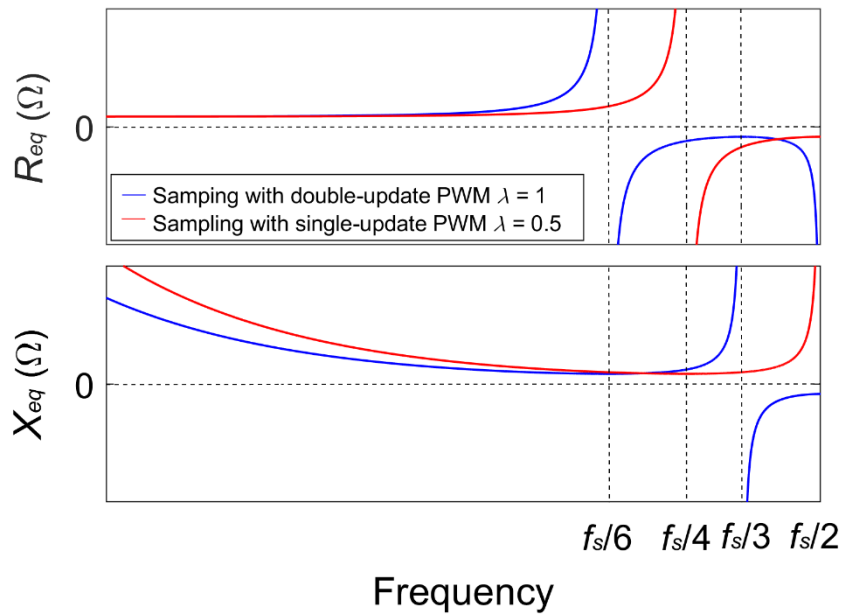
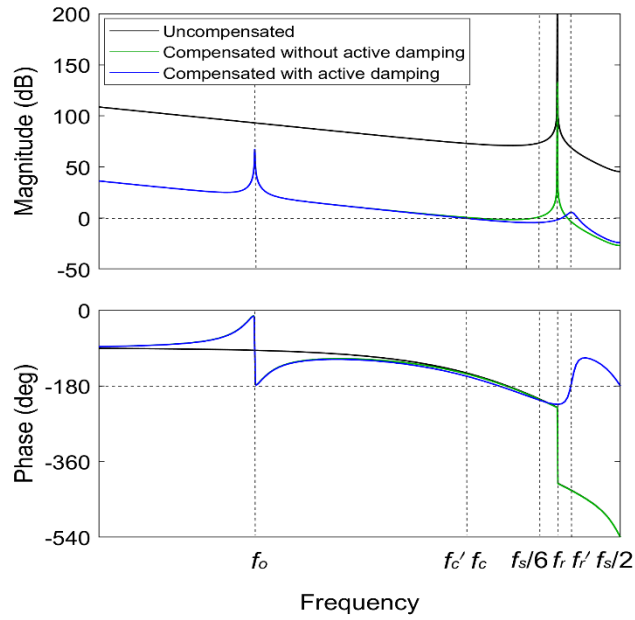


Figure 5.10. Magnitude curves of R_{eq} and X_{eq} as a function of frequency.

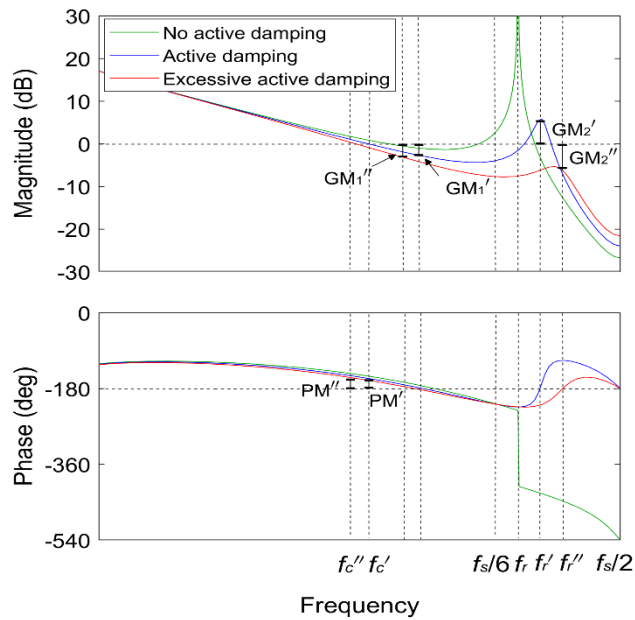
from positive to negative is at the critical frequency, $f_s/6$. The reactance, X_{eq} , is inductive in the frequency range of $0 < f < f_s/3$ and becomes capacitive in the frequency range of $f_s/3 < f < f_s/2$. Therefore, the frequency asymptote of X_{eq} where it turns to be capacitive from inductive is at $f_s/3$. When synchronous sampling with single-update PWM whose λ is equal to 0.5 is adopted, R_{eq} is positive in the frequency range of $0 < f < f_s/4$ and negative above $f_s/4$, whereas X_{eq} remains inductive in the full range. Thus, the frequency asymptote of R_{eq} where it turns from positive to negative is at $f_s/4$.

Note that when R_{eq} is negative, a pair of open-loop unstable poles is produced in RHP. This is verified by investigating the roots of the denominator of the system loop gain $T(s)$ derived by Equation (5.46) according to Routh's Method.

For the case of synchronous sampling with double-update PWM implying $\lambda = 1$, the Bode diagrams of the system loop gain $T(z)$, a discrete equivalent of the continuous system loop gain $T(s)$, converted using the zero-order-hold (ZOH) are shown in Figure 5.11. The proportional resonant current controller $G_c(s)$ in Equation (5.39) is employed for the $T(s)$. It is attained with a target of phase margin (PM) equal to 45° for the LCL filter given in Table 5.1 with zero grid inductance. The Bode diagrams of the same system with a grid inductance of $60 \mu\text{H}$, which shifts the LCL filter resonance frequency, are shown in Figure 5.12. As seen in Figure 5.11, with the controller, the compensated systems have a relatively high gain at the fundamental reference frequency, which is 60 Hz grid frequency. Therefore, the closed-loop transfer function of the system definitely approaches unity at the fundamental reference frequency, meaning that the grid-injected current tracks well the reference sinusoid without phase or magnitude error. In case without active damping, the LCL resonance frequency f_r is higher than the critical frequency $f_s/6$, and the phase-frequency curve crosses -180° below the critical frequency to some extent in the direction of phase falling. There are no more -180° crossings in the frequency range. Thus, as long as the gain at the -180° crossing frequency is below 0 dB, implying no negative crossing as well as a positive gain margin, the system ensures stability without active damping. However, as seen in Figure 5.11(b), the gain margin is considerably small due to the influence of the resonance peak, and it needs to be raised for ensuring reliable stability. Although a reduction in the proportional gain of the controller can satisfy this requirement, this method also reduces the crossover frequency, thereby the response speed of the system being compromised. In addition, even though the system operates with stability according to the Nyquist stability criterion, the high gain of the resonance peak is not preferred in terms of the total harmonic distortion (THD).

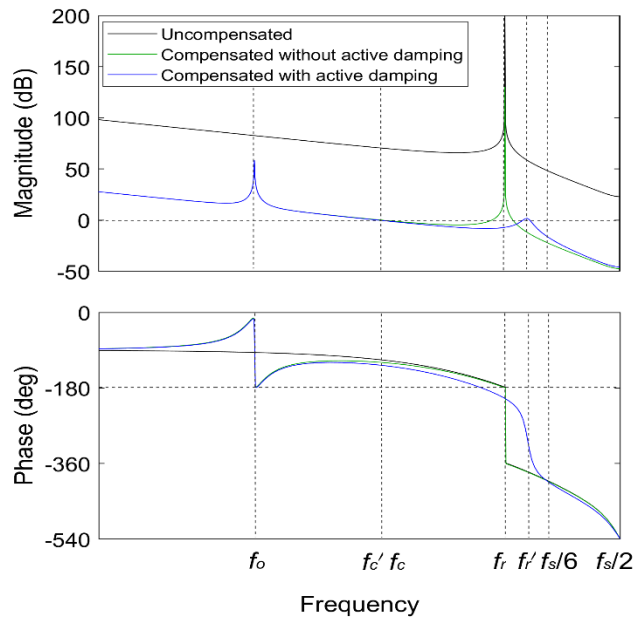


(a)

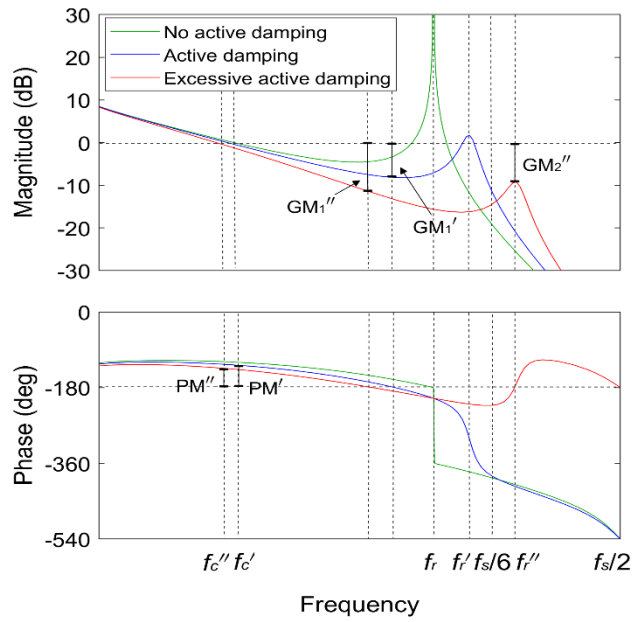


(b)

Figure 5.11. Bode diagrams of the loop gain of the system when $f_r > f_s/6$: (a) uncompensated, compensated, and compensated with active damping (b) compensated, compensated with active damping, and compensated with excessive active damping.



(a)



(b)

Figure 5.12. Bode diagrams of the loop gain of the system when $f_r < f_s/6$, $L_g = 60 \mu\text{H}$: (a) uncompensated, compensated, and compensated with active damping (b) compensated, compensated with active damping, and compensated with excessive active damping.

In an effort to increase the gain margin and dampen the resonance peak, active damping is applied to the system, and details of the result are displayed in Figure 5.11(b). First, a relatively small active damping gain, $K_{ad} = 0.0002 \text{ A}^{-1}$, is applied for active damping. As previously mentioned, the R_{eq} of the Z_{eq} equivalent to the active damping dampens down the resonance peak but is negative in the frequency range above the critical frequency $f_s/6$, generating a pair of open-loop RHP poles. The X_{eq} of the Z_{eq} displaces the intrinsic LCL filter resonance frequency f_r to the higher frequency f_r' due to its inductive characteristic in this range as shown in Figure 5.11(b). In the figure, GM_1 represents the gain margin at a -180° crossing frequency in the direction of phase falling and GM_2 indicates the gain margin at a displaced resonance frequency with a -180° crossing in the direction of phase rising due to active damping. The gain margin GM_1' is increased compared to the original gain margin of the system thanks to the active damping. However, the stability of the system is affected by a pair of open-loop RHP poles resulting from the negative R_{eq} . According to the Nyquist stability criterion $Z = P - 2(N_{(+)} - N_{(-)})$, due to the unstable open-loop pole pair $p = 2$, the number of positive -180° crossings $N_{(+)}$ should be greater than the number of the negative -180° crossings $N_{(-)}$ by one in order for the system to achieve zero closed-loop RHP pole. This requires the gain margin GM_2' at the displaced frequency f_r' to be negative, and it is met with the active damping gain $K_{ad} = 0.0002 \text{ A}^{-1}$ applied as shown in the Figure 5.11(b). Although the system with the active damping applied is stable, the resonance still causes the magnitude to rise above 1 and the enhanced gain margin GM_1' is not large enough to guarantee reliable stability.

In an attempt to apply more damping, an increased value of the active damping gain, $K_{ad} = 0.0004 \text{ A}^{-1}$, is applied. Although it leads to the slightly increased gain margin GM_1'' as shown in Figure 5.11(b), the positive GM_2'' does not contribute to generation of a positive -180°

crossing, causing a pair of unstable closed-loop RHP poles, i.e., $Z = 2$. This means that the system becomes unstable with the relatively large active damping gain, which is to be called excessive active damping. When the intrinsic resonance frequency f_r is between $f_s/6$ and $f_s/2$, the negative R_{eq} resulting from the active damping restricts the active damping gain K_{ad} to be within a substantially constrained range. In this frequency range, adjustment of the active damping gain K_{ad} requires so elaborate a task that application of active damping is practically not possible. In addition, internal component parameter variations and external impedance from a grid make it more difficult to apply active damping.

As the external inductance arising from grid impedance increases, the system resonance frequency drops to be lower than the critical frequency, $f_s/6$. As for the same VSI and the LCL filter, a grid inductance of $60 \mu\text{H}$ is considered, and its Bode diagrams are shown in Figure 5.12. Due to the addition of the grid inductance, the intrinsic LCL filter resonance frequency shifts to the frequency f_r , which is lower than the critical frequency $f_s/6$. In case the system resonance frequency f_r is lower than the critical frequency $f_s/6$ with no active damping, the phase curve crosses over -180° in the direction of phase falling at the resonance frequency f_r . Therefore, active damping must be employed to dampen the resonance peak as well as to achieve a positive gain margin for its stability. A relatively small active damping gain of $K_{ad} = 0.00015 \text{ A}^{-1}$ within the limits of $0.00006 \text{ A}^{-1} < K_{ad} < 0.00017 \text{ A}^{-1}$ obtained from Equations (5.22) and (5.24) is applied to the system, and the Bode diagrams are shown in Figure 5.12(b). There is one -180° crossing at a frequency rather lower than the resonance frequency f_r , and the gain margin GM_1' at the frequency is positive. It indicates that the system is stable, but the magnitude of the resonance peak is still above 1, which does not satisfy the general rule of keeping the high-frequency gain low for noise reduction. An increased active damping gain of $K_{ad} = 0.0004 \text{ A}^{-1}$

beyond the obtained K_{ad_max} for further active damping is applied, and it contributes to the increased gain margin $GM_{1''}$ as shown in Figure 5.12(b). However, the displaced resonance peak found at the frequency $f_{r''}$ higher than the critical frequency $f_s/6$ generates a -180° crossing in the direction of phase rising. The gain margin $GM_{2''}$ at the displaced resonance frequency $f_{r''}$ is positive. Therefore, a pair of open-loop RHP poles exists, but a positive -180° crossing does not exist due to the positive gain margin, i.e., $P = 2$, and $N_{(+)} = 0$. The Nyquist stability criterion results in $Z = 2$, a pair of unstable closed-loop RHP poles. Hence, any active damping gain K_{ad} beyond the K_{ad_max} causes excessive active damping which gives rise to instability to the system. Further attenuation of the resonance peak is no longer attainable when the displaced resonance frequency is beyond the critical frequency $f_s/6$ due to the -180° crossing in the direction of phase rising with the positive $GM_{2''}$. This is in consistence with the tightly restricted limits of the active damping gain, $0.00006 \text{ A}^{-1} < K_{ad} < 0.00017 \text{ A}^{-1}$. Thus, it is necessary to introduce a scheme which can sufficiently dampen the resonance peak for noise reduction irrespective of the location of the displaced resonance peak resulting from active damping even when it is above the critical frequency $f_s/6$.

CHAPTER 6 DELAY COMPENSATION

6.1 VSI With an LCL Filter Discrete-Time Model

It is necessary to reshape the equivalent resistance R_{eq} of Z_{eq} to be positive in the extended frequency ranging up to the Nyquist frequency $f_s/2$, which is the full controllable frequency range. One of solutions to the issue is to compensate for the time delays. If the capacitor current proportional feedback for active damping does not lag by the time delays, the equivalent resistance R_{eq} would not become negative within the Nyquist frequency. The one sample ahead estimated three-phase capacitor currents are obtained by the predictor type Kalman estimator, which can cancel out the lagging effect caused by the time delays.

The average linear model of the grid-connected VSI with an LCL filter is described from Figure 5.1 in the dq frame as

$$\begin{aligned} \frac{V_{dc}}{2} \mathbf{u}(t) &= R_i \mathbf{i}_i(t) + L_i \frac{d\mathbf{i}_i(t)}{dt} + j\omega_o L_i \mathbf{i}_i(t) + \mathbf{v}_c(t) \\ \mathbf{i}_i(t) &= \mathbf{i}_o(t) + j\omega_o C_f \mathbf{v}_c(t) + C_f \frac{d\mathbf{v}_c(t)}{dt} \\ \mathbf{v}_c(t) &= (R_o + R_g) \mathbf{i}_o(t) + (L_o + L_g) \frac{d\mathbf{i}_o(t)}{dt} + j\omega_o (L_o + L_g) \mathbf{i}_o(t) + \mathbf{v}_g(t), \end{aligned} \quad (6.1)$$

where, $\mathbf{i}_i(t)$ is the inverter-side current vector, $\mathbf{i}_o(t)$ is the grid-side current vector, $\mathbf{v}_c(t)$ is the capacitor voltage vector, $\mathbf{v}_g(t)$ is the grid voltage vector, and $\mathbf{u}(t)$ is the input vector of duty ratios d_d and d_q . The LCL filter elements L_i , C_f , and L_o are respectively the inverter-side inductance, the capacitance of the filter, and the filter grid-side inductance. The internal resistance of the inverter-side inductor is referred as R_i , and the internal resistance of the filter grid-side inductor is represented by R_o . The grid impedance comprises the inductive part L_g and the resistive part R_g . The grid fundamental frequency is denoted by ω_o .

The model in state-space notation is expressed as

$$\begin{cases} \frac{dx(t)}{dt} = Ax(t) + B_i u(t) + B_g v_g(t) \\ y(t) = Cx(t) \end{cases} \quad (6.2)$$

where

$$\begin{aligned} x(t) &= [i_{id} \ i_{iq} \ v_{cd} \ v_{cq} \ i_{od} \ i_{oq}]^T \\ y(t) &= [i_{od} \ i_{oq}]^T \end{aligned} \quad (6.3)$$

$$A = \begin{bmatrix} -\frac{R_i}{L_i} & \omega_o & -\frac{1}{L_i} & 0 & 0 & 0 \\ -\omega_o & -\frac{R_i}{L_i} & 0 & -\frac{1}{L_i} & 0 & 0 \\ \frac{1}{C_f} & 0 & 0 & \omega_o & -\frac{1}{C_f} & 0 \\ 0 & \frac{1}{C_f} & -\omega_o & 0 & 0 & -\frac{1}{C_f} \\ 0 & 0 & \frac{1}{L_o+L_g} & 0 & -\frac{R_o+R_g}{L_o+L_g} & \omega_o \\ 0 & 0 & 0 & \frac{1}{L_o+L_g} & -\omega_o & -\frac{R_o+R_g}{L_o+L_g} \end{bmatrix} \quad (6.4)$$

$$B_i = \begin{bmatrix} 0 & \frac{v_{dc}}{2L_i} & 0 & 0 & 0 & 0 \\ \frac{v_{dc}}{2L_i} & 0 & 0 & 0 & 0 & 0 \end{bmatrix}^T$$

$$B_g = \begin{bmatrix} 0 & 0 & 0 & 0 & 0 & -\frac{1}{L_o+L_g} \\ 0 & 0 & 0 & 0 & -\frac{1}{L_o+L_g} & 0 \end{bmatrix}^T$$

$$C = \begin{bmatrix} 0 & 0 & 0 & 0 & 1 & 0 \\ 0 & 0 & 0 & 0 & 0 & 1 \end{bmatrix},$$

and the superscript T denotes transpose.

For digital implementation, the proposed model is discretized with the sampling period T_s by the zero-order hold (ZOH) method as follows.

$$\begin{aligned}
A_d &= e^{AT_s} = I + \frac{AT_s}{1!} + \frac{A^2T_s^2}{2!} + \dots \\
B_{id} &= A^{-1}(A_d - I)B_i \\
B_{gd} &= A^{-1}(A_d - I)B_g \\
C_d &= C.
\end{aligned} \tag{6.5}$$

The discrete-time model of the grid-connected VSI with the LCL filter is then

$$\begin{cases} x[k+1] = A_d x[k] + B_{id} u[k] + B_{gd} v_g[k] \\ y[k] = C_d x[k]. \end{cases} \tag{6.6}$$

6.2 Design of Kalman Estimators

A discrete-time linear dynamical system is described by:

$$\begin{aligned}
x[k+1] &= A_d x[k] + B_{id} u[k] + B_{gd} v_g[k] + G_d w[k] \\
y[k] &= C_d x[k] + v[k],
\end{aligned} \tag{6.7}$$

where x , u , and y are state, input, and measurement vectors, respectively. Zero-mean white Gaussian plant and measurement noise vectors are given by w and v , respectively and assumed to be uncorrelated with each other. They have covariance matrices Q and R , respectively.

A generalized estimator and covariance of the state yield corrector, i.e., measurement update equations as [104]:

$$\hat{x}[k|k] = \hat{x}[k|k-1] + L_K[k](y[k] - C_d \hat{x}[k|k-1]) \tag{6.8a}$$

$$P[k|k] = (I - L_K[k]C_d)P[k|k-1], \tag{6.8b}$$

where I is the identity matrix, and the Kalman gain L_K is expressed as

$$L_K[k] = P[k|k-1]C_d^T(C_d P[k|k-1]C_d^T + R)^{-1}. \tag{6.9}$$

Similarly, a generalized conditional estimator and covariance of the state produce predictor, i.e., time update equations as [104]:

$$\hat{\mathbf{x}}[k + 1 | k] = \mathbf{A}_d \hat{\mathbf{x}}[k | k] + \mathbf{B}_{id} \mathbf{u}[k] + \mathbf{B}_{gd} \mathbf{v}_g[k] \quad (6.10a)$$

$$\mathbf{P}[k + 1 | k] = \mathbf{A}_d \mathbf{P}[k | k] \mathbf{A}_d^T + \mathbf{G}_d \mathbf{Q} \mathbf{G}_d^T. \quad (6.10b)$$

Substituting Equations (6.8a) and (6.8b) into Equations (6.10a) and (6.10b) yields an a priori estimator and prediction error covariance, respectively, which is the predictor type Kalman estimator.

$$\begin{aligned} \hat{\mathbf{x}}[k + 1 | k] = & \mathbf{A}_d \hat{\mathbf{x}}[k | k - 1] + \mathbf{B}_{id} \mathbf{u}[k] + \mathbf{B}_{gd} \mathbf{v}_g[k] \\ & + \mathbf{A}_d \mathbf{L}_K[k] (\mathbf{y}[k] - \mathbf{C}_d \hat{\mathbf{x}}[k | k - 1]) \end{aligned} \quad (6.11a)$$

$$\mathbf{P}[k + 1 | k] = \mathbf{A}_d (\mathbf{I} - \mathbf{L}_K[k] \mathbf{C}_d) \mathbf{P}[k | k - 1] \mathbf{A}_d^T + \mathbf{G}_d \mathbf{Q} \mathbf{G}_d^T. \quad (6.11b)$$

On the other hand, substituting Equations (6.10a) and (6.10b) into Equations (6.8a) and (6.8b) gives the filter type Kalman estimator as

$$\begin{aligned} \hat{\mathbf{x}}[k | k] = & (\mathbf{I} - \mathbf{L}_K[k + 1] \mathbf{C}_d) (\mathbf{A}_d \hat{\mathbf{x}}[k - 1 | k - 1] + \mathbf{B}_{id} \mathbf{u}[k - 1] + \mathbf{B}_{gd} \mathbf{v}_g[k - 1]) \\ & + \mathbf{L}_K[k] \mathbf{y}[k] \end{aligned} \quad (6.12a)$$

$$\mathbf{P}[k | k] = (\mathbf{I} - \mathbf{L}_K[k] \mathbf{C}_d) (\mathbf{A}_d \mathbf{P}[k - 1 | k - 1] \mathbf{A}_d^T + \mathbf{G}_d \mathbf{Q} \mathbf{G}_d^T). \quad (6.12b)$$

Steady-state Kalman gain can be found with the following two assumptions about the linear system described by Equations (6.7). One is that $(\mathbf{A}_d, \mathbf{G} \sqrt{\mathbf{Q}})$ is reachable in the sense that the eigenvalues of $\mathbf{A}_d - \mathbf{G} \sqrt{\mathbf{Q}} \mathbf{L}_1$ can be arbitrarily placed by choosing an appropriate matrix of \mathbf{L}_1 . The other is that $(\mathbf{A}_d, \mathbf{C}_d)$ is detectable in the sense that there exists a gain of \mathbf{L}_2 to locate all the eigenvalues of $\mathbf{A}_d - \mathbf{L}_2 \mathbf{C}_d$ inside the unit circle. Then, the prediction error covariance matrix obtained by Equation (6.11b) converges to a positive definite matrix \mathbf{P} , which is the unique solution to the discrete-time algebraic Riccati equation [104].

$$P = A_d \left(P - PC_d^T (C_d PC_d^T + R)^{-1} C_d P \right) A_d^T + G_d Q G_d^T. \quad (6.13)$$

Substituting this solution P into Equation (6.9) gives the steady-state Kalman gain

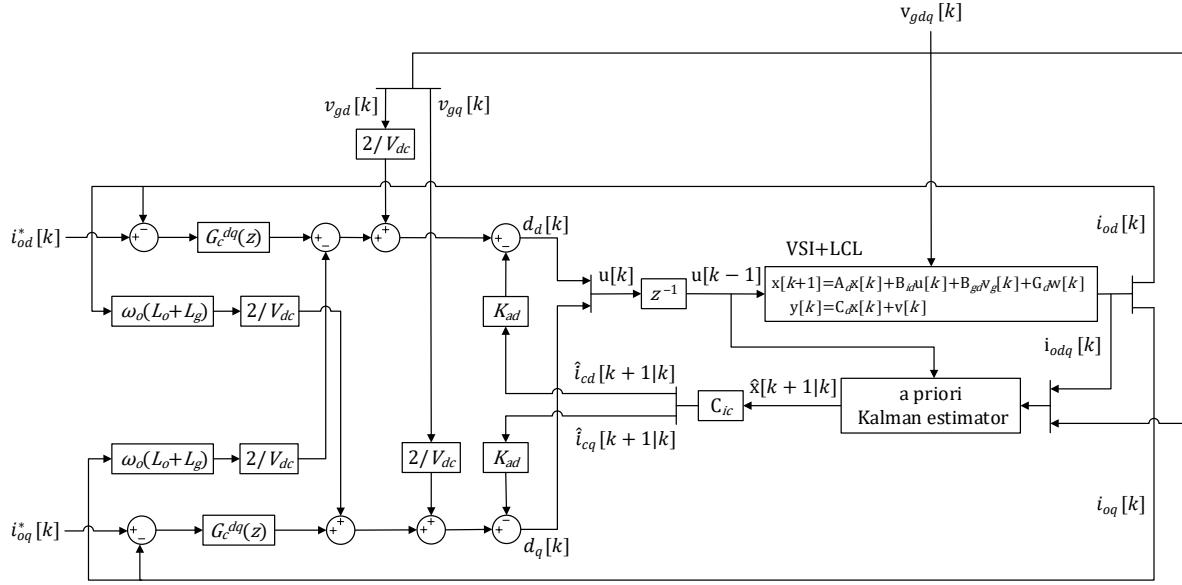
$$L_K = PC_d^T (C_d PC_d^T + R)^{-1}. \quad (6.14)$$

The proposed current-mode control for the three-phase grid-connected VSI equipped with the LCL filter is shown in Figure 6.1(a). In this approach, the grid-side currents are tightly regulated by the designed SRFPI current controller in (5.42). In order to prevent the grid harmonics from exacerbating the THD of the grid-injected currents, the measured grid voltages in the dq synchronous reference frame are scaled by a factor of $2/V_{dc}$ and introduced as feed forward signals. The real and reactive powers are controlled by the phase angle and the amplitude of the grid-side currents with respect to the grid voltages.

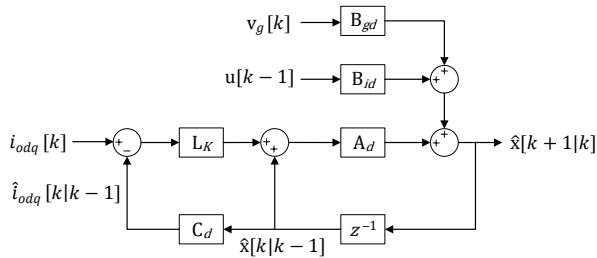
In this control scheme for active damping, the measured three-phase grid-side currents, the grid voltages, and the input signals in the dq frame are used in the Kalman estimators, both a posteriori and a priori types, to predict the states, the inverter-side currents and the grid-side currents. The Kalman estimators of a priori and a posteriori types are presented in Figure 6.1(a), (b), respectively. The estimate capacitor current vector is computed from the estimated grid-side and the inverter-side currents via a matrix of C_{ic} .

$$C_{ic} = \begin{bmatrix} 1 & 0 & 0 & 0 & -1 & 0 \\ 0 & 1 & 0 & 0 & 0 & -1 \end{bmatrix}. \quad (6.15)$$

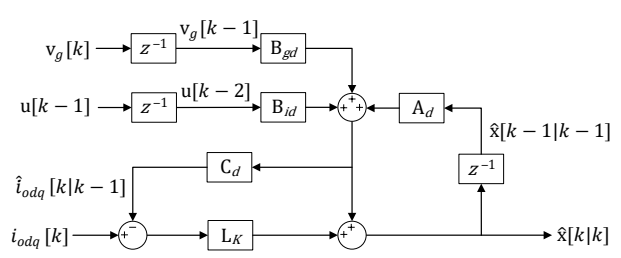
Now that the a priori type Kalman estimator reconstructs one-sample-ahead capacitor-current estimates, the computation delay is cancelled out, indicating the delay coefficient λ equal to zero in Equation (5.45). Therefore, only the duty ratio update delay, a time duration of the



(a)



(b)



(c)

Figure 6.1 (a) Proposed control system with active damping of one-sample-ahead estimated capacitor current by the Kalman a priori estimator. (b) Block diagram of the Kalman a priori estimator. (c) Block diagram of the Kalman posteriori estimator.

PWM reference being held on and compared to the triangular carrier to generate the duty cycle, is taken into account. The frequency characteristics of virtual resistance R_{eq} and reactance X_{eq} stemming from active damping using one-sample-ahead capacitor-current-estimate-proportional-negative feedback are shown in Figure 6.2. As seen, R_{eq} stays positive up to the Nyquist frequency $f_s/2$. The reactance X_{eq} remains inductive up to the Nyquist frequency as well. These

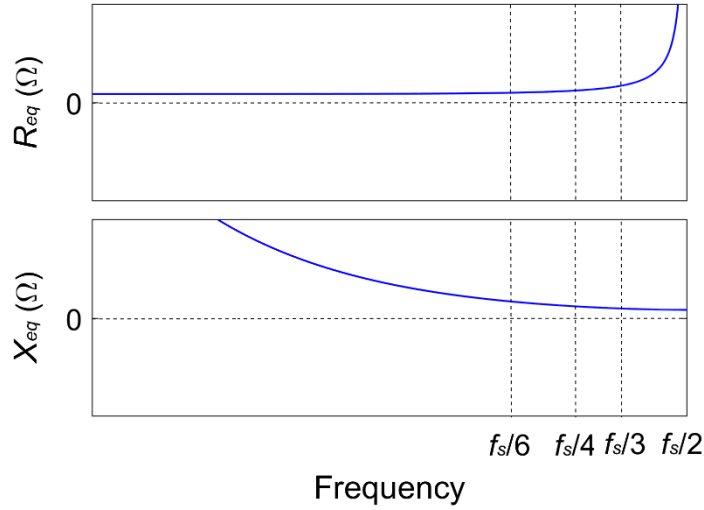
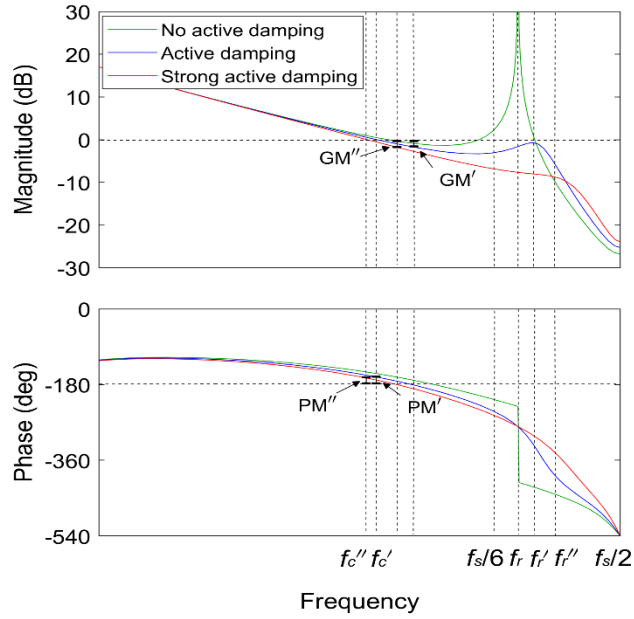


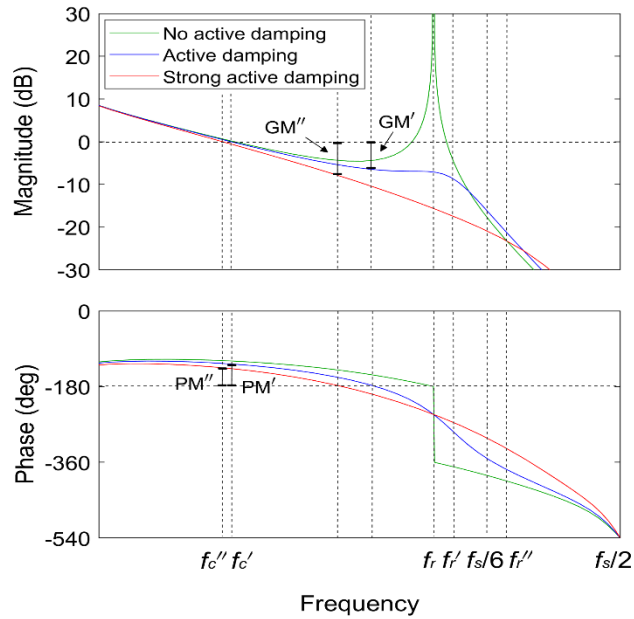
Figure 6.2. Magnitude curves of R_{eq} and X_{eq} as a function of frequency.

consequences indicate that the capacitor-current-estimate-proportional-negative-feedback active damping with no delays never generates open-loop RHP poles in the entire frequency range below the Nyquist frequency $f_s/2$. The proposed active damping method provides the full controllable frequency range for the VSI to operate regardless of the location of the displaced resonance peak while maintaining its stability.

For the system with the a priori Kalman estimator shown in Figure 6.1(b), no delay results in $\lambda = 0$ in Equation (5.45), which is incorporated into the system loop gain $T(s)$. The Bode diagrams of the system loop gain $T(z)$, a discrete equivalent of the continuous system loop gain, with three different active damping gains are shown in Figure 6.3(a). When a relatively small active damping gain applies, the magnitude of the dampened resonance peak is nearly 0 dB. Therefore, noise due to the resonance is not sufficiently attenuated. With a relatively large



(a)

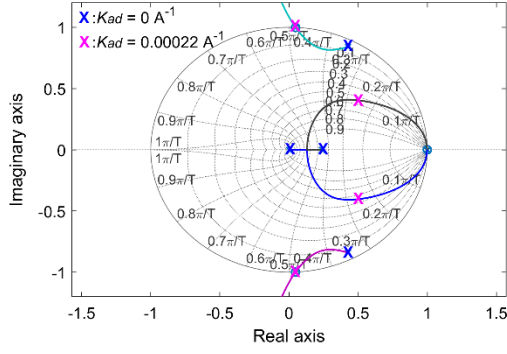


(b)

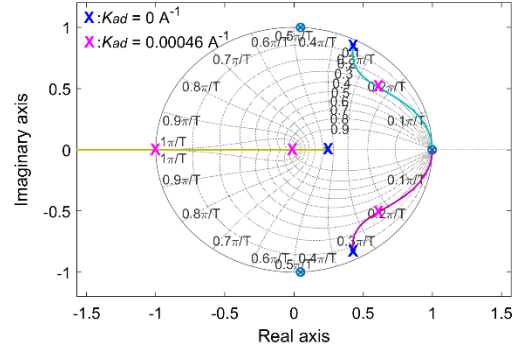
Figure 6.3. Bode diagrams of the loop gain of the system employing one-sample-ahead capacitor-current-estimate-proportional-negative feedback with active damping disabled, active damping enabled, or strong active damping enabled: (a) when $f_r > f_s/6$, (b) when $f_r < f_s/6$, $L_g = 60 \mu\text{H}$.

active damping gain, the resonance is dampened enough to have a very small amount of noise at the resonance frequency. It does not have a pair open-loop RHP poles due to the positive R_{eq} and no -180° crossing at the frequency of the displaced resonance peak. The system with active damping employing one-sample-ahead capacitor-current-estimate-proportional-negative feedback ensures its stability even when the magnitude of the resonance peak is below 0 dB. Therefore, sufficient attenuation of the resonance peak is applicable with a relatively large active damping gain, which is called strong active damping. The strong active damping also enhances its stability with the increased gain margin GM'' . With a grid inductance of $60 \mu\text{H}$ is considered, the Bode diagrams of the system loop gain $T(z)$ are shown in Figure 6.3(b). With a relatively small active gain, the resonance peak is considerably attenuated, and its peak still is below the critical frequency $f_s/6$. A further increased active damping gain shifts the peak above the critical frequency $f_s/6$, but it does not incur a -180° crossing in the direction of phase rising at the frequency of the displaced resonance peak. It indicates that open-loop RHP poles do not exist because the R_{eq} resulting from the active damping is ever positive even when the displaced resonance peak is above the critical frequency $f_s/6$. The strong active damping sufficiently dampens the resonance peak and leads to the further increased gain margin GM'' with the slightly reduced PM'' .

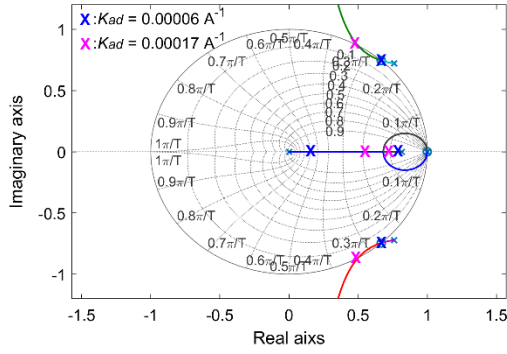
The root loci of the dual-loop system shown in Figure 5.2(b) can be viewed by plotting the denominator poles of its closed-loop transfer function as the active damping gain varies for a fixed given value of K_p . The characteristic equation of the transfer function for root locus analysis is obtained from Equation (5.44), i.e.,



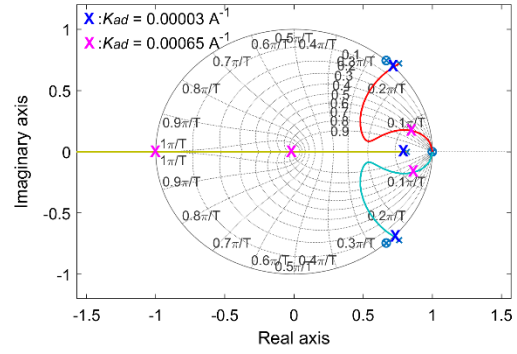
(a)



(b)



(c)



(d)

Figure 6.4 Root loci of the dual-loop control systems with respect to the active damping K_{ad} for a given K_p of 0.00024 A^{-1} . (a) With the capacitor-current-estimate-feedback active damping employing the a posteriori Kalman estimator when $f_r > f_{crit}$, $L_g = 0 \mu\text{H}$. (b) With the one-sample-ahead capacitor-current-estimate-feedback active damping employing the a priori Kalman estimator when $f_r > f_{crit}$, $L_g = 0 \mu\text{H}$. (c) The same as (a) when $f_r < f_{crit}$, $L_g = 60 \mu\text{H}$ (d) The same as (b) when $f_r < f_{crit}$, $L_g = 60 \mu\text{H}$.

$$1 + K_{ad} \frac{V_{dc}/2G_{ic}(z)}{z + K_p V_{dc}/2G_{ic}(z)[i_o(z)/i_c(z)]} = 0. \quad (6.16)$$

Of the three types of delays in Equation (5.45), the duty ratio update delay of $0.5T_s$ is ignored in this z-domain analysis for simplicity sake. For one-sample-ahead capacitor-current-estimate-proportional-negative-feedback active damping employing the a priori Kalman estimator, the

capacitor-current-estimate feedback is assumed to bypass the one-sample delay. Therefore, the forward-path transfer function of the dual-loop system is obtained as

$$\frac{i_o(z)}{i_o^e(z)} = G_c(z) \times \frac{V_{dc}/2G_{ic}(z)[i_o(z)/i_c(z)]}{z + zK_{ad}V_{dc}/2G_{ic}(z)}. \quad (6.17)$$

The PR controller function $G_c(z)$ can be reduced to K_p since the effect of the resonance gain is negligible above the fundamental frequency. Then, the denominator of the closed-loop transfer function is expressed as

$$z + zK_{ad}V_{dc}/2G_{ic}(z) + K_pV_{dc}/2G_{ic}(z)[i_o(z)/i_c(z)] = 0. \quad (6.18)$$

The characteristic equation for root locus analysis is obtained from Equation (6.18), i.e.,

$$1 + K_{ad} \frac{zV_{dc}/2G_{ic}(z)}{z + K_pV_{dc}/2G_{ic}(z)[i_o(z)/i_c(z)]} = 0. \quad (6.16)$$

Figure 6.4 shows the closed-loop pole movement with respect to the active damping gain K_{ad} with the dual-loop control systems for a fixed given K_p of 0.00024 A^{-1} . Figure 6.4(a) and (b) correspond to the systems with no grid inductance involved. Then, their resonance peaks are higher than the critical frequency f_{crit} , where the systems are initially stable without active damping. The poles initially track well inside the unit circle until too much active damping gain is applied. This is in agreement with the Bode diagram in Figure 5.11 in which the gain margin can be positive by adjusting K_p without active damping. The one-sample-ahead capacitor-current-estimate-feedback active damping gives the system a broader range of the active damping gain $0 \text{ A}^{-1} < K_{ad} < 0.00046 \text{ A}^{-1}$ which ensures its stability compared to that of the capacitor-current-estimate-feedback active damping system. This explains very well the strong active damping effect represented in the Bode diagram for the one-sample-ahead capacitor-current-estimate active damping. The strong active damping also allows a relatively large

damping ratio, which ensures sufficient resonance damping in contrast to the very low damping ratio 0.1 of the capacitor-current-feedback active damping system. Therefore, the capacitor-current-feedback active damping system hardly attenuates the resonance oscillation because the magnitude at the displaced resonance frequency should be above 0 dB in order to maintain system stability.

The root loci in Figure 6.4(c) and (d) clearly show that when the resonance frequency, f_r , is below the critical frequency, f_{crit} , due to a grid inductance of 60 μH , active damping is mandatory to achieve a stable system. The poles of the system originate outside the unit circle. Increasing the active damping gain K_{ad} forces the poles to move inside the unit circle until too much active damping gain is applied, and the system becomes stable. Although both the active damping schemes render the system to become stable in the allowable ranges, one-sample-ahead capacitor-current-estimate-feedback active damping yields a much more extended range $0.00003 \text{ A}^{-1} < K_{ad} < 0.00065 \text{ A}^{-1}$ compared to $0.00006 \text{ A}^{-1} < K_{ad} < 0.00017 \text{ A}^{-1}$ for the capacitor-current-feedback active damping. In addition, one-sample-ahead capacitor-current-estimate-feedback active damping permits a very high damping ratio beyond 0.9, which is significantly larger than a maximum damping ratio below 0.1 incurred by the capacitor-current-feedback active damping. Strong active damping that is available by the a priori Kalman estimator ensures completely damped resonance and robustness against variations in system parameters.

6.3 Simulation Results When f_r is Above f_{crit}

The need for and the benefits of the one-sample-ahead active damping, when the resonance frequency f_r is above the critical frequency f_{crit} , are well demonstrated in Figure 6.5. It shows that the system stably operates without resonance before the active damping is disabled.

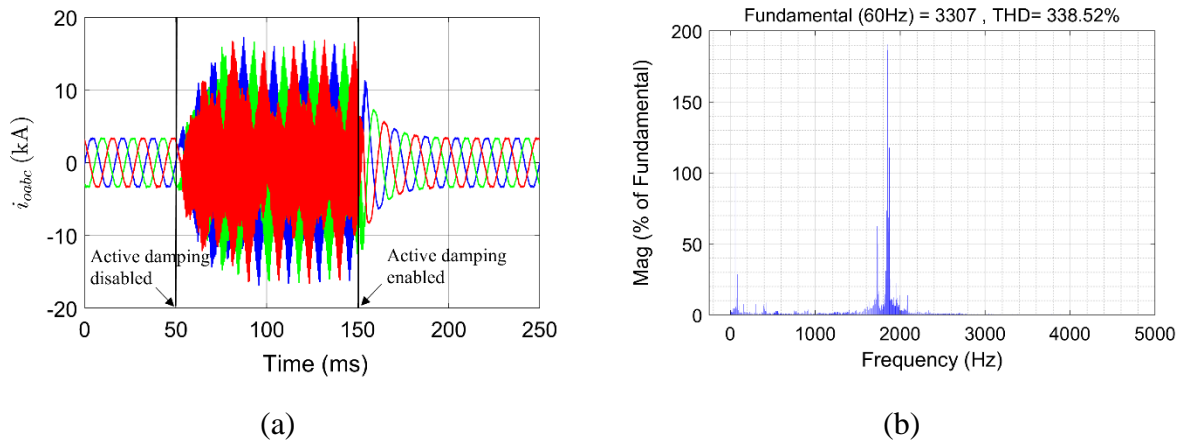
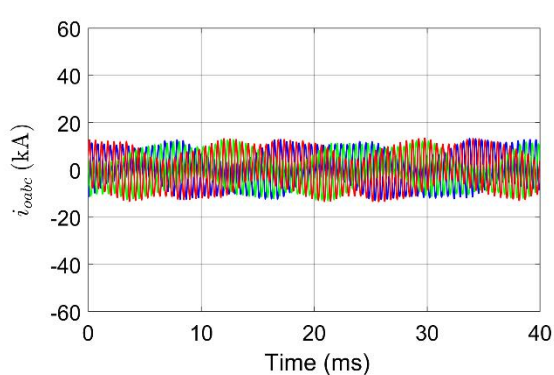


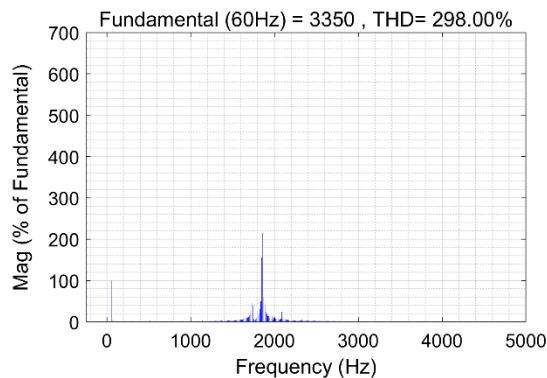
Figure 6.5 (a) Grid-injected three-phase currents when $f_r > f_{crit}$, and the one-sample-ahead capacitor-current-estimate active damping is disabled at 50 ms and enabled at 150 ms. (b) Current THD after active damping is disabled.

Once the active damping is disabled, large resonant currents ensue even though the system still remains stable, which is confirmed by the current THD in Figure 6.5(b). Therefore, even when the resonance frequency f_r is above the critical frequency f_{crit} , active damping is necessary to dampen the resonance.

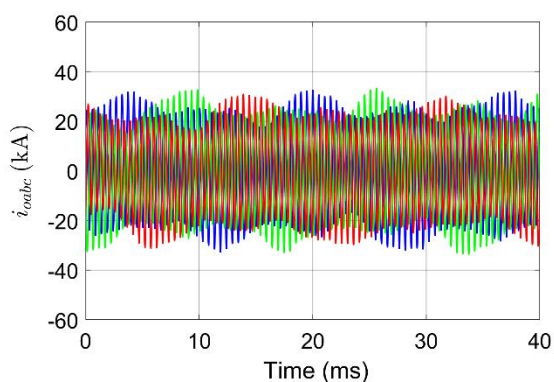
Simulation studies for the LCL filter systems are performed with no grid impedance, representing a worst case scenario and, thus, it requires more effective damping to obtain low THD output currents. Simulations are carried out with Matlab/Simulink using a two-level three-phase inverter model, connected with a stiff grid. For comparison sake, three types of capacitor-current active damping are used for the LCL filter system described in Table 5.1, and the results are compared. One is capacitor-current-proportional-negative-feedback active damping using directly measured three-phase capacitor currents. Another is capacitor-current-estimate-proportional-negative-feedback active damping employing the a posteriori Kalman estimator. The other is one-sample-ahead capacitor-current-estimate-proportional-negative-feedback active damping utilizing the a priori Kalman estimator.



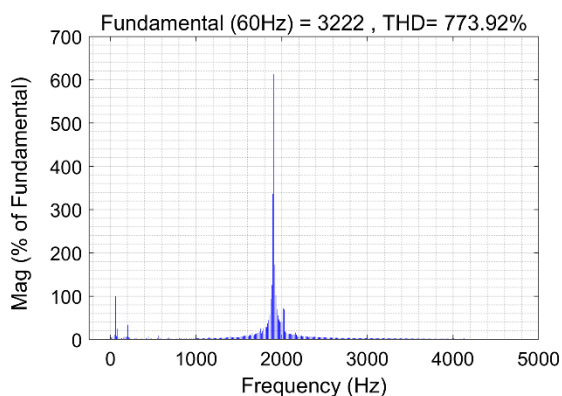
(a)



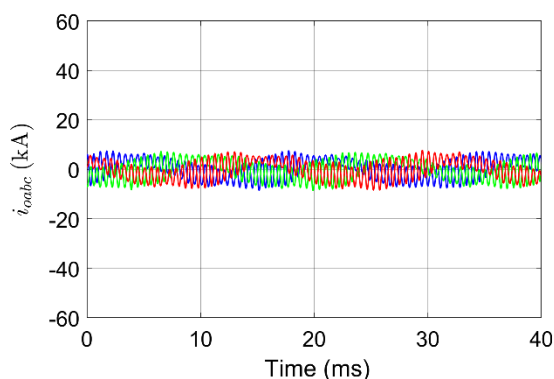
(b)



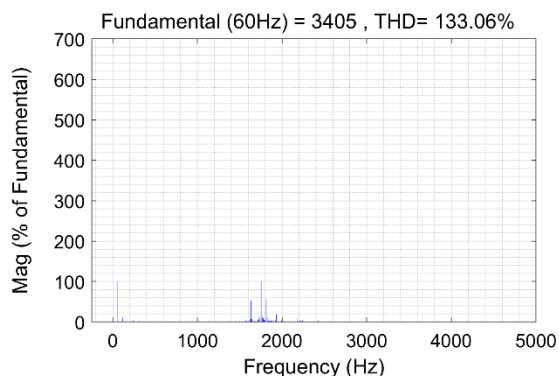
(c)



(d)



(e)



(f)

Figure 6.6 Grid-side three-phase currents for three different types of active damping schemes with an active damping gain of $K_{ad} = 0.0001 \text{ A}^{-1}$ when $f_r > f_{crit}$. (a) Capacitor-current-feedback active damping. (b) Current THD. (c) Capacitor-current-estimate-feedback active damping. (d) Current THD. (e) One-sample-ahead capacitor-current-estimate-feedback active damping. (f) Current THD.

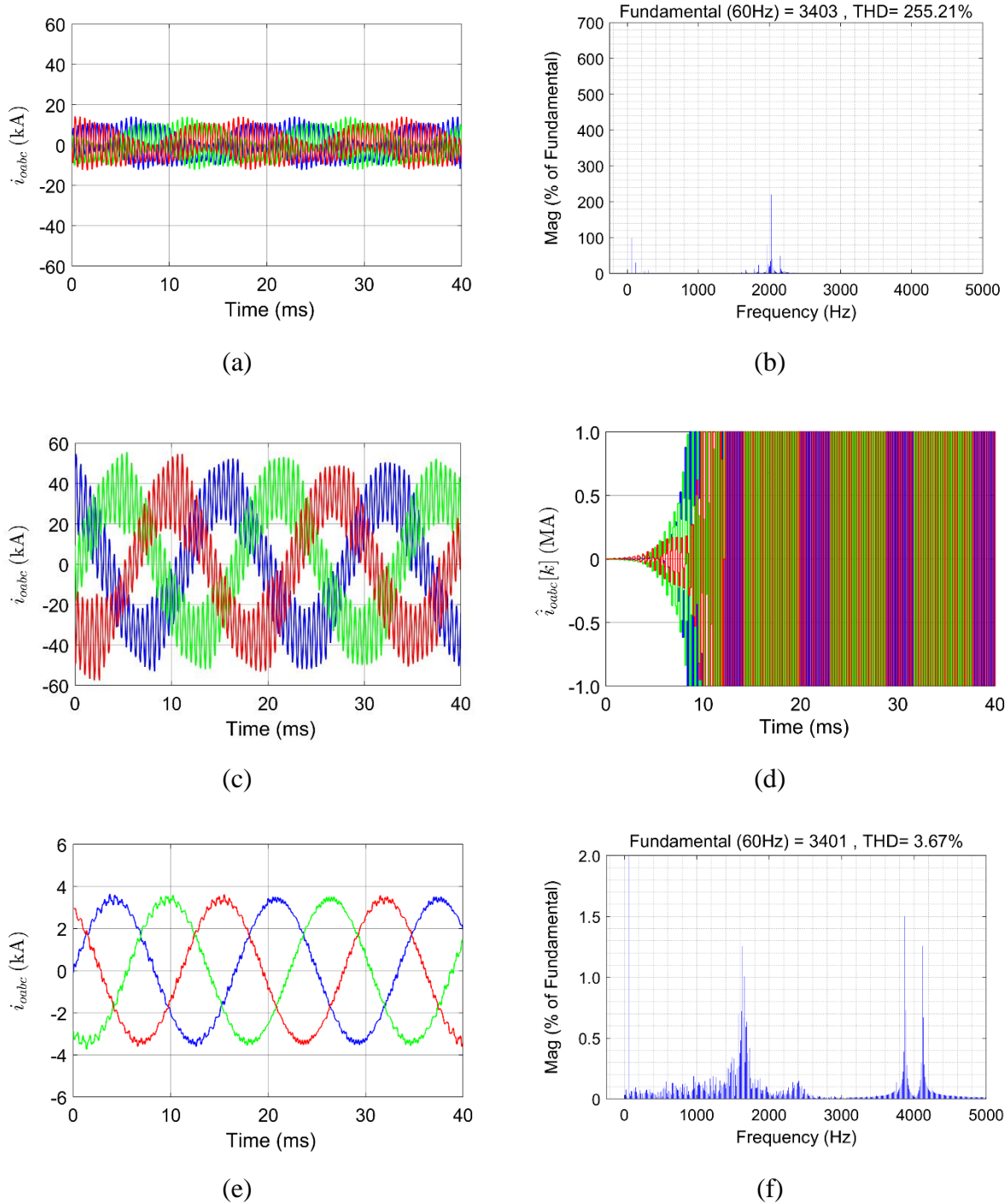


Figure 6.7 Grid-side three-phase currents for three different types of active damping schemes with an increased active damping gain of $K_{ad} = 0.0003 \text{ A}^{-1}$ when $f_r > f_{crit}$. (a) Capacitor-current-feedback active damping. (b) Current THD. (c) Capacitor-current-estimate-feedback active damping. (d) Current THD. (e) One-sample-ahead capacitor-current-estimate-feedback active damping. (f) Current THD.

The formal expressions for the Kalman Estimators include two matrices, plant noise vector w and measurement noise vector v , representing the amount of covariance for the vectors. Setting values for the covariance matrices Q and R of w and v , respectively, is an important step because it adjusts a tradeoff between estimator robustness and estimator filtering performance. One of the usual approaches in selecting an R matrix is to estimate its variance under the assumption that the noise is white and Gaussian. In selecting a Q matrix, some thumb rules can be used. Small values in Q mean that the system modeling is so accurate that the output responses and the states match the theoretical model very well. Such a Kalman estimator has an ability of effectively removing noise from measurements. One drawback caused by low values in Q is potential large bias errors on the output estimates and the states. In contrast, greater Q values reduce bias errors at the cost of degraded filtering performance.

The Simulation results show that when the resonance frequency f_r is above the critical frequency f_{crit} significant resonance oscillation ensues with a relatively small active damping gain of $K_{ad} = 0.0001 \text{ A}^{-1}$ for all three active damping schemes. First of all, the capacitor-current-feedback active damping system results are not consistent. The simulation results are not in agreement with the analysis results of the frequency domain Bode plots and the root loci. This is due to the inverter switching actions, which cause the capacitor current to change its polarity with the switching instant. The stability analyses performed in the s-domain do not incorporate the switching effects. Therefore, there must be critical discrepancies between the analyses and the simulation/experiment results.

For the capacitor-current active damping system and the capacitor-current-estimate active damping system, within the obtained bounds of the active damping gain K_{ad} which ensure system stability, resonance oscillation cannot be reduced enough to produce appropriate output currents.

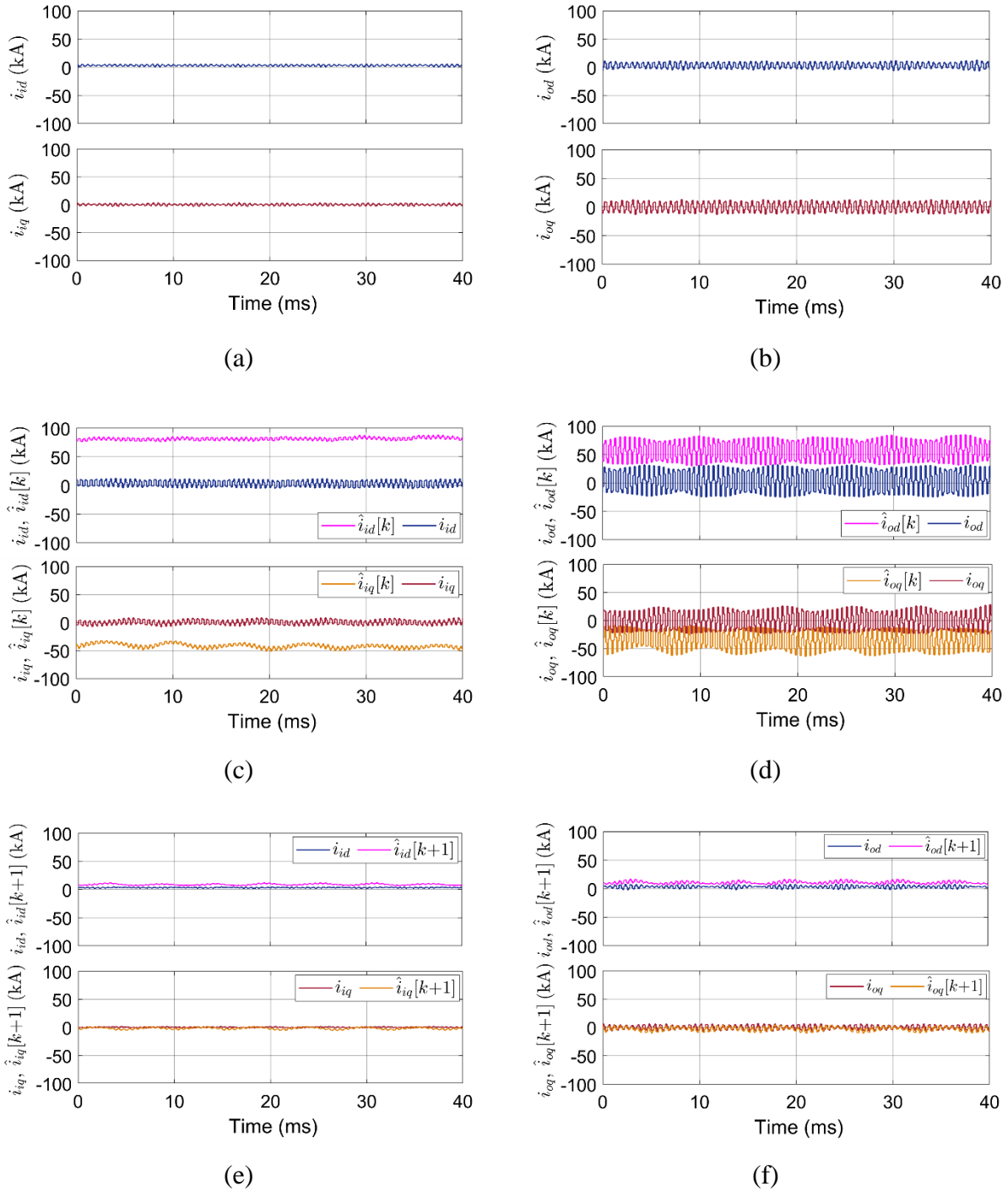


Figure 6.8 Three-phase currents and their estimates in the dq frame for three different types of active damping schemes with an active damping gain of $K_{ad} = 0.0001 \text{ A}^{-1}$ when $f_r > f_{crit}$. Capacitor-current-feedback active damping: (a) inverter-side currents, (b) grid-side currents. Capacitor-current-estimate-feedback active damping: (c) inverter-side currents, (d) grid-side currents. One-sample-ahead capacitor-current-estimate-feedback active damping: (e) Inverter-side currents (f) Grid-side currents.

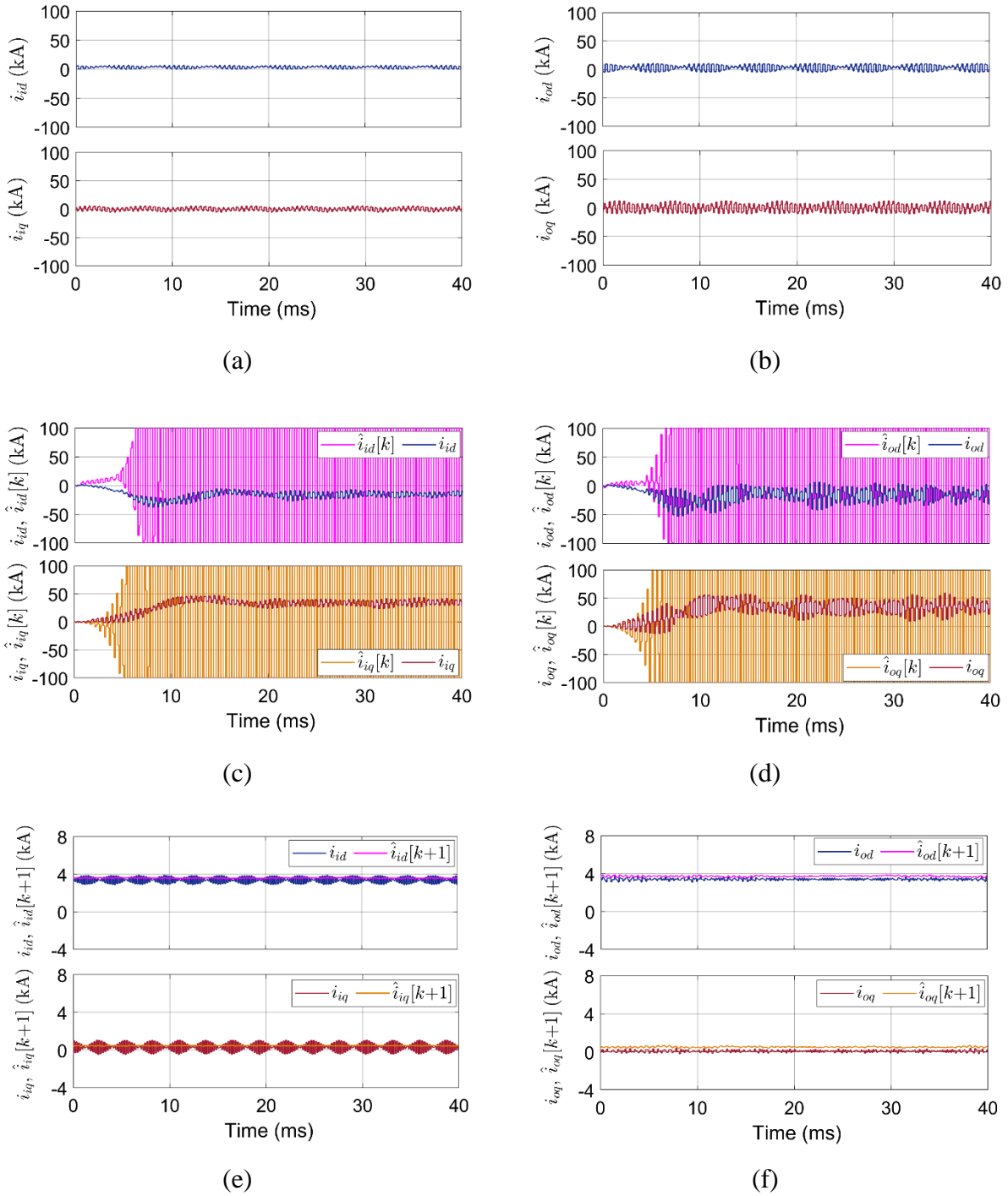


Figure 6.9 Three-phase currents and their estimates in the dq frame for three different types of active damping schemes with an increased active damping gain of $K_{ad} = 0.0003 \text{ A}^{-1}$ when $f_r > f_{crit}$. Capacitor-current-feedback active damping: (a) inverter-side currents, (b) grid-side currents. Capacitor-current-estimate-feedback active damping: (c) inverter-side currents, (d) grid-side currents. One-sample-ahead capacitor-current-estimate-feedback active damping: (e) Inverter-side currents (f) Grid-side currents.

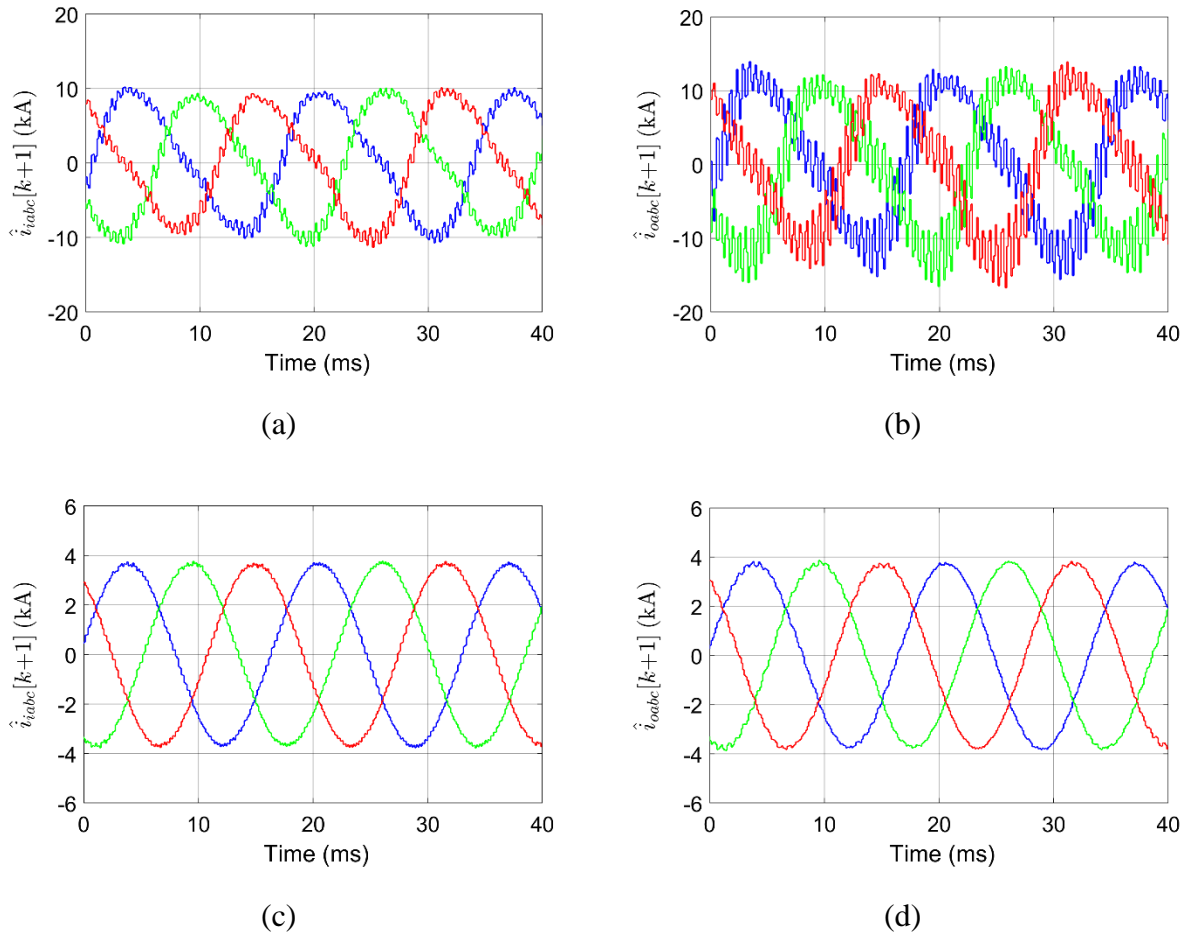
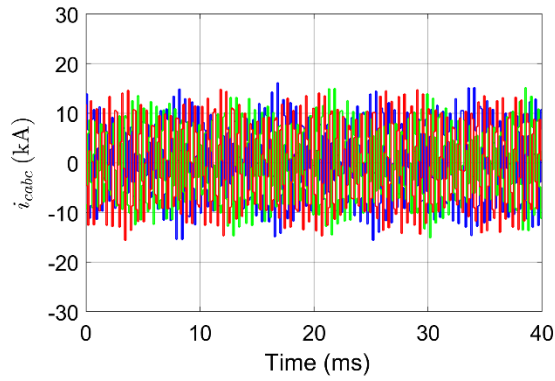
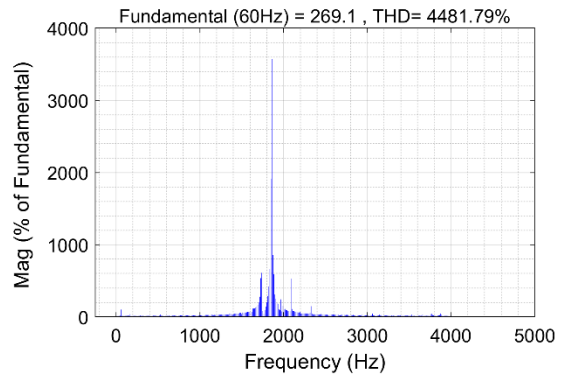


Figure 6.10 One-sample-ahead-current estimates for the one-sample-ahead capacitor-current-estimate-feedback active damping system. With an active damping gain of $K_{ad} = 0.0001 \text{ A}^{-1}$: (a) inverter-side current estimates, (b) grid-side current estimates. With an increased active damping gain of $K_{ad} = 0.0003 \text{ A}^{-1}$: (c) inverter-side current estimates, (d) grid-side current estimates.

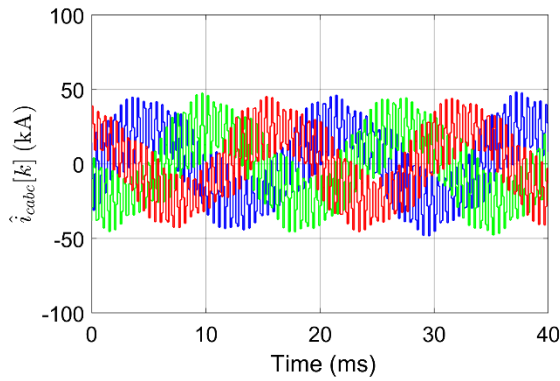
For the capacitor-current-estimate active damping system, once the active damping gain goes beyond the maximum value, the system becomes unstable, which is verified with the current estimates increasing to infinity shown in Figure 6.9(c) and (d). Excessive active damping with an active damping gain of $K_{ad} = 0.0003 \text{ A}^{-1}$ results in instability of the system. However, the one-sample delay compensated active damping system employing the a priori Kalman estimator enables further damping until the resonance is sufficiently attenuated ensuring stability.



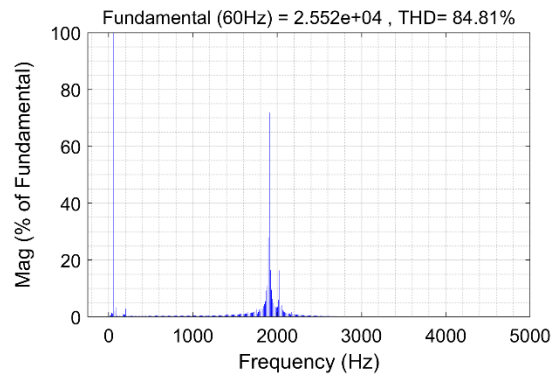
(a)



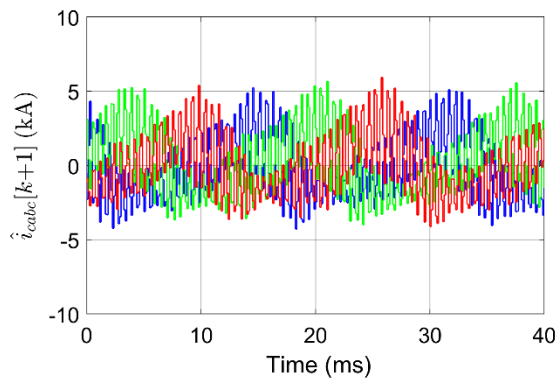
(b)



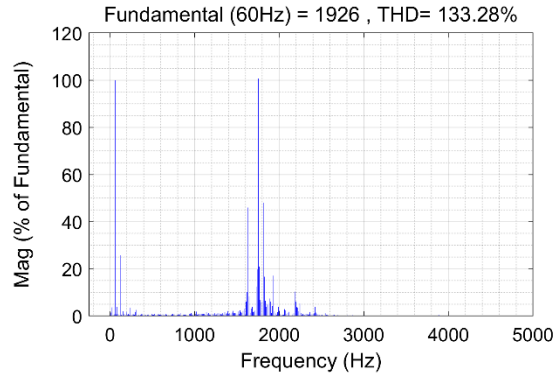
(c)



(d)

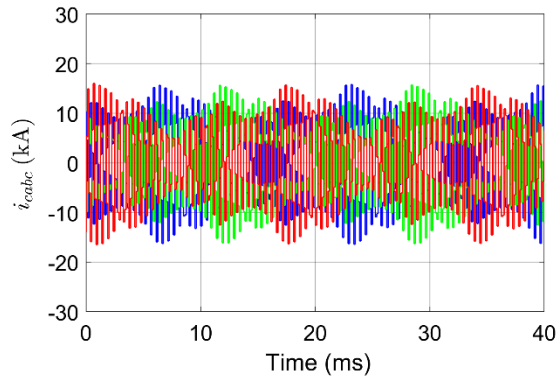


(e)

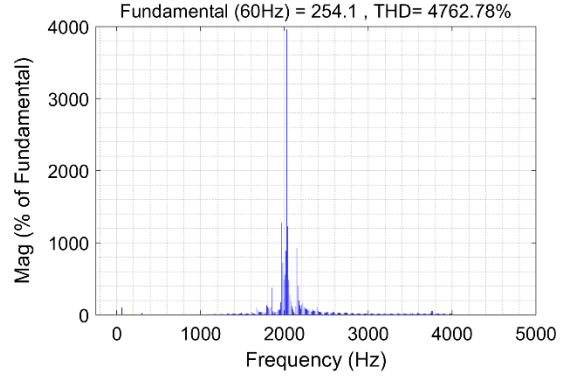


(f)

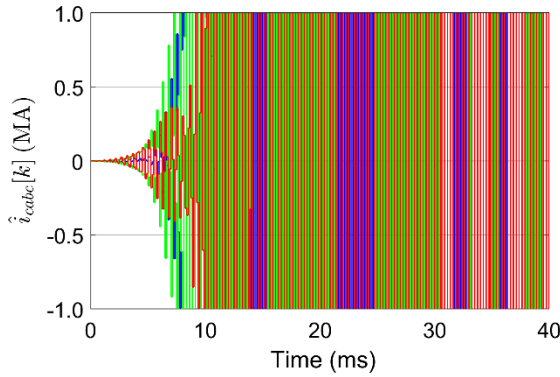
Figure 6.11 Three-phase capacitor currents or estimates for three different types of active damping schemes with an active damping gain of $K_{ad} = 0.0001 \text{ A}^{-1}$ when $f_r > f_{crit}$. Capacitor-current-feedback active damping: (a) measured capacitor currents, (b) current THD. Capacitor-current-estimate-feedback active damping: (c) capacitor-current estimates, (d) current THD. One-sample-ahead capacitor-current-estimate-feedback active damping: (e) one-sample-ahead capacitor-current estimates, (f) current THD.



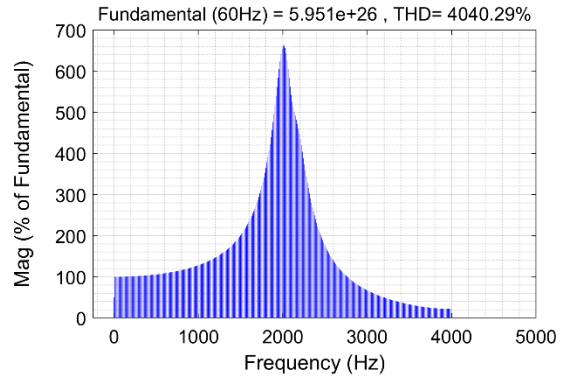
(a)



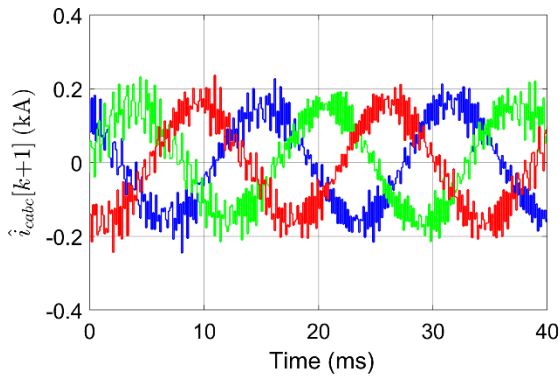
(b)



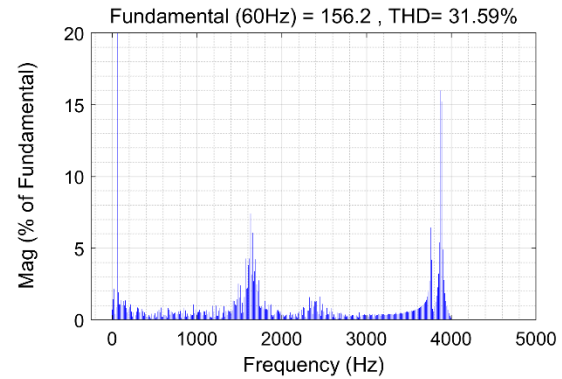
(c)



(d)



(e)



(f)

Figure 6.12 Three-phase capacitor currents or estimates for three different types of active damping schemes with an active damping gain of $K_{ad} = 0.0003 \text{ A}^{-1}$ when $f_r > f_{crit}$. Capacitor-current-feedback active damping: (a) measured capacitor currents, (b) current THD. Capacitor-current-estimate-feedback active damping: (c) capacitor-current estimates, (d) current THD. One-sample-ahead capacitor-current-estimate-feedback active damping: (e) one-sample-ahead capacitor-current estimates, (f) current THD.

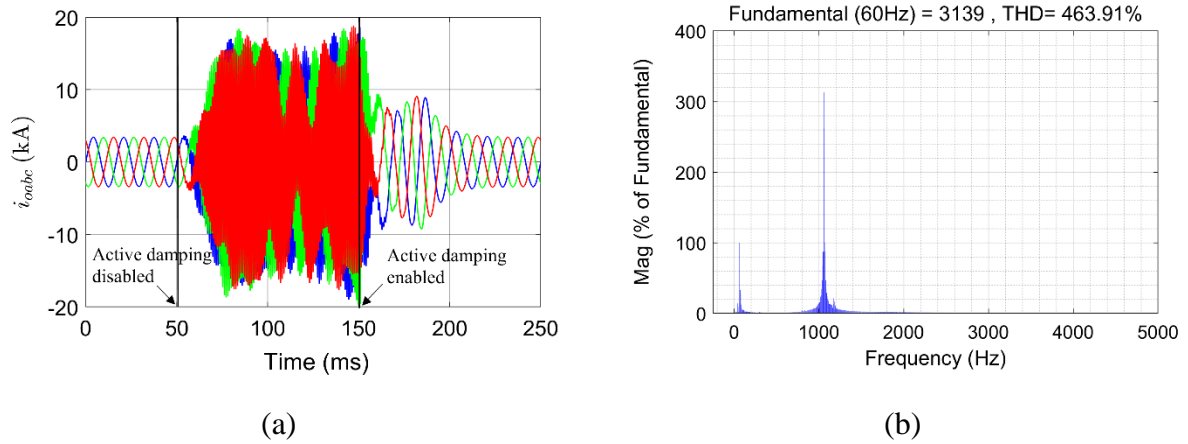
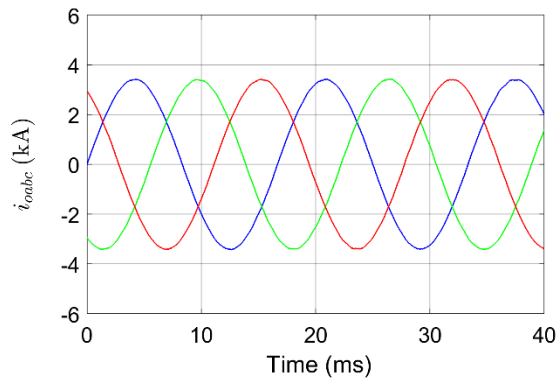


Figure 6.13 (a) Grid-injected three-phase currents when $f_r < f_{crit}$ with a grid inductance of $60 \mu\text{H}$, and the one-sample-ahead capacitor-current-estimate-feedback active damping is disabled at 50 ms and enabled at 150 ms. (b) Current THD after active damping is disabled.

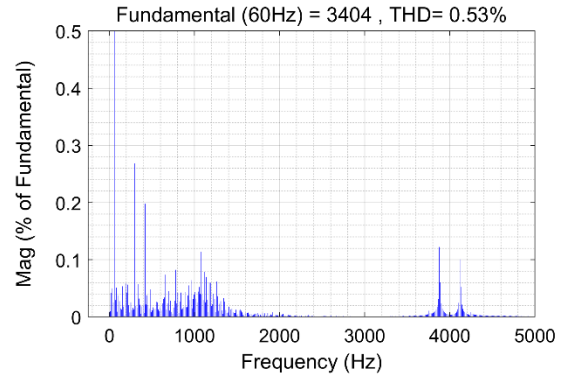
6.4 Simulation Results When f_r is Below f_{crit}

The THD of the grid-side current can be decreased to about 3 % with a strong active damping gain available up to the extended maximum active damping gain $K_{ad} = 0.00046 \text{ A}^{-1}$. This enhancement is achieved primarily by the one-sample-ahead capacitor-current estimates which do not include any components resulting from the inverter switching actions. In Figure 6.12(e), the capacitor-current estimates which are obtained by the a priori Kalman estimator with an increased active damping gain of $K_{ad} = 0.0003 \text{ A}^{-1}$ look proper sinusoids compared to those of two other active damping systems.

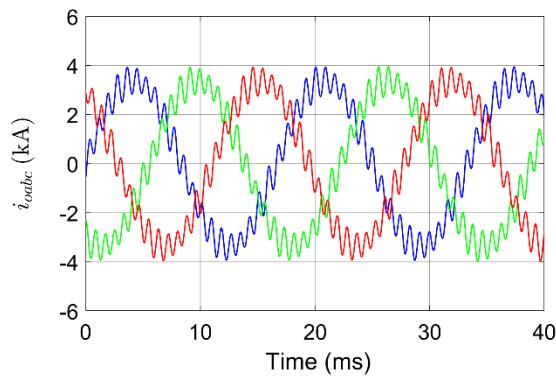
Another set of simulations is carried out when the resonance frequency f_r is below the critical frequency f_{crit} , which is obtained with an added grid inductance of $60 \mu\text{H}$. Figure 6.13 demonstrates active damping is required for the system of which resonance frequency is below the critical frequency f_{crit} . Once the one-sample-ahead capacitor-current active damping using the a priori Kalman estimator is disabled, the currents oscillate and the system becomes unstable.



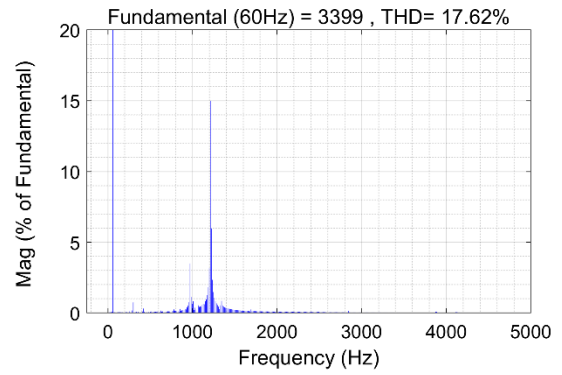
(a)



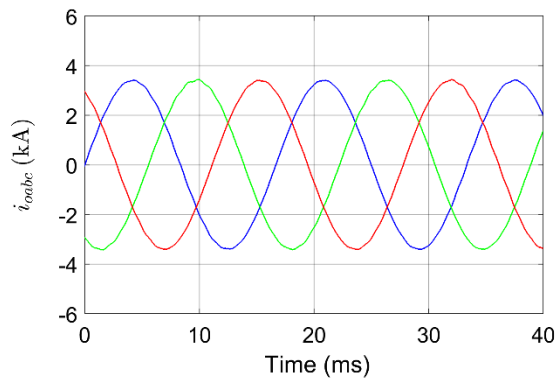
(b)



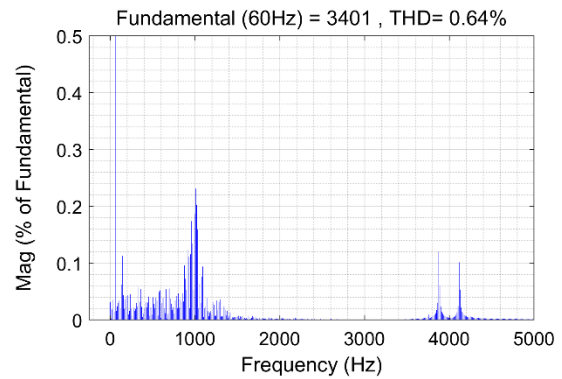
(c)



(d)



(e)



(f)

Figure 6.14 Grid-side three-phase currents for three different types of active damping schemes with an active damping gain of $K_{ad} = 0.0001 \text{ A}^{-1}$ when $f_r < f_{crit}$ with a grid inductance of $60 \mu\text{H}$ (a) Capacitor-current-feedback active damping. (b) Current THD. (c) Capacitor-current-estimate-feedback active damping. (d) Current THD. (e) One-sample-ahead capacitor-current-estimate-feedback active damping. (f) Current THD.

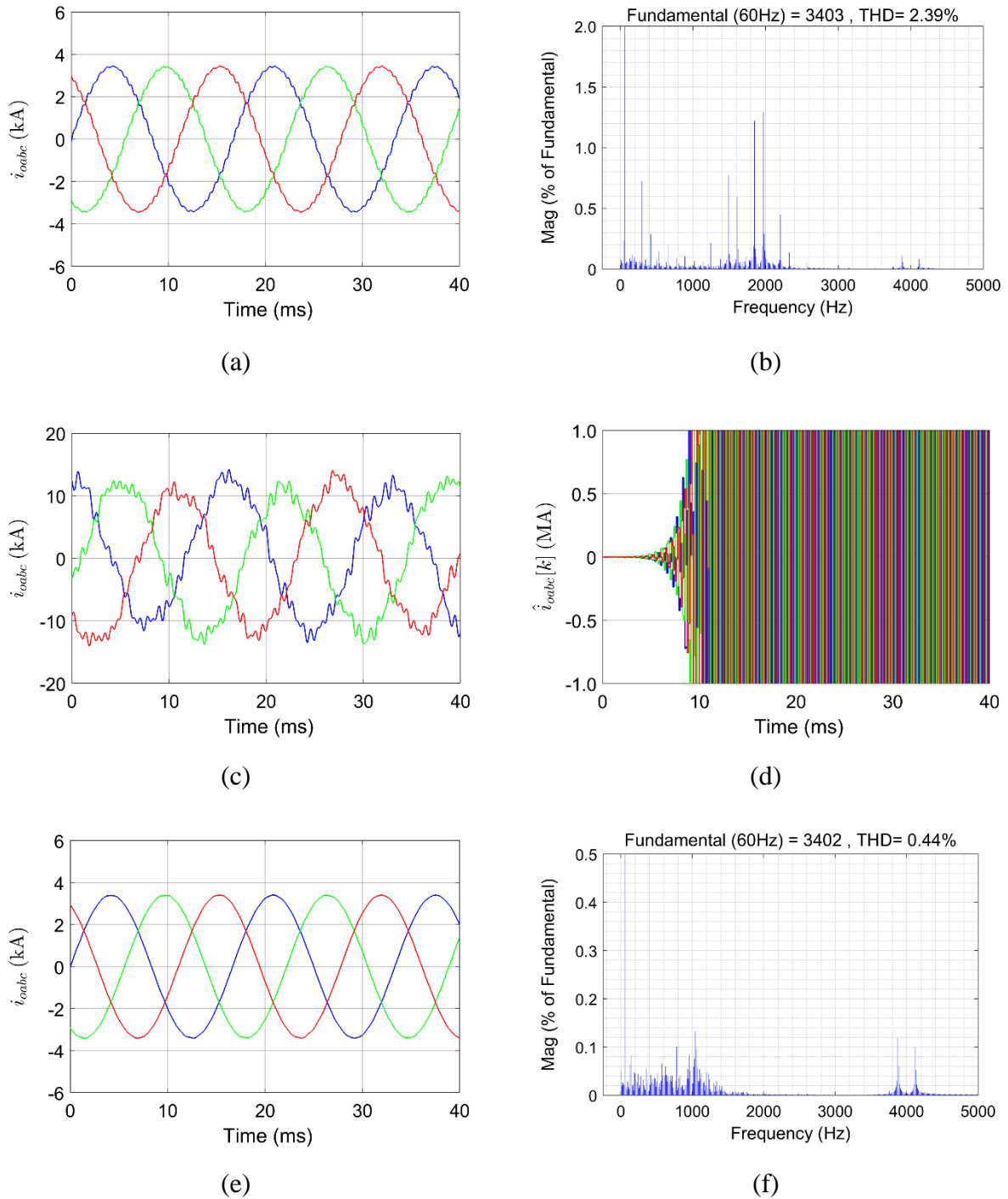


Figure 6.15 Grid-side three-phase currents for three different types of active damping schemes with an increased active damping gain of $K_{ad} = 0.0003 \text{ A}^{-1}$ when $f_r < f_{crit}$ with a grid inductance of $60 \mu\text{H}$. (a) Capacitor-current-feedback active damping. (b) Current THD. (c) Capacitor-current-estimate-feedback active damping. (d) Current THD. (e) One-sample-ahead capacitor-current-estimate-feedback active damping. (f) Current THD.

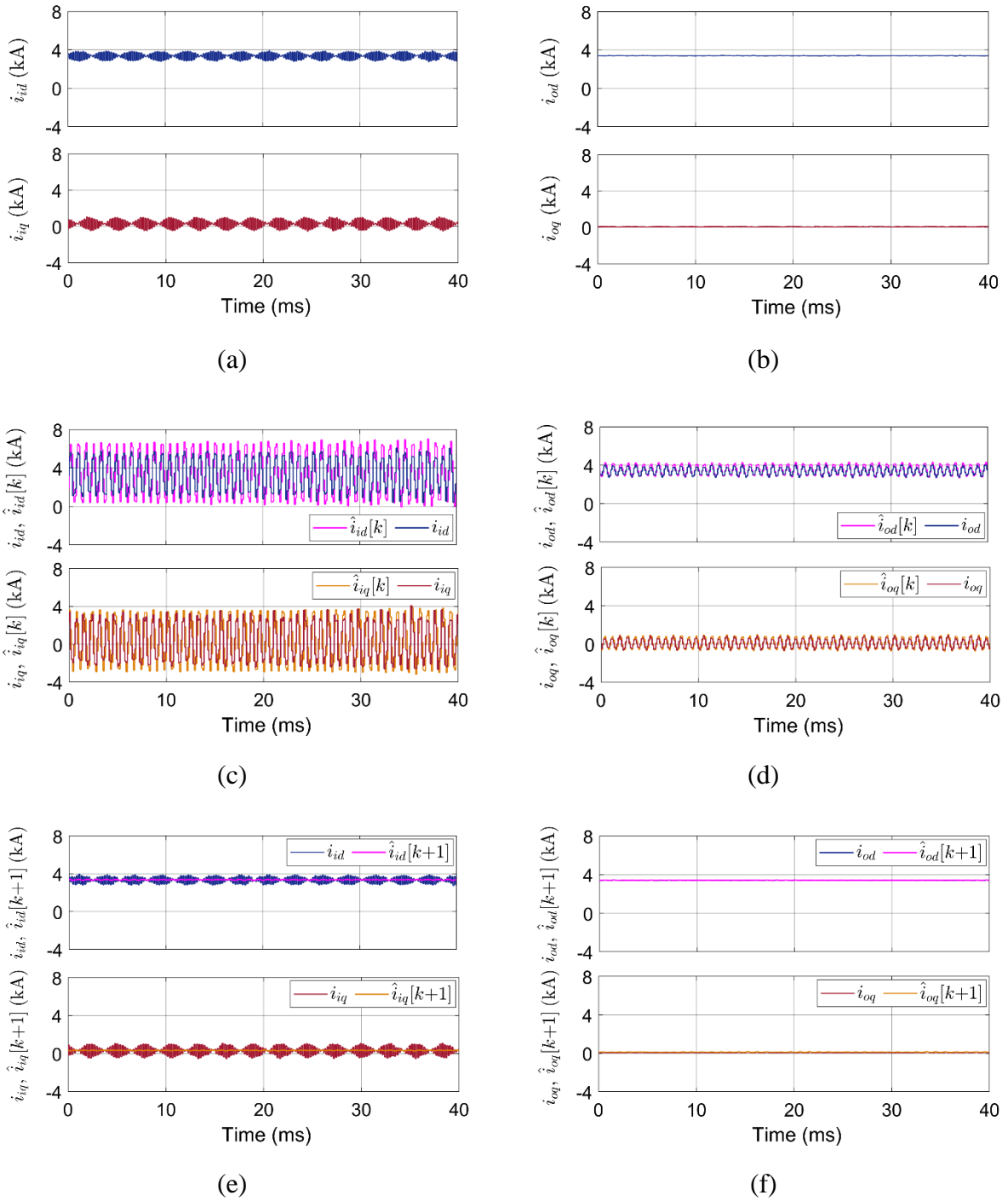
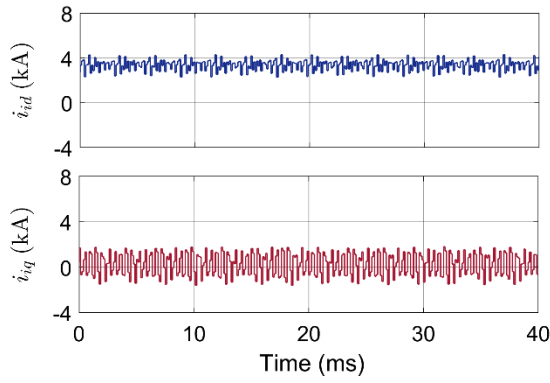
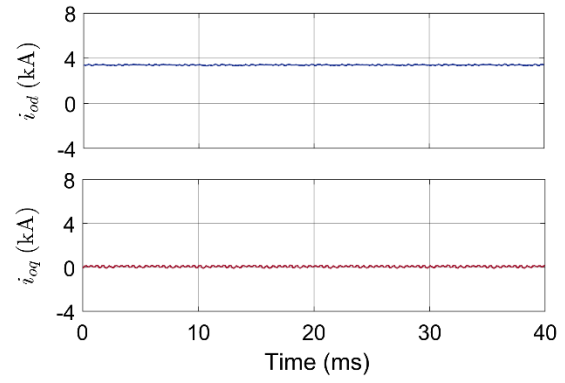


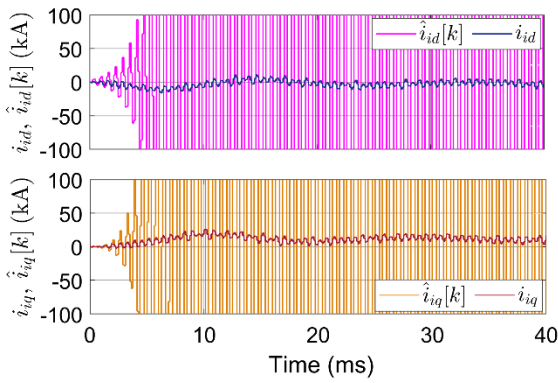
Figure 6.16 Three-phase currents and their estimates in the dq frame for three different types of active damping schemes with an active damping gain of $K_{ad} = 0.0001 \text{ A}^{-1}$ when $f_r < f_{crit}$ with a grid inductance of $60 \mu\text{H}$. Capacitor-current-feedback active damping: (a) inverter-side currents, (b) grid-side currents. Capacitor-current-estimate-feedback active damping: (c) inverter-side currents, (d) grid-side currents. One-sample-ahead capacitor-current-estimate-feedback active damping: (e) Inverter-side currents (f) Grid-side currents.



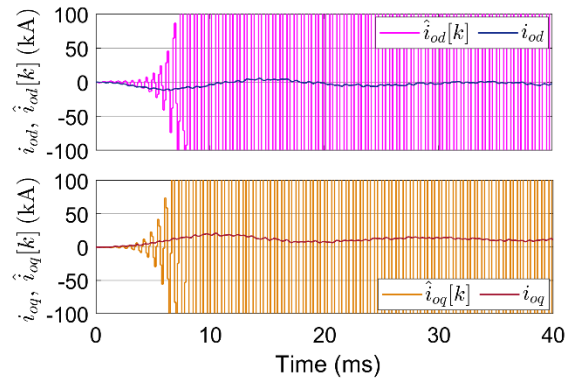
(a)



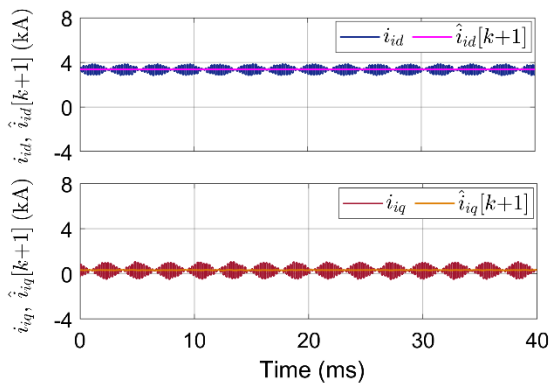
(b)



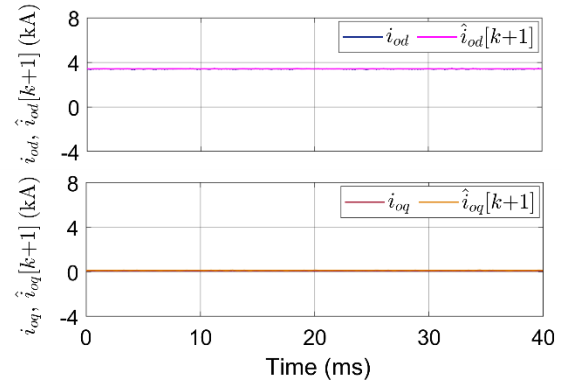
(c)



(d)



(e)



(f)

Figure 6.17 Three-phase currents and their estimates in the dq frame for three different types of active damping schemes with an increased active damping gain of $K_{ad} = 0.0003 \text{ A}^{-1}$ when $f_r < f_{crit}$ with a grid inductance of $60 \mu\text{H}$. Capacitor-current-feedback active damping: (a) inverter-side currents, (b) grid-side currents. Capacitor-current-estimate-feedback active damping: (c) inverter-side currents, (d) grid-side currents. One-sample-ahead capacitor-current-estimate-feedback active damping: (e) Inverter-side currents (f) Grid-side currents.

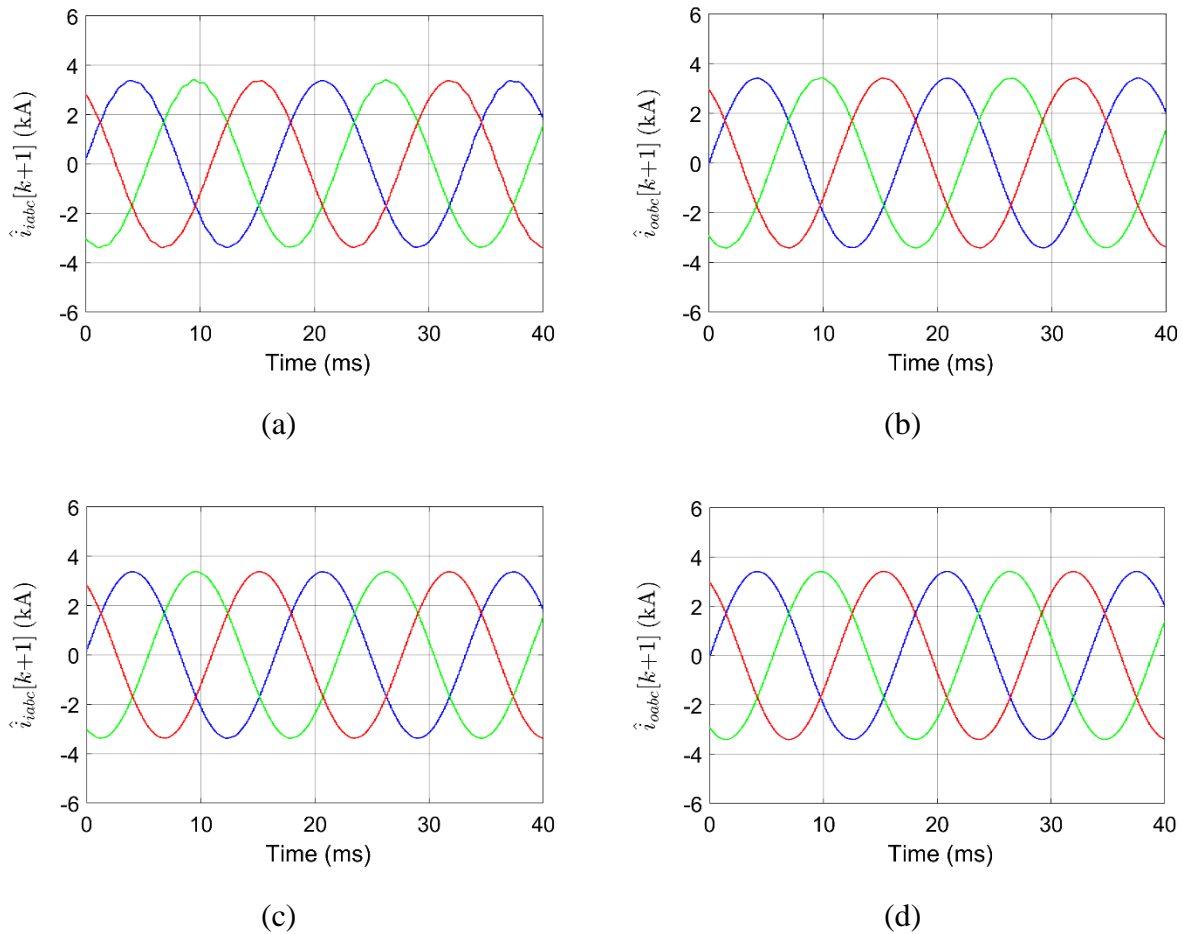


Figure 6.18 One-sample-ahead-current estimates for the one-sample-ahead capacitor-current-estimate-feedback active damping system. With an active damping gain of $K_{ad} = 0.0001 \text{ A}^{-1}$: (a) inverter-side current estimates, (b) grid-side current estimates. With an increased active damping gain of $K_{ad} = 0.0003 \text{ A}^{-1}$: (c) inverter-side current estimates, (d) grid-side current estimates.

With no active damping applied, the system is initially unstable because the complex poles are outside the unit circle as seen in the root locus. For the capacitor-current-estimate active damping system, the resonance is not sufficiently attenuated. This result well explains the root loci of the system, where the complex roots barely track inside the unit circle providing a maximum damping ratio lower than 0.1 seen in Figure 6.4(c). When the active damping gain K_{ad} is greater than the maximum bound, the current estimates grow to infinity meaning instability.

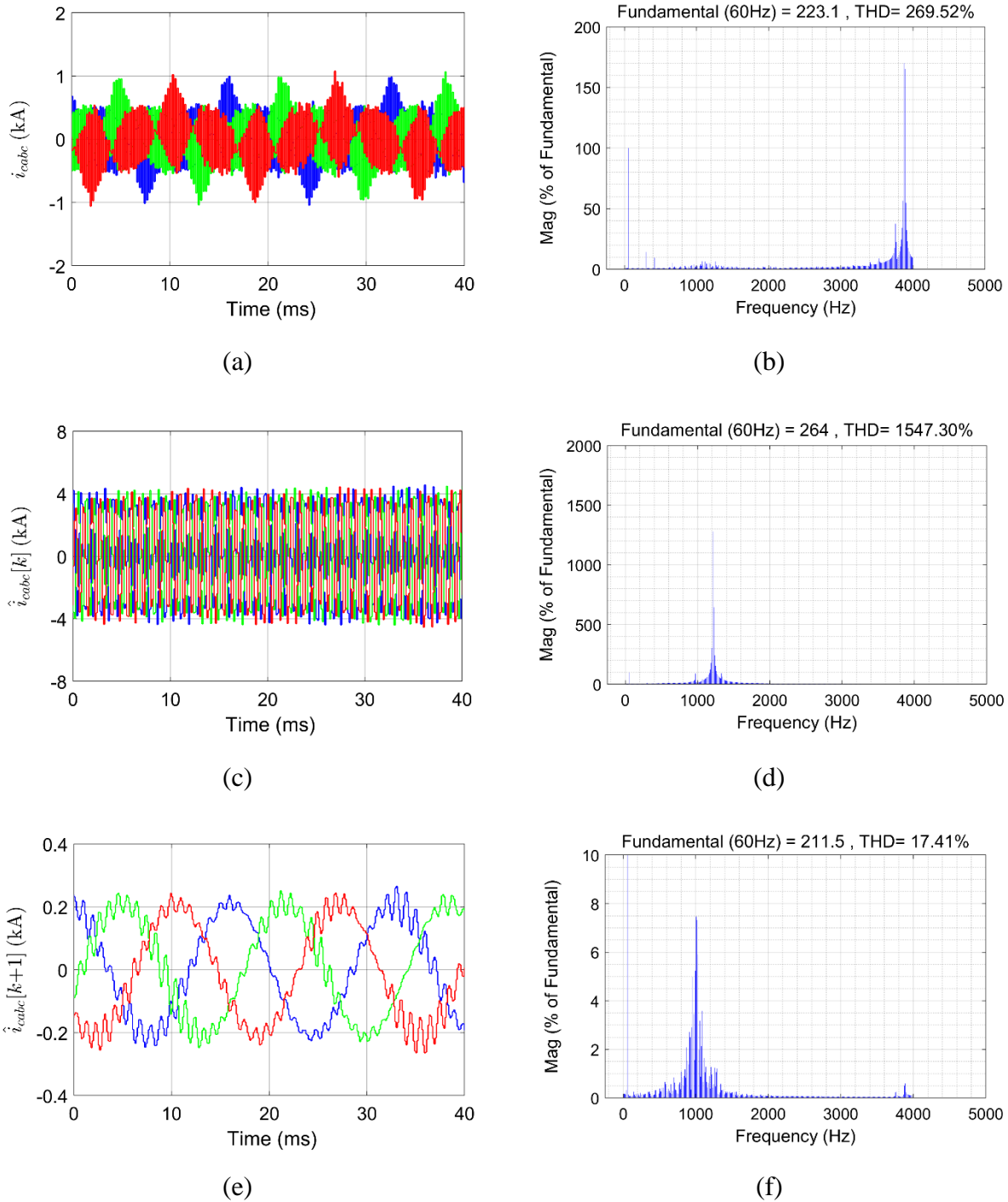


Figure 6.19 Three-phase capacitor currents or estimates for three different types of active damping schemes with an active damping gain of $K_{ad} = 0.0001 \text{ A}^{-1}$ when $f_r < f_{crit}$ with a grid inductance of $60 \mu\text{H}$. Capacitor-current-feedback active damping: (a) measured capacitor currents, (b) current THD. Capacitor-current-estimate-feedback active damping: (c) capacitor-current estimates, (d) current THD. One-sample-ahead capacitor-current-estimate-feedback active damping: (e) one-sample-ahead capacitor-current estimates, (f) current THD.

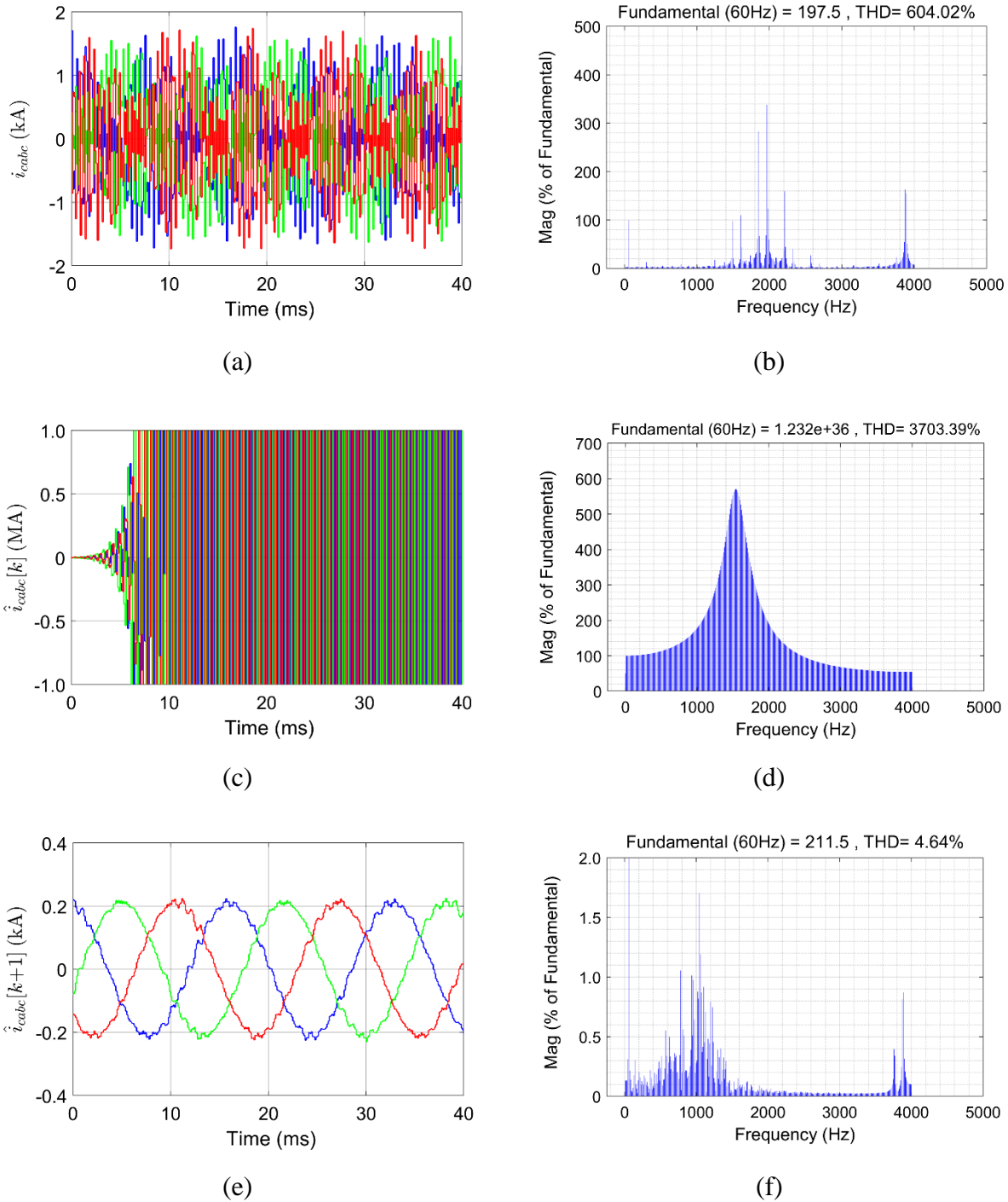


Figure 6.20 Three-phase capacitor currents or estimates for three different types of active damping schemes with an active damping gain of $K_{ad} = 0.0003 \text{ A}^{-1}$ when $f_r < f_{crit}$ with a grid inductance of $60 \mu\text{H}$. Capacitor-current-feedback active damping: (a) measured capacitor currents, (b) current THD. Capacitor-current-estimate-feedback active damping: (c) capacitor-current estimates, (d) current THD. One-sample-ahead capacitor-current-estimate-feedback active damping: (e) one-sample-ahead capacitor-current estimates, (f) current THD.

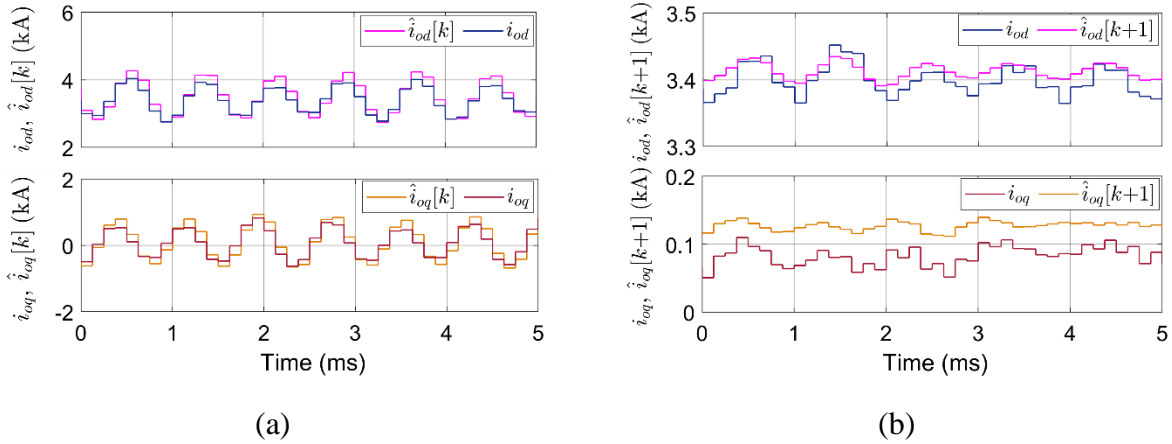
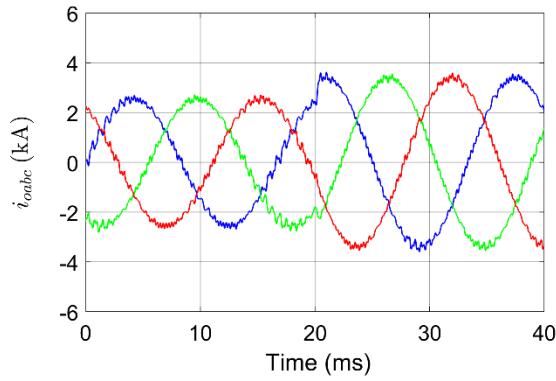
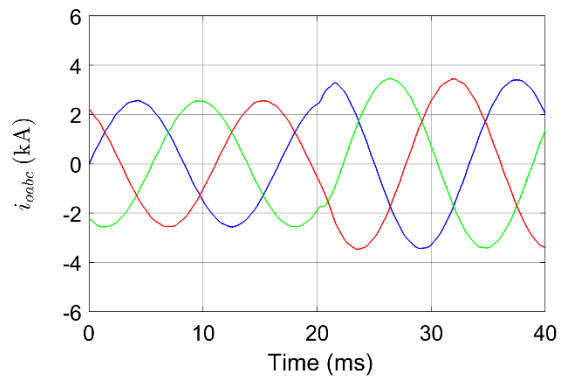


Figure 6.21 Three-phase grid-side currents and their estimates in the dq frame for two different types of active damping schemes with an active damping gain of $K_{ad} = 0.0001 \text{ A}^{-1}$ when $f_r < f_{crit}$ with a grid inductance of $60 \mu\text{H}$. (a) Current-state grid-side-current estimates for the capacitor-current-estimate-feedback active damping system (b) One-sample-ahead grid-side-current estimates of the one-sample-ahead capacitor-current-estimate-feedback active damping system.

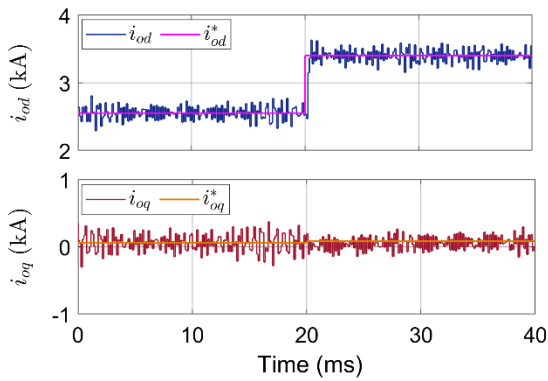
The capacitor-current-feedback active damping system shows incoherent results from the perspective of the frequency response and the root locus analyses. As the active damping gain, K_{ad} , increases within the limits, the THD gradually decreases. It means a very narrow range of the active damping gain ensures the currents of low THD, whereas the one-sample-ahead capacitor-current-estimate active damping system maintains the currents of the lowest THD in a much broad range of the active damping gain, meaning enhanced robustness under system parameter variation. The reconstructed capacitor-current estimates with an increased active damping gain of $K_{ad} = 0.0003 \text{ A}^{-1}$ look appropriate sinusoids with a THD of 4.64 %. In summary, the proposed delay-compensated active damping method provides much more effective damping, known as strong active damping, than two other active damping schemes. It also improves robustness not only against variation of system parameters but under the grid inductance variation.



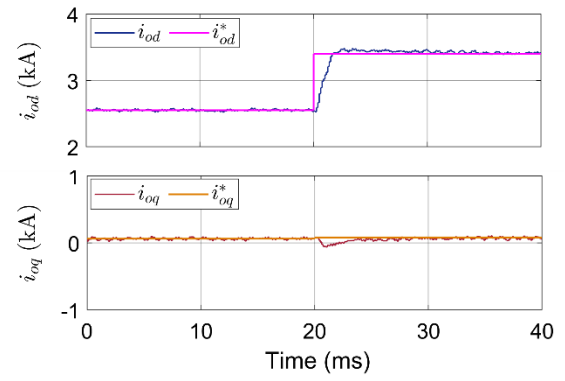
(a)



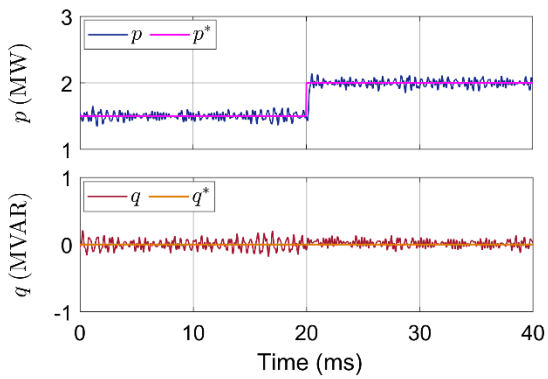
(d)



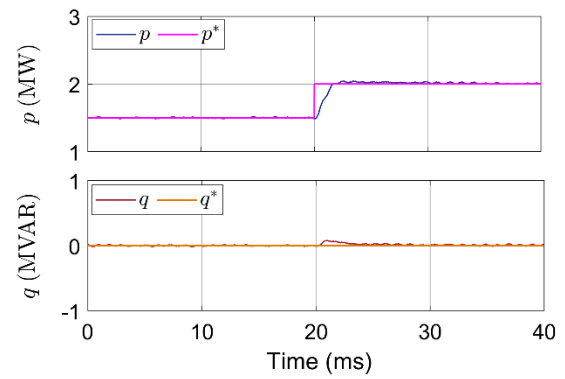
(b)



(e)



(c)



(f)

Figure 6.22 A step change in supply power to the grid for the one-sample-ahead capacitor-current-estimate active damping system when $f_r > f_{crit}$: (a) grid-side currents, (b) grid-side currents in the dq frame, (c) active and reactive powers. When $f_r < f_{crit}$, $L_g = 60 \mu\text{H}$. (d) grid-side currents, (e) grid-side currents in the dq frame, (f) active and reactive powers.

The one-sample-ahead grid-side current estimates in the dq frame properly reflect next instant estimates in comparison with the current-state grid-current estimates in Figure 6.21.

A step change in supply power to the grid is performed and the results in Figure 6.22 show good dynamic performance with satisfactory settling times and a good reference tracking ability for both the cases.

The limits of the active damping gain ensuring stable operation are shown in Table 6.1 for the capacitor-current-feedback active damping system, capacitor-current-estimate-feedback active damping system and the one-sample-ahead capacitor-current-estimate-feedback active damping system.

Table 6.1. The Stable Operation Regions of the Active Damping Gain

	capacitor-current-feedback	Capacitor-current-estimate-feedback	One-sample-ahead capacitor-current-estimate-feedback
When $f_r > f_{crit}$ with zero grid inductance			
K_{ad_min} (A^{-1})	0	0	0
K_{ad_max} (A^{-1})	0.00022	0.00022	0.00046
When $f_r < f_{crit}$ with a grid inductance of $60 \mu H$			
K_{ad_min} (A^{-1})	0.00006	0.00006	0.00003
K_{ad_max} (A^{-1})	0.00017	0.00017	0.00065

Comparison results in terms of current THD for the three types of the active damping methods are summarized in Table 6.1. The results of the two systems employing the a posteriori and a priori Kalman estimators, respectively, are very consistent with the design analyses. Within the stable active damping gain limits, the systems stably operate yielding coherent THDs as

expected from the root loci. When the active damping gains are out of the limits, the systems become unstable, which also agrees well with the analyses. However, the capacitor-current-feedback active damping system has THDs irrelevant to the analyses, meaning unpredictable when it comes to using the capacitor-current as a feedback signal.

Table 6.2. Grid-Side Current THDs for Three Different Types of the Active Damping Methods

$K_{ad} (A^{-1})$	capacitor-current-feedback	Capacitor-current-estimate-feedback	One-sample-ahead capacitor-current-estimate-feedback
When $f_r > f_{crit}$ with zero grid inductance			
0.0001	298.00 %	773.92 %	133.06 %
0.0002	430.30 %	163.18 %	33.07 %
0.0003	255.21 %	unstable	3.67 %
0.0004	unstable	unstable	3.36 %
0.0005	unstable	unstable	unstable
When $f_r < f_{crit}$ with a grid inductance of 60 μH			
0.0001	0.53 %	17.62 %	0.64 %
0.0002	1.15 %	unstable	0.46 %
0.0003	2.39 %	unstable	0.44 %
0.0004	5.85 %	unstable	0.43 %
0.0005	7.04 %	unstable	0.49 %
0.0006	8.93 %	unstable	0.61 %
0.0007	9.53 %	unstable	unstable

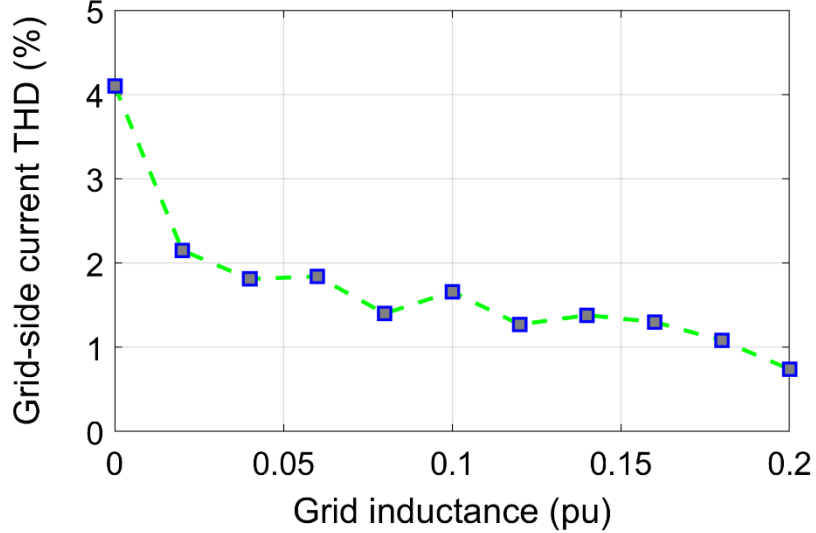


Figure 6.23. Grid-side current THDs of the one-sample-ahead capacitor-current-estimate-feedback active damping system with variation in grid inductance.

Robustness under grid inductance variation from 0 to 0.2 pu is verified in Figure 6.23 for the one-sample-ahead capacitor-current-estimate-feedback system including a fixed grid inductance value of $9 \mu\text{H}$ (0.03 pu) for the a priori Kalman estimator and $K_p = 0.00024 \text{ A}^{-1}$ for the PR controller. In order for the system to be robust under parameter variation or mismatch, large values for the covariance matrix Q of the system measurement vector w are employed. As the grid inductance varies from 0 to 0.2 pu the THDs keep dropping from about THD 4.1 % to below THD 1 %. This indicates that stable operation is ensured by strong active damping application regardless of the location of the resonance peak with variations in grid inductance.

For the system, phase-locked loop (PLL) via point of common coupling might deteriorate the control system. A weak grid has more serious negative effects of PLL on the control system. However, the proposed method improves stability with more increased gain margin and phase margin under a weak grid. Accordingly, the proposed control system can effectively mitigate the negative impacts of PLL on the system.

CHAPTER 7 MODEL PREDICTIVE CONTROL

7.1 Introduction

As use of renewal resources rises, the number of grid-connected inverters increases in power grids. The inverter is accompanied by an inductive-capacitive-inductive (LCL) filter to attenuate the pulse width modulation (PWM) switching harmonics. The filter enables to reduce overall size and weight when compared with a conventional inductive (L) filter [3]–[5]. However, an LCL filter introduces substantial complexity from a control perspective due to a resonance phenomenon caused by the filter elements, which creates a pair of system poles located on the closed-loop stability boundary. Therefore, designing a control system for a grid-connected voltage source inverter (VSI) with an LCL filter is a very challenging task [11], [12]. In particular, a weak grid implying a grid with a low short circuit ratio (SCR) can lead to voltage fluctuation at the inverter terminals and consequently cause inverter instability [11], [38]. The literature [39] demonstrates a decrease in grid inductance does not necessarily improve the stability of grid-connected VSIs. It also claims that system stability is a function of both the grid R/X ratio and grid inductance. Additionally, despite the grid-side inductor of an LCL filter is in series with the grid impedance, they have different effects on the stability of the system [39].

There are many types of model predictive control (MPC) under different names but they all have a similarity, which is to predict future events and take control actions based on objective function minimization [40]–[42]. Since predictive control drew a growing attention almost three decades ago, research and development activities in finite control set MPC (FCS-MPC) have become substantially active for the last decade [42], [43]. As the consequences of the intensive study, advanced analysis techniques and practical tests for FCS-MPC have been performed for a

wide range of power conversion applications [41]. FCS-MPC has many advantages over a classical linear controller, which are nonlinear nature, a modulator-free structure and good dynamic performance [42], [44]. These merits suggest that FCS-MPC could be applied in a wide variety of systems in place of conventional control methods which are quite vulnerable to uncertainties in practice [42], [45]–[47]. Non-linearity of systems in nature puts restrictions on the closed-loop performance because the conventional design methods develop controllers based on a linearized model [42].

For a grid-connected VSI, current control is commonly performed with a linear PI controller in the synchronous reference frame. A controller has been designed based on the fixed resonant frequency of an output LCL filter. However, the filter resonance is also affected by the equivalent grid impedance and is therefore subject to change depending on grid conditions. This further complicates designing a robust PI controller. As another approach for the issue, FCS-MPC with a cost function including active damping is designed and applied to a grid-connected VSI with an LCL filter system. Performance between the PI-based current control and FCS-MPC is compared from an active damping perspective [48].

7.2 Modeling of a Three-Phase Inverter for Model Predictive Control

7.2.1 Modeling of Grid Currents in *abc*-Frame

The primary object for an inverter includes regulation of grid active and reactive power through control of the grid currents. Modeling of the system in continuous time is converted to in discrete time of *abc*, $\alpha\beta$, and *dq* reference frames. In order to relate the grid current dynamics to inverter switching states, the inverter terminal voltages are formulated in terms of switching states. To simplify analysis, the following assumptions are made:

$$\begin{aligned}
 R_{1a} = R_{1b} = R_{1c} = R_t \quad (R_t = R_i + R_g) & \qquad L_{1a} = L_{1b} = L_{1c} = L_t \quad (L_t = L_i + L_g) \\
 v_{ga} + v_{gb} + v_{gc} = 0 & \qquad i_{ga} = i_{gb} = i_{gc} = 0.
 \end{aligned}
 \tag{7.1}$$

In Figure 7.1 L_i and L_g are respectively the inverter-side inductance and the grid-side inductance. Similarly, R_i and R_g are the internal resistances of the inverter-side inductor and the grid-side inductor, respectively. C_f is the capacitance of the filter. V_{dc} , v_i , and v_g are the dc voltage source inverter output voltage, and the grid voltage.

In fact, at frequencies lower than half of the resonance frequency, an LCL-filter frequency characteristic is equivalent to the frequency characteristic of an inductor filter made by the sum of the inductance downstream of the inverter. By Kirchoff's voltage law, the grid-connected inverter system shown in Figure 7.1 is expressed in terms of the grid voltages, the grid currents, and the filter parameters as follows:

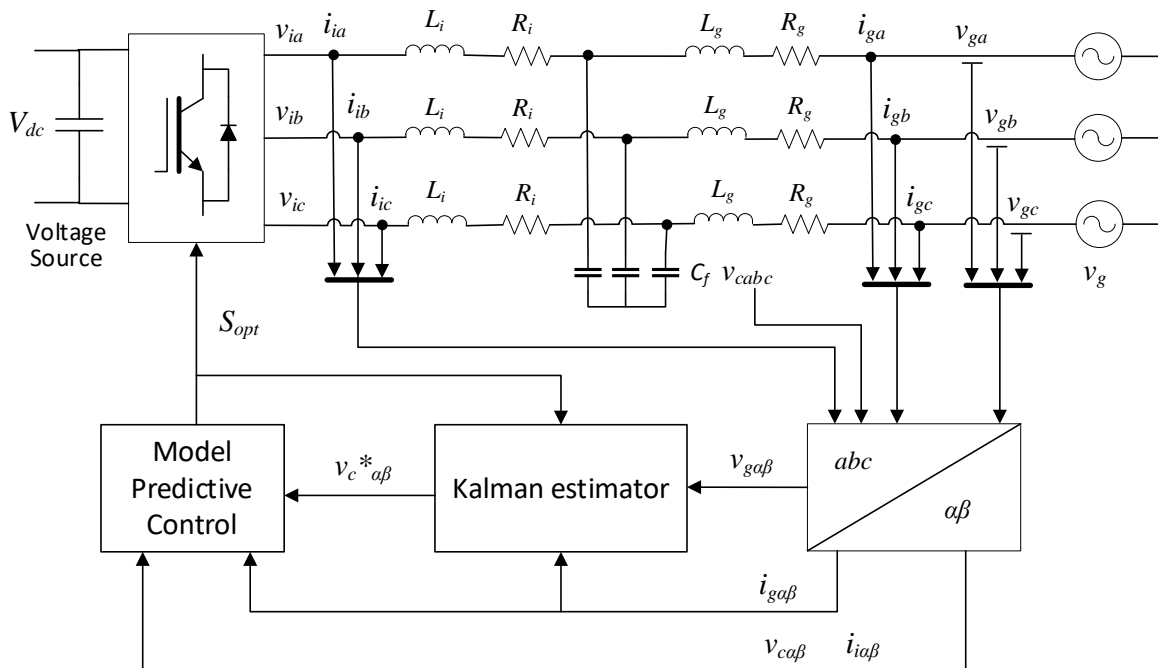


Figure 7.1. Block diagram of a three-phase inverter with a model predictive control system.

$$\begin{bmatrix} v_{Na} \\ v_{Nb} \\ v_{Nc} \end{bmatrix} = \begin{bmatrix} R_t & 0 & 0 \\ 0 & R_t & 0 \\ 0 & 0 & R_t \end{bmatrix} \begin{bmatrix} i_{ga} \\ i_{gb} \\ i_{gc} \end{bmatrix} + \begin{bmatrix} L_t & 0 & 0 \\ 0 & L_t & 0 \\ 0 & 0 & L_t \end{bmatrix} \frac{d}{dt} \begin{bmatrix} i_{ga}(t) \\ i_{gb}(t) \\ i_{gc}(t) \end{bmatrix} + \begin{bmatrix} v_{ga} \\ v_{gb} \\ v_{gc} \end{bmatrix} + \begin{bmatrix} v_{nN} \\ v_{nN} \\ v_{nN} \end{bmatrix}. \quad (7.2)$$

For a three-phase balanced grid, the grid neutral voltage v_{nN} is given as:

$$v_{nN} = \frac{v_{Na} + v_{Nb} + v_{Nc}}{3}. \quad (7.3)$$

By substituting equation (7.3) into equation (7.2), the abc -frame continuous time grid current dynamics are expressed as:

$$\underbrace{\frac{d}{dt} \begin{bmatrix} i_{ga}(t) \\ i_{gb}(t) \\ i_{gc}(t) \end{bmatrix}}_{\dot{x}(t)} = \underbrace{\begin{bmatrix} -\frac{R_t}{L_t} & 0 & 0 \\ 0 & -\frac{R_t}{L_t} & 0 \\ 0 & 0 & -\frac{R_t}{L_t} \end{bmatrix}}_A \underbrace{\begin{bmatrix} i_{ga}(t) \\ i_{gb}(t) \\ i_{gc}(t) \end{bmatrix}}_{x(t)} + \underbrace{\begin{bmatrix} \frac{1}{L_t} & 0 & 0 \\ 0 & \frac{1}{L_t} & 0 \\ 0 & 0 & \frac{1}{L_t} \end{bmatrix}}_{B_i} \underbrace{\begin{bmatrix} v_{na}(t) \\ v_{nb}(t) \\ v_{nc}(t) \end{bmatrix}}_{v_i(t)} + \underbrace{\begin{bmatrix} -\frac{1}{L_t} & 0 & 0 \\ 0 & -\frac{1}{L_t} & 0 \\ 0 & 0 & -\frac{1}{L_t} \end{bmatrix}}_{B_g} \underbrace{\begin{bmatrix} v_{ga}(t) \\ v_{gb}(t) \\ v_{gc}(t) \end{bmatrix}}_{v_g(t)}. \quad (7.4)$$

MPC is basically an optimization algorithm implemented on digital control platforms.

Therefore, continuous time models should be converted to discrete time equivalents. By using the forward Euler approximation the discrete time grid current model is obtained in the abc -frame [41]:

$$\begin{bmatrix} i_{ga}(k+1) \\ i_{gb}(k+1) \\ i_{gc}(k+1) \end{bmatrix} = \Phi \begin{bmatrix} i_{ga}(k) \\ i_{gb}(k) \\ i_{gc}(k) \end{bmatrix} + \Gamma_i \begin{bmatrix} v_{na}(k) \\ v_{nb}(k) \\ v_{nc}(k) \end{bmatrix} + \Gamma_g \begin{bmatrix} v_{ga}(k) \\ v_{gb}(k) \\ v_{gc}(k) \end{bmatrix}, \quad (7.5)$$

where the discrete time equivalent matrices are defined by

$$\Phi \approx [I + AT_s] \approx \begin{bmatrix} 1 - \frac{R_t T_s}{L_t} & 0 & 0 \\ 0 & 1 - \frac{R_t T_s}{L_t} & 0 \\ 0 & 0 & 1 - \frac{R_t T_s}{L_t} \end{bmatrix}, \Gamma_i \approx B_i T_s \approx \begin{bmatrix} \frac{T_s}{L_t} & 0 & 0 \\ 0 & \frac{T_s}{L_t} & 0 \\ 0 & 0 & \frac{T_s}{L_t} \end{bmatrix}, \Gamma_g \approx B_g T_s \approx \begin{bmatrix} -\frac{T_s}{L_t} & 0 & 0 \\ 0 & -\frac{T_s}{L_t} & 0 \\ 0 & 0 & -\frac{T_s}{L_t} \end{bmatrix}. \quad (7.6)$$

7.2.2 Modeling of Grid Currents in $\alpha\beta$ -Frame

By using the abc to $\alpha\beta$ transformation matrix, the $\alpha\beta$ -frame grid current continuous model is derived as follows:

$$\underbrace{\frac{d}{dt} \begin{bmatrix} i_{g\alpha}(t) \\ i_{g\beta}(t) \end{bmatrix}}_{\dot{\mathbf{x}}(t)} = \underbrace{\begin{bmatrix} -\frac{R_t}{L_t} & 0 \\ 0 & -\frac{R_t}{L_t} \end{bmatrix}}_{\mathbf{A}} \underbrace{\begin{bmatrix} i_{g\alpha}(t) \\ i_{g\beta}(t) \end{bmatrix}}_{\mathbf{x}(t)} + \underbrace{\begin{bmatrix} \frac{1}{L_t} & 0 \\ 0 & \frac{1}{L_t} \end{bmatrix}}_{\mathbf{B}_i} \underbrace{\begin{bmatrix} v_{i\alpha}(t) \\ v_{i\beta}(t) \end{bmatrix}}_{\mathbf{v}_i(t)} + \underbrace{\begin{bmatrix} -\frac{1}{L_t} & 0 \\ 0 & -\frac{1}{L_t} \end{bmatrix}}_{\mathbf{B}_g} \underbrace{\begin{bmatrix} v_{g\alpha}(t) \\ v_{g\beta}(t) \end{bmatrix}}_{\mathbf{v}_g(t)}. \quad (7.7)$$

By using the forward Euler approximation into equation (7.7), the discrete time current model is given as follows:

$$\begin{bmatrix} i_{g\alpha}(k+1) \\ i_{g\beta}(k+1) \end{bmatrix} = \Phi \begin{bmatrix} i_{g\alpha}(k) \\ i_{g\beta}(k) \end{bmatrix} + \Gamma_i \begin{bmatrix} v_{i\alpha}(k) \\ v_{i\beta}(k) \end{bmatrix} + \Gamma_g \begin{bmatrix} v_{g\alpha}(k) \\ v_{g\beta}(k) \end{bmatrix}. \quad (7.8)$$

The approximate discrete time equivalent matrices are obtained as

$$\Phi \approx [\mathbf{I} + \mathbf{A}T_s] \approx \begin{bmatrix} 1 - \frac{R_t T_s}{L_t} & 0 \\ 0 & 1 - \frac{R_t T_s}{L_t} \end{bmatrix}, \Gamma_i \approx \mathbf{B}_i T_s \approx \begin{bmatrix} \frac{T_s}{L_t} & 0 \\ 0 & \frac{T_s}{L_t} \end{bmatrix}, \Gamma_g \approx \mathbf{B}_g T_s \approx \begin{bmatrix} -\frac{T_s}{L_t} & 0 \\ 0 & -\frac{T_s}{L_t} \end{bmatrix}. \quad (7.9)$$

7.2.3 Modeling of Grid Currents in dq -Frame

In the synchronous frame subscripts d and q correspond to the orthogonal synchronous frame-axes. One significant aspect of dq -frame is that all the variables are dc in nature. The dq -frame model has $-\omega_g L_t i_{gq}$ and $\omega_g L_t i_{gd}$ representing the induced speed voltages caused by the transformation of variables from the abc -frame to dq -frame [43]. By the abc - to dq -frame transformation matrix the grid current model in dq -frame is given in equation (7.10), that is,

$$\underbrace{\frac{d}{dt} \begin{bmatrix} i_{gd}(t) \\ i_{gq}(t) \end{bmatrix}}_{\dot{x}(t)} = \underbrace{\begin{bmatrix} -\frac{R_t}{L_t} & \omega_g \\ -\omega_g & -\frac{R_t}{L_t} \end{bmatrix}}_A \underbrace{\begin{bmatrix} i_{gd}(t) \\ i_{gq}(t) \end{bmatrix}}_{x(t)} + \underbrace{\begin{bmatrix} \frac{1}{L_t} & 0 \\ 0 & \frac{1}{L_t} \end{bmatrix}}_{B_i} \underbrace{\begin{bmatrix} v_{id}(t) \\ v_{iq}(t) \end{bmatrix}}_{v_i(t)} + \underbrace{\begin{bmatrix} -\frac{1}{L_t} & 0 \\ 0 & -\frac{1}{L_t} \end{bmatrix}}_{B_g} \underbrace{\begin{bmatrix} v_{gd}(t) \\ v_{gq}(t) \end{bmatrix}}_{v_g(t)}. \quad (7.10)$$

By the forward Euler approximation, the discrete time current model is obtained as below:

$$\begin{bmatrix} i_{gd}(k+1) \\ i_{gq}(k+1) \end{bmatrix} = \Phi \begin{bmatrix} i_{gd}(k) \\ i_{gq}(k) \end{bmatrix} + \Gamma_i \begin{bmatrix} v_{id}(k) \\ v_{iq}(k) \end{bmatrix} + \Gamma_g \begin{bmatrix} v_{gd}(k) \\ v_{gq}(k) \end{bmatrix}. \quad (7.11)$$

The approximate discrete time equivalent matrices are obtained as

$$\Phi \approx [I + AT_s] \approx \begin{bmatrix} 1 - \frac{R_t T_s}{L_t} & \omega_g T_s \\ -\omega_g T_s & 1 - \frac{R_t T_s}{L_t} \end{bmatrix}, \Gamma_i \approx B_i T_s \approx \begin{bmatrix} \frac{T_s}{L_t} & 0 \\ 0 & \frac{T_s}{L_t} \end{bmatrix}, \Gamma_g \approx B_g T_s \approx \begin{bmatrix} -\frac{T_s}{L_t} & 0 \\ 0 & -\frac{T_s}{L_t} \end{bmatrix}. \quad (7.12)$$

7.3 Cost Function

The models in equations (7.5), (7.8), and (7.11) indicate that the future currents are obtained on the basis of selection of the inverter voltages. Through the model of a 2-level VSI, switching states are founded in association with the voltages. Due to the finite number of switching state combinations, eight for a 2-level VSI, the iterations are relatively simplified. The eight possible combinations indicate eight different predictions for the output grid currents. The errors between the eight predictive currents and the extrapolated reference currents are evaluated by an absolute cost function of $g(k)$:

$$g(k) = |\hat{i}^*(k+1) - i^p(k+1)|. \quad (7.13)$$

The minimum cost function value is identified by comparison and the corresponding switching state combination is applied to the inverter. To provide active damping for resonance caused by the inverter output LCL filter, a frequency-dependent cost function can be used [105].

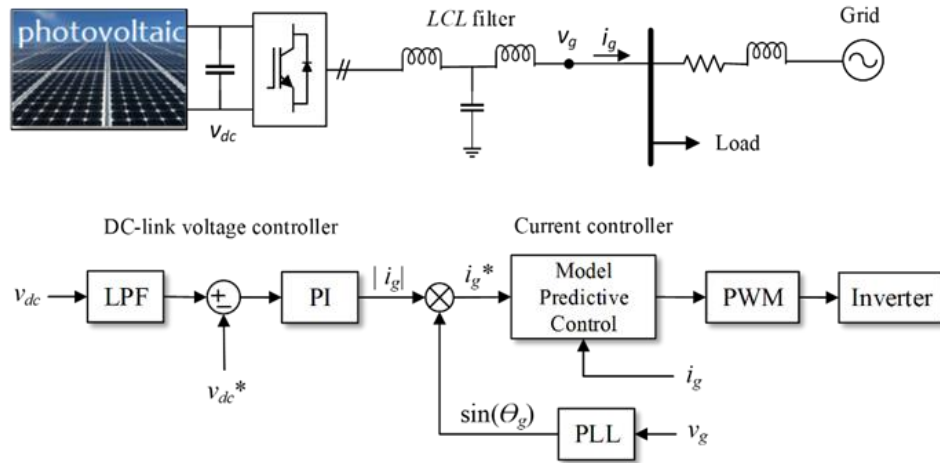


Figure 7.2. Model predictive control application to a grid-connected inverter.

7.4 MPC Discrete Model With an Embedded Integrator

A grid-connected three-phase inverter regulated by a model predictive current control algorithm is simulated in Matlab/Simulink[®]. Finite control set model predictive control consists of three main parts, which are extrapolation of reference currents, prediction of state variables in discrete-time model, and cost function minimization. The finite number of switching state combinations is evaluated in terms of error between predictive currents and extrapolated reference currents by using the absolute cost function. A switching state corresponding to a minimum cost function value is applied to the inverter switches. In addition, a feedforward term is generally introduced to take grid harmonics into account, which reduces the THD of grid-side currents. This requires that the measured grid voltages scaled by a factor of $2/V_{dc}$ in the $\alpha\beta$ frame are added to the switching input signals that are obtained from the cost function minimization. Finally, the duty cycles are applied to the inverter switches via the $\alpha\beta$ to abc transformation.

Figure 7.2 shows a three-phase grid-connected VSI with an LCL filter, where the reference currents are generated from the dc-link control system and the measured PCC voltages. The VSI with the LCL filter system shown in 7.1 is expressed in the $\alpha\beta$ frame as follows:

$$\begin{aligned}
\dot{x}(t) &= Ax(t) + B_i u(t) + B_g v_g(t) \\
y &= Cx(t)
\end{aligned}$$

$$A = \begin{bmatrix} -\frac{R_i}{L_i} & 0 & -\frac{1}{L_i} & 0 & 0 & 0 \\ 0 & -\frac{R_i}{L_i} & 0 & -\frac{1}{L_i} & 0 & 0 \\ \frac{1}{C_f} & 0 & 0 & 0 & -\frac{1}{C_f} & 0 \\ 0 & \frac{1}{C_f} & 0 & 0 & 0 & -\frac{1}{C_f} \\ 0 & 0 & \frac{1}{L_g} & 0 & -\frac{R_g}{L_g} & 0 \\ 0 & 0 & 0 & \frac{1}{L_g} & 0 & -\frac{R_g}{L_g} \end{bmatrix} \tag{7.14}$$

$$B_i = \begin{bmatrix} 0 & \frac{v_{dc}}{2L_i} & 0 & 0 & 0 & 0 \\ \frac{v_{dc}}{2L_i} & 0 & 0 & 0 & 0 & 0 \end{bmatrix}^T K_{\alpha\beta}$$

$$B_g = \begin{bmatrix} 0 & 0 & 0 & 0 & 0 & \frac{1}{-L_g} \\ 0 & 0 & 0 & 0 & \frac{1}{-L_g} & 0 \end{bmatrix}^T K_{\alpha\beta}$$

$$C = [0 \quad 0 \quad 0 \quad 0 \quad 1 \quad 1]$$

$$K_{\alpha\beta} = \frac{2}{3} \begin{bmatrix} 1 & -\frac{1}{2} & -\frac{1}{2} \\ 0 & \frac{\sqrt{3}}{2} & -\frac{\sqrt{3}}{2} \end{bmatrix},$$

where $x(t) = [i_{i\alpha} \quad i_{i\beta} \quad v_{cf\alpha} \quad v_{cf\beta} \quad i_{g\alpha} \quad i_{g\beta}]^T$, and $v_g(t)$ is the grid voltage vector. The model is required to be discretized with a sampling period T_s by using the forward Euler approximation. The discrete state-space model is represented as follows:

$$\begin{aligned}
x_d(k+1) &= A_d x_d(k) + B_{id} u(k) + B_{gd} v_g(k) \\
y_d(k) &= C_d x_d(k).
\end{aligned} \tag{7.15}$$

In order to ensure a zero steady-state error, an integrator is embedded in the state-space model.

Taking a difference operation on both sides of equation (7.15) yields

$$\begin{aligned} x_d(k+1) - x_d(k) &= A_d(x_d(k) - x_d(k-1)) + B_{id}(u(k) - u(k-1)) \\ &\quad + B_{gd}(v_g(k) - v_g(k-1)). \end{aligned} \quad (7.16)$$

The difference of the state variable is denoted by

$$\Delta x_d(k+1) = A_d \Delta x_d(k) + B_{id} \Delta u(k). \quad (7.17)$$

Note that the last term of equation (7.16) is regarded as an input disturbance and is removed since it is assumed to be a slowly varying disturbance, i.e., $v_g(k) = v_g(k-1)$. The output variable is determined in its incremental dynamics as

$$\begin{aligned} y_d(k+1) - y_d(k) &= C_d(x_d(k+1) - x_d(k)) \\ &= C_d A_d \Delta x_d(k) + C_d B_{id} \Delta u(k). \end{aligned} \quad (7.18)$$

Now, a new state variable vector is chosen to be

$$x(k) = [\Delta x_d(k) \quad y_d(k)]^T \quad (7.19)$$

Putting together equations (7.17) and (7.18) leads to the following augmented state-space model:

$$\begin{aligned} x(k+1) &= \mathbf{A}x(k) + \mathbf{B}\Delta u(k) \\ y(k) &= \mathbf{C}x(k). \end{aligned} \quad (7.20)$$

$$\mathbf{A} = \begin{bmatrix} A_d & \mathbf{0}_6^T \\ C_d A_d & 1 \end{bmatrix}, \mathbf{B} = \begin{bmatrix} B_{id} \\ C_d B_{id} \end{bmatrix}, \mathbf{C} = [\mathbf{0}_6 \quad 1],$$

where $\mathbf{0}_6 = [0 \ 0 \ 0 \ 0 \ 0 \ 0]$. This model ensures a zero steady-state error.

7.5 Prediction of State and Output Variables Within a Prediction Horizon

Assuming that at the sampling instant k_i , the state variable vector $x(k_i)$ is obtained through measurement. The vector of future incremental control actions are expressed as follows:

$$\Delta u = [\Delta u(k_i) \quad \Delta u(k_i + 1) \quad \dots \quad \Delta u(k_i + N_c - 1)], \quad (7.21)$$

where N_c is called the control horizon stating the number of parameters used to capture the future control trajectory. Given information $x(k_i)$, the future state variables are predicted for N_p number of samples, where N_p is the prediction horizon and also the length of the optimization window.

The future state variables are expressed as

$$x(k_i + 1|k_i), x(k_i + 2|k_i), \dots, x(k_i + m|k_i), \dots, x(k_i + N_p|k_i), \quad (7.22)$$

where $x(k_i + m|k_i)$ is the predicted state variable at $k_i + m$ with given information $x(k_i)$. The control horizon N_c is selected to be less than or equal to the prediction horizon N_p . Then, the future state variables are computed sequentially using the set of future control parameters:

$$\begin{aligned} x(k_i + 1|k_i) &= \mathbf{A}x(k_i) + \mathbf{B}\Delta u(k_i) \\ x(k_i + 2|k_i) &= \mathbf{A}^2x(k_i) + \mathbf{A}\mathbf{B}\Delta u(k_i) + \mathbf{B}\Delta u(k_i + 1) \\ &\vdots \\ x(k_i + N_p|k_i) &= \mathbf{A}^{N_p}x(k_i) + \mathbf{A}^{N_p-1}\mathbf{B}\Delta u(k_i) + \mathbf{A}^{N_p-2}\mathbf{B}\Delta u(k_i + 1) + \dots \\ &\quad + \mathbf{A}^{N_p-N_c}\mathbf{B}\Delta u(k_i + N_c - 1). \end{aligned} \quad (7.23)$$

From the predicted state variables, the predicted output variables are obtained by substitution:

$$\begin{aligned} y(k_i + 1|k_i) &= \mathbf{C}\mathbf{A}x(k_i) + \mathbf{C}\mathbf{B}\Delta u(k_i) \\ y(k_i + 2|k_i) &= \mathbf{C}\mathbf{A}^2x(k_i) + \mathbf{C}\mathbf{A}\mathbf{B}\Delta u(k_i) + \mathbf{C}\mathbf{B}\Delta u(k_i + 1) \\ &\vdots \\ y(k_i + N_p|k_i) &= \mathbf{C}\mathbf{A}^{N_p}x(k_i) + \mathbf{C}\mathbf{A}^{N_p-1}\mathbf{B}\Delta u(k_i) + \mathbf{C}\mathbf{A}^{N_p-2}\mathbf{B}\Delta u(k_i + 1) + \dots \\ &\quad + \mathbf{C}\mathbf{A}^{N_p-N_c}\mathbf{B}\Delta u(k_i + N_c - 1). \end{aligned} \quad (7.24)$$

The output vector is defined as

$$\mathbf{y} = [y(k_i + 1|k_i) \ y(k_i + 2|k_i) \ y(k_i + 3|k_i) \ \dots \ y(k_i + N_p|k_i)]^T \quad (7.25)$$

Finally, equations (7.24) and (7.25) are rewritten in a matrix form as

$$\mathbf{y} = \mathbf{P}x(k_i) + \mathbf{H}\Delta u, \quad (7.26)$$

where \mathbf{y} is a vector of dimension N_p and the dimension of Δu is N_c . The matrices \mathbf{P} and \mathbf{H} are given by

$$\mathbf{P} = \begin{bmatrix} \mathbf{CA} \\ \mathbf{CA}^2 \\ \mathbf{CA}^3 \\ \vdots \\ \mathbf{CA}^{N_p} \end{bmatrix}, \mathbf{H} = \begin{bmatrix} \mathbf{CB} & 0 & 0 & \dots & 0 \\ \mathbf{CAB} & \mathbf{CB} & 0 & \dots & 0 \\ \mathbf{CA}^2\mathbf{B} & \mathbf{CAB} & \mathbf{CB} & \dots & 0 \\ \vdots & \vdots & \vdots & \vdots & \vdots \\ \mathbf{CA}^{N_p-1}\mathbf{B} & \mathbf{CA}^{N_p-2}\mathbf{B} & \dots & \dots & \mathbf{CA}^{N_p-N_c}\mathbf{B} \end{bmatrix}. \quad (7.27)$$

7.6 Cost Function Minimization

For a given set-point signal $ri^*(k_i)$ at sampling time k_i , within a prediction horizon the main objective of an MPC system is to make the predicted output as close as possible to the set-point signal. This is accompanied by an assumption that the reference signal remains constant in the optimization window. The following reference current vector is defined:

$$\mathbf{i}^* = [1 \ 1 \ \dots \ 1]^T i^*(k_i) = ri^*(k_i), \quad (7.28)$$

where $i^*(k_i)$ is the reference current at the sampling instant k_i and \mathbf{r} is a column vector of ones with the prediction horizon N_p .

The following cost function is defined to reflect the control objective as

$$J = (\mathbf{i}^* - \mathbf{y})^T (\mathbf{i}^* - \mathbf{y}) + \Delta \mathbf{u}^T \mathbf{R} \Delta \mathbf{u}, \quad (7.29)$$

where $\mathbf{R} = r_w \mathbf{I}_{N_c \times N_c}$ ($r_w \geq 0$) is a diagonal matrix in which r_w is used as a tuning parameter for the desired closed-loop performance. When $r_w = 0$, the control objective is solely to make the error $(\mathbf{i}^* - \mathbf{y})^T (\mathbf{i}^* - \mathbf{y})$ as small as possible. For the case of large r_w , the cost function primarily considers how large the $\Delta \mathbf{u}$ might be and cautiously reduces the error. In order to find the optimal $\Delta \mathbf{u}$ that minimizes J , equation (7.26) is substituted in equation (7.29), yielding:

$$J = (\mathbf{i}^* - \mathbf{P}\mathbf{x}(k_i))^T (\mathbf{i}^* - \mathbf{P}\mathbf{x}(k_i)) - 2\Delta \mathbf{u}^T \mathbf{H}^T (\mathbf{i}^* - \mathbf{P}\mathbf{x}(k_i)) + \Delta \mathbf{u}^T (\mathbf{H}^T \mathbf{H} + \mathbf{R}) \Delta \mathbf{u}. \quad (7.30)$$

From the first derivative of the cost function with respect to $\Delta \mathbf{u}$:

$$\frac{\partial J}{\partial \Delta u} = -2\mathbf{H}^T(i^* - \mathbf{P}x(k_i)) + 2(\mathbf{H}^T\mathbf{H} + \mathbf{R})\Delta u. \quad (7.31)$$

The necessary condition of the minimum J is obtained by equalizing equation (7.31) to zero and taking into account equation (7.28), giving the incremental control signals as

$$\Delta u(k_i) = (\mathbf{H}^T\mathbf{H} + \mathbf{R})^{-1}\mathbf{H}^T(ri^*(k_i) - \mathbf{P}x(k_i)). \quad (7.32)$$

Note that the vector Δu contains all the incremental control signals from the sampling instant k_i to $k_i + N_c - 1$. Since a receding horizon control is used, only the first control signal is applied.

The actual incremental control signal is expressed as follows:

$$\Delta u(k_i) = w(\mathbf{H}^T\mathbf{H} + \mathbf{R})^{-1}\mathbf{H}^T(ri^*(k_i) - \mathbf{P}x(k_i)), \quad (7.33)$$

where $w = [1 \ 0 \ 0 \ \dots \ 0]$ of which dimension is N_c .

Finally, the optimal control signal is obtained to add the incremental value to the control signal value in the previous sampling instant:

$$u(k_i) = \Delta u(k_i) + u(k_i - 1). \quad (7.34)$$

7.7 Closed-loop Control System

It is found that at a given k_i , the optimal control vector Δu can be separated into two parts as follows:

$$\Delta u(k_i) = K_r i^*(k_i) - K_c x(k_i), \quad (7.35)$$

where

$$\begin{aligned} K_r &= w(\mathbf{H}^T\mathbf{H} + \mathbf{R})^{-1}\mathbf{H}^T\mathbf{r} \\ K_c &= w(\mathbf{H}^T\mathbf{H} + \mathbf{R})^{-1}\mathbf{H}^T\mathbf{P}. \end{aligned} \quad (7.36)$$

Equation (7.35) is in a standard form of linear time-invariant state feedback control, and \mathbf{K}_c is a state feedback gain vector. Therefore, the closed-loop system is obtained by substituting equation (7.35) into the augmented system equation:

$$\mathbf{x}(k+1) = \mathbf{A}\mathbf{x}(k) - \mathbf{B}\mathbf{K}_c\mathbf{x}(k) + K_r\mathbf{B}\mathbf{i}^*(k), \quad (7.37)$$

or equivalently

$$\mathbf{x}(k+1) = (\mathbf{A} - \mathbf{B}\mathbf{K}_c)\mathbf{x}(k) + K_r\mathbf{B}\mathbf{i}^*(k), \quad (7.38)$$

where the closed-loop eigenvalues can be evaluated through the closed-loop characteristic equation:

$$|\lambda\mathbf{I} - \mathbf{A} + \mathbf{B}\mathbf{K}_c| = 0. \quad (7.39)$$

By selecting an appropriate r_w , desired dynamic performance of the MPC system can be achieved [106].

An Euclidean distance between the filter capacitor voltage vector reference and the measured voltage vector is added to the cost function, expressed as

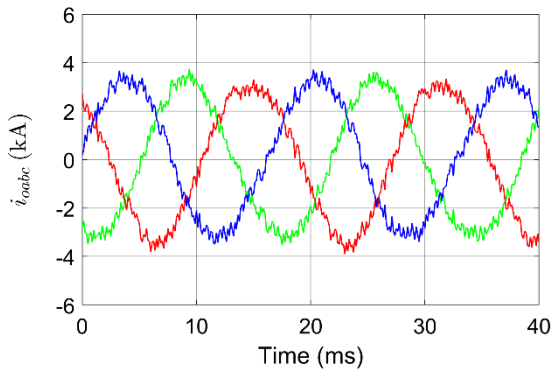
$$g_{con} = |v_{cf\alpha}^*(k+1) - v_{cf\alpha}(k+1)| + |v_{cf\beta}^*(k+1) - v_{cf\beta}(k+1)|. \quad (7.40)$$

For the purpose of incorporating active damping into the MPC system, a term which tracks the derivative of the capacitor voltage vector reference can be added to the cost function and is expressed as [107],

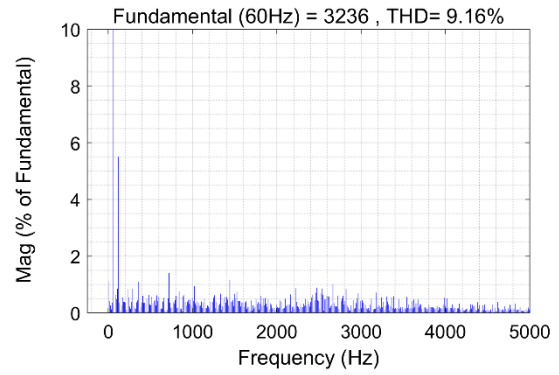
$$g_{der} = |C_f\omega_n v_{cf\beta}^*(k+1) - i_{i\alpha}(k+1) + i_{g\alpha}(k+1)| \\ + |C_f\omega_n v_{cf\alpha}^*(k+1) + i_{i\beta}(k+1) - i_{g\beta}(k+1)|, \quad (7.41)$$

where ω_n is the nominal angular grid frequency and v_{cf} is the voltage of the capacitor. The term has an active damping effect and ensures robust performance in steady-state and dynamic responses. This also allows for easy compensation of nonlinear effects.

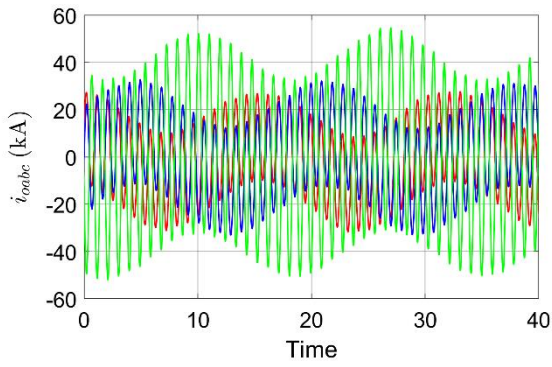
Simulation studies of MPC for the LCL-filtered VSI system are performed using Matlab/Simulink. Three cases are considered and the results are shown in Figure 7.3, which are a system with only total inductance considered, MPC either with active damping or without active damping for the LCL-filtered system. A grid inductance of $60 \mu\text{H}$ is accounted for, indicating the resonance frequency f_r is lower than the critical frequency f_{crit} . Figure 7.3(a) shows that for the inductance-based filter system the MPC generates the output currents with a relatively high THD of 9.16 %. The same system but with the LCL filter is operated by the MPC without active damping term in the cost function. The result in Figure 7.3(b) expresses that severe resonant currents occur due to the LCL filter. It is clear that active damping should be applied in order to attenuate the resonance. Therefore, the cost function containing the active damping effect terms which track the filter capacitor voltage vector and its derivative is adopted for the MPC. Tuning of the cost function can be performed through weighting factors which penalize each term included in the cost function. The applied active damping slightly mitigates the resonance effect caused by the LCL filter, but the system is still severely affected by the resonance as shown in Figure 7.3(c). Thus, the MPC is required to have a more effective and robust active damping scheme for the grid-connected VSI with the LCL filter. Consequently, a finite control set model predictive control strategy is applicable for a grid-connected VSI with an LCL filter, but it needs to significantly improve active damping effect. In addition, robustness against grid impedance variation should be ensured for practical application. Nonetheless, an advanced control strategy, especially MPC, is expected as a potential approach to robust control against complexity and instability caused by resonant phenomena of a grid-connected VSI with an LCL filter. This is due to the fact that high dynamic performance can be achieved with the flexibility of a cost



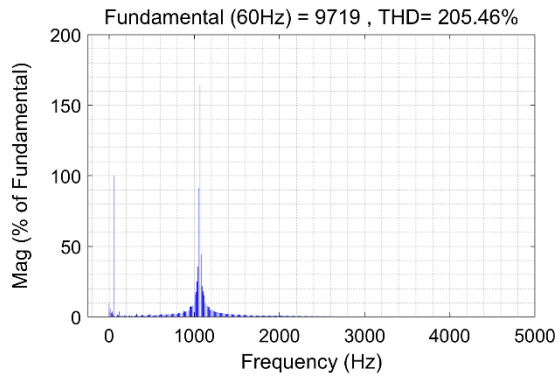
(a)



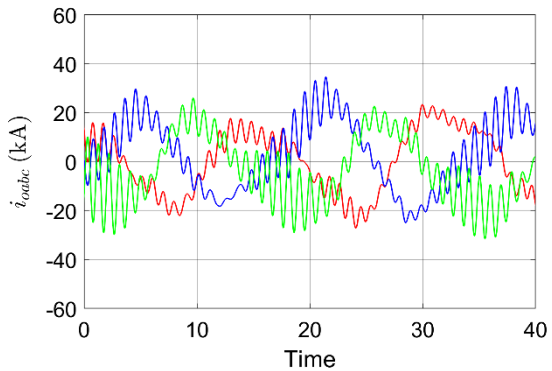
(b)



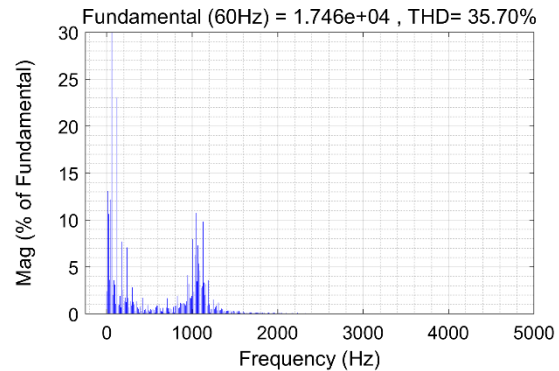
(c)



(d)



(e)



(f)

Figure 7.3 FCS-MPC for the VSI when $f_r < f_{crit}$, $L_g = 60 \mu\text{H}$. (a) With the L filter. (b) Current THD. (c) With the LCL filter without active damping. (d) Current THD. (e) With the LCL filter with active damping. (f) Current THD.

function in MPC design. Thus, MPC is particularly expected to allow for easy compensation for the complicated LCL filter resonance issues attributed to variations in grid condition.

CHAPTER 8 CONCLUSION

Active damping using capacitor current feedback is widely used to suppress the resonance of a grid-connected voltage source inverter (VSI) accompanied by an inductive-capacitive-inductive (LCL) filter. However, control system design analyses and the system performance do not match, which does not lead to a clear consensus on the control system design method. The proposed capacitor-current-estimate active damping employing the designed a posteriori Kalman estimator yields simulation results which is consistent with the design analyses. This outcome reveals that the capacitor current including inverter switching noise components causes the performance results quite different from the design analyses. Therefore, any active damping schemes relying on the capacitor current feedback should take this into account in control system design.

This study addresses a theoretical discrete time analysis framework that identifies three distinct regions of LCL filter resonance, that is, high, critical, and low resonance frequencies. Apparently one-sixth of the sampling frequency $f_s/6$ is regarded as the critical LCL-filter resonance frequency. The high resonance frequency range is where active damping is not needed since the system is inherently stable, meanwhile it is technically necessary to attenuate resonance-induced noise. The low resonance frequency range is where requires active damping. In practice, grid impedance tends to vary with no information. Therefore, the resonance peak also varies and locates at any frequency of the three regions. Therefore the active damping applied to the control should be reinvestigated in order to improve robustness against grid impedance variation.

In order to ensure system stability, active damping should be always enabled because of the grid impedance variation. However, capacitor-current-feedback active damping brings about instability when the displaced resonance peak is in the high frequency range. It has been proved that the capacitor-current-proportional feedback is equivalent to virtual impedance connected in parallel with the filter capacitor. In a digitally controlled system, delays cause the equivalent resistance of the virtual impedance to become negative in the high frequency range, producing a pair of open-loop unstable poles in RHP. The developed a priori Kalman estimator generates one-sample-ahead state variable estimates, which reconstruct the capacitor current estimates for active damping. The one-sample-ahead capacitor-current estimates cancel out the computation delay and ensure system stability regardless of the location of the resonance frequency. The proposed active damping method provides extended boundaries of active damping gains, which enhances robustness against system parameter variation. It also allows strong active damping that results in more attenuation for resonance noise reduction.

An essence of adopting the developed Kalman estimators into a system is their role as a system stability identifier, let alone their primary functions of filtering and estimation. Usually, it is difficult to figure out if a system severely suffers from resonance noise or is in an unstable condition. The state variables of Kalman estimators go to infinity when the system is unstable, which offers a clear and easy way to analyze system stability.

As an alternative, model predictive control (MPC) has been designed and implemented for a grid-connected VSI with an LCL filter. The MPC can incorporate active damping effect terms into a cost function and tune the overall cost function through weighting factors. This study suggests that MPC can be a promising control scheme for a grid-connected VSI with good dynamic performance.

REFERENCES

- [1] C.-Y. Tang, Y.-F. Chen, Y.-M. Chen and Y.-R. Chang, "DC-link voltage control strategy for three-phase back-to-back active power conditioners", *IEEE Trans. Ind. Electron.*, vol. 62, no. 10, pp. 6306–6316, Oct. 2015.
- [2] A. Rodriguez-Cabero, M. Prodanovic and J. Roldan-Perez, "Full-state feedback control of back-to-back converters based on differential and common power concepts", *IEEE Trans. Ind. Electron.*, vol. 66, no. 11, pp. 9045–9055, Nov. 2019.
- [3] Y. Tang, P. C. Loh, P. Wang, F. H. Choo, F. Gao, "Exploring inherent damping characteristics of LCL-filters for three-phase grid-connected voltage source inverters", *IEEE Trans. Power Electron.*, vol. 27, no. 3, pp. 1433–1443, Mar. 2012.
- [4] D.G. Holms, T.A. Lipo, B.P. McGrath, W.Y. Kong, "Optimized design of stationary frame three phase ac current regulators", *IEEE Trans. Power Electron.*, vol. 24, no. 11, pp. 2417–2426, Nov. 2009.
- [5] G. Shen, Z. Xuancai, Z. Jun, X. Dehong, "A new feedback method for PR current control of LCL-filter-based grid-connected inverter", *IEEE Trans. Ind. Electron.*, vol. 57, no. 6, pp. 2033–2041, Jun. 2010.
- [6] R. Teodorescu, F. Blaabjerg, M. Liserre, A. Dell'Aquila, "A stable three-phase LCL-filter based active rectifier without damping", *Conf. Rec. IEEE IAS Annu. Meeting*, pp. 1552–1557, 2003.
- [7] J. Dannehl, C. Wessels, F. W. Fuchs, "Limitations of voltage-oriented PI current control of grid-connected PWM rectifiers with LCL filters", *IEEE Trans. Ind. Electron.*, vol. 56, no. 2, pp. 380–388, Feb. 2009.
- [8] S. Parker, B. P. McGrath, D. G. Holmes, "Region of active damping control for LCL filters", *IEEE Trans. Ind. Appl.*, vol. 50, no. 1, pp. 424–432, Jan./Feb. 2014.
- [9] J. G. Wang, J. D. Yan, L. Jiang, J. Y. Zou, "Delay-dependent stability of single-loop controlled grid-connected inverters with LCL filters", *IEEE Trans. Power Electron.*, vol. 31, no. 1, pp. 734–757, Jan. 2016.
- [10] Z. Xin, P. Mattavelli, W. Yao, Y. Yang, F. Blaabjerg, P. C. Loh, "Mitigation of grid current distortion for LCL-filtered voltage source inverter with inverter current feedback control", *IEEE Trans. Power Electron.*, vol. 33, no. 7, pp. 6248–6261, Jul. 2018.
- [11] C. Bao, X. Ruan, X. Wang, W. Li, D. Pan, K. Weng, "Step-by-step controller design for LCL-type grid-connected inverter with capacitor-current-feedback active-damping", *IEEE Trans. Power Electron.*, vol. 29, no. 3, pp. 1239–1253, Mar. 2014.

- [12] J. Yin, S. Duan, B. Liu, "Stability analysis of grid-connected inverter with LCL filter adopting a digital single-loop controller with inherent damping characteristic", *IEEE Trans. Ind. Informat.*, vol. 9, no. 2, pp. 1104–1112, May 2013.
- [13] C. Zou, B. Liu, S. Duan, R. Li, "Influence of delay on system stability and delay optimization of grid-connected inverters with LCL filter", *IEEE Trans. Ind. Informat.*, vol. 10, no. 3, pp. 1775–1784, Aug. 2014.
- [14] P. A. Dahono, "A control method to damp oscillation in the input LC-filter", *Proc. Power Electron. Spec. Conf.*, vol. 4, pp. 1630–1635, 2002.
- [15] V. Blasko, V. Kaura, "A novel control to actively damp resonance in input LC filter of a three-phase voltage source converter", *IEEE Trans. Ind. Appl.*, vol. 33, no. 2, pp. 542–550, Mar./Apr. 1997.
- [16] R. Pena-Alzola, M. Liserre, F. Blaabjerg, R. Sebastian, J. Dannehl, F. W. Fuchs, "Systematic design of the lead-lag network method for active damping in LCL-filter based three phase converters", *IEEE Trans. Ind. Informat.*, vol. 10, no. 1, pp. 43–52, Feb. 2014.
- [17] R. Pena-Alzola, M. Liserre, F. Blaabjerg, M. Ordonez, Y. Yang, "LCL-filter design for robust active damping in grid connected converters", *IEEE Trans. Ind. Informat.*, vol. 10, no. 4, pp. 2192–2203, Nov. 2014.
- [18] S. R. Dick, M. Rosekeit, J. Rolink, R. De Doncker, "Active damping of LCL resonance with minimum sensor effort by means of a digital infinite impulse response filter", *Proc. Eur. Conf. Power Electron. Appl.*, pp. 1–8, 2007.
- [19] Z. Bai, H. Ma, D. Xu, B. Wu, Y. Fang, Y. Yao, "Resonance damping and harmonic suppression for grid-connected current-source inverter", *IEEE Trans. Ind. Electron.*, vol. 61, no. 7, pp. 3146–3154, Jul. 2014.
- [20] M. Liserre, F. Blaabjerg, S. Hansen, "Design and control of an LCL -filter-based three-phase active rectifier ", *IEEE Trans. Ind. Appl.*, vol. 41, no. 5, pp. 1281–1291, Sep./Oct. 2005.
- [21] W. Wu, Y. He, F. Blaabjerg, "An LLCL power filter for single-phase grid-tied inverter", *IEEE Trans. Power Electron.*, vol. 27, no. 2, pp. 782–789, Feb. 2012.
- [22] J. Dannehl, M. Liserre, F. Fuchs, "Filter-based active damping of voltage source inverters with LCL filters", *IEEE Trans. Ind. Electron.*, vol. 58, no. 8, pp. 3623–3633, Oct. 2011.
- [23] X. Wang, F. Blaabjerg, P. C. Loh, "Virtual RC damping of LCL -filtered voltage source inverters with extended selective harmonic compensation", *IEEE Trans. Power Electron.*, vol. 30, no. 9, pp. 4726–4737, Sep. 2010.

- [24] P. Alemi, C. Bae, D. Lee, "Resonance suppression scheme based on PR control for single-phase grid-connected inverters with LLCL filters", *IEEE J. Emerg. Sel. Topics Power Electron.*, vol. 4, no. 2, pp. 459–467, Jun. 2016.
- [25] J. L. Agorreta, M. Borrega, J. Lopez, L. Marroyo, " Modeling and control of n -paralleled grid-connected inverters with LCL filter coupled due to grid impedance in PV plants ", *IEEE Trans. Power Electron.*, vol. 26, no. 3, pp. 770–785, Mar. 2011.
- [26] Y. Liu, W. Wu, Y. He, Z. Lin, F. Blaabjerg, H. Chung, "An efficient and robust hybrid damper for LCL- or LLCL-based grid-tied inverter with strong grid-side harmonic voltage effect rejection", *IEEE Trans. Ind. Electron.*, vol. 63, no. 2, pp. 926–936, Feb. 2016.
- [27] B. Wen, D. Boroyevich, R. Burgos, P. Mattavelli, Z. Shen, "Inverse Nyquist stability criterion for grid-tied inverters", *IEEE Trans. Power Electron.*, vol. 32, no. 2, pp. 1548–1556, Feb. 2017.
- [28] Y. He, H. S. H. Chung, C. N. M. Ho, W. Wu, "Modified cascaded boundary-deadbeat control for a virtually-grounded three-phase grid-connected inverter with LCL filter", *IEEE Trans. Power Electron.*, vol. 32, no. 10, pp. 8163–8180, Oct. 2017.
- [29] X. Wang, X. F. Blaabjerg, P. C. Loh, "Grid-current-feedback active damping for LCL resonance in grid-connected voltage source inverters", *IEEE Trans. Power Electron.*, vol. 3, no. 1, pp. 213–223, Jan. 2016.
- [30] Y. Tang, C. Yoon, R. Zhu, F. Blaabjerg, "Generalized stability regions of current control for LCL-filtered grid-connected inverters without passive or active damping", *Proc. IEEE Energy Convers. Congr. Expo.*, pp. 2040–2047, 2015.
- [31] R. Beres, X. Wang, F. Blaabjerg, M. Liserre, C. L. Bak, "A review of passive power filters for three-phase grid-connected voltage-source inverters", *IEEE Trans. Power Electron.*, vol. 4, no. 1, pp. 54–69, Mar. 2016.
- [32] A. K. Balasubramanian, V. John, "Analysis and design of split-capacitor resistive inductive passive damping for LCL filters in grid-connected inverters ", *IET Power Electron.*, vol. 6, no. 9, pp. 1822–1832, Nov. 2013.
- [33] W. Wu, Y. J. Sun, M. Huang, X. F. Wang, H. Wang, F. Blaabjerg, "A robust passive damping method for LLCL-filter-based grid-tied inverters to minimize the effect of grid harmonic voltages", *IEEE Trans. Power Electron.*, vol. 29, no. 7, pp. 3279–3289, Jul. 2014.
- [34] M. Liserre, R. Teodorescu, F. Blaabjerg, "Stability of photovoltaic and wind turbine grid-connected inverters for a large set of grid impedance values", *IEEE Trans. Power Electron.*, vol. 21, no. 1, pp. 263–272, Jan. 2006.

- [35] Y. Huang, X. Yuan, J. Hu, P. Zhou, "Modeling of VSC connected to weak grid for stability analysis of DC-link voltage control", *IEEE J. Emerg. Sel. Topics Power Electron.*, vol. 3, no. 4, pp. 1193–1204, Dec. 2015.
- [36] M. Ashabani, Y. A.-R. I. Mohamed, "Integrating VSCs to weak grids by nonlinear power damping controller with self-synchronization capability", *IEEE Trans. Power Syst.*, vol. 29, no. 2, pp. 805–814, Mar. 2014.
- [37] M. Davari, Y. A.-R. I. Mohamed, "Robust vector control of a very weak-grid-connected voltage-source converter considering the phase-locked loop dynamics", *IEEE Trans. Power Electron.*, vol. 32, no. 2, pp. 977–994, Feb. 2017.
- [38] D. Yang, X. Ruan, H. Wu, "Impedance shaping of the grid-connected inverter with LCL filter to improve its adaptability to the weak grid condition", *IEEE Trans. Power Electron.*, vol. 29, no. 11, pp. 5795–5805, Nov. 2014.
- [39] A. Adib, B. Mirafzal, X. Wang, F. Blaabjerg, "On stability of voltage source inverters in weak grids", *IEEE Access*, vol. 6, pp. 4427–4439, Jan. 2018.
- [40] P. Cortes M. P. Kazmierkowski R. M. Kennel D. E. Quevedo J. Rodriguez "Predictive control in power electronics and drives" *IEEE Trans. Ind. Electron.* vol. 55 no. 12 pp. 4312–4324, Dec. 2008.
- [41] K. S. Low R. Cao "Model predictive control of parallel-connected inverters for uninterruptible power supplies" *IEEE Trans. Ind. Electron.* vol. 55 no. 8 pp. 2884–2893, Aug. 2008.
- [42] S. Vazquez et al. "Model predictive control: A review of its applications in power electronics" *IEEE Ind. Electron. Mag.* vol. 8 no. 1 pp. 16–31, Mar. 2014.
- [43] V. Yaramasu and B. Wu, "Fundamentals of model predictive control," in *Model predictive control of wind energy conversion systems*, Hoboken, New Jersey, USA: Wiley, 2016, pp. 117–148.
- [44] J. Rodriguez et al. "State of the art of finite control set model predictive control in power electronics" *IEEE Trans. Ind. Informat.* vol. 9 no. 2 pp. 1003–1016, May 2013.
- [45] S. Alepuz S. Busquets-Monge J. Bordonau J. Gago D. Gonzalez and J. Balcells "Interfacing Renewable Energy Sources to the Utility Grid Using a Three-Level Inverter" *IEEE Trans. on Ind. Electron.* vol. 53 no. 5 pp. 1504–1511, Oct. 2006.
- [46] S. Kouro P. Cortes R. Vargas U. Ammann J. Rodriguez "Model predictive control—A simple and powerful method to control power converters" *IEEE Trans. Ind. Electron.* vol. 56 no. 6 pp. 1826–1838, Jun. 2009.
- [47] J. Rodriguez et al. "Predictive current control of a voltage source inverter" *IEEE Trans. Ind. Electron.* vol. 54 no. 1 pp. 495–503, Feb. 2007.

- [48] J. Nørgaard M. Graungaard T. Dragičević, F. Blaabjerg, "Current Control of LCL-Filtered Grid-Connected VSC using Model Predictive Control with Inherent Damping" in *2018 20th European Conference on Power Electronics and Applications. EPE's 18 ECCE Europe*, pp.1–9, 2018.
- [49] D. Pan, X. Ruan, X. Wang, H. Yu and Z. Xing, "Analysis and design of current control schemes for LCL-type grid-connected inverter based on a general mathematical model", *IEEE Trans. Power Electron.*, vol. 32, no. 6, pp. 4395–4410, Jun. 2017.
- [50] D. Yang, X. Wang, F. Liu, K. Xin, Y. Liu and F. Blaabjerg, "Adaptive reactive power control of PV power plants for improved power transfer capability under ultra-weak grid conditions", *IEEE Trans. Smart Grid*, vol. 10, no. 2, pp. 1269–1279, Mar. 2019.
- [51] D. Pan, X. Ruan, C. Bao, W. Li and X. Wang, "Optimized controller design for LCL -type grid-connected inverter to achieve high robustness against grid-impedance variation", *IEEE Trans. Ind. Electron.*, vol. 62, no. 3, pp. 1537–1547, Mar. 2015.
- [52] D. Pan, X. Ruan, X. Wang, F. Blaabjerg, X. Wang and Q. Zhou, "A highly robust single-loop current control scheme for grid-connected inverter with an improved LCCL filter configuration", *IEEE Trans. Power Electron.*, vol. 33, no. 10, pp. 8474–8487, Oct. 2018.
- [53] D. Yang, X. Ruan and H. Wu, "A real-time computation method with dual sampling mode to improve the current control performance of the LCL -type grid-connected inverter", *IEEE Trans. Ind. Electron.*, vol. 62, no. 7, pp. 4563–4572, Jul. 2015.
- [54] C. Zhou, H. Jiang and F. Xie, "Control research of NPC three level high-power grid connected inverter based on multi sampling", *Proc. 13th Annu. IEEE Conf. Ind. Electron. Appl.*, pp. 1386–1389, 2018.
- [55] K. H. Ahmed, A. M. Massoud, S. J. Finney and B. W. Williams, "Sensorless current control of three-phase inverter-based distributed generation", *IEEE Trans. Power Deliv.*, vol. 24, no. 2, pp. 919–929, Apr. 2009.
- [56] T. Nussbaumer, M. L. Heldwein, G. Gong, S. D. Round and J. W. Kolar, "Comparison of prediction techniques to compensate time delays caused by digital control of a three-phase buck-type PWM rectifier system", *IEEE Trans. Ind. Electron.*, vol. 55, no. 2, pp. 791–799, Feb. 2008.
- [57] S. Bibian and H. Jin, "Time delay compensation of digital control for DC switch-mode power supplies using prediction techniques", *IEEE Trans. Power Electron.*, vol. 15, no. 5, pp. 835–842, Sep. 2000.
- [58] K. Jalili and S. Bernet, "Design of LCL filters of active-front-end two-level voltage-source converters", *IEEE Trans. Ind. Electron.*, vol. 56, no. 5, pp. 1674–1689, May 2009.

- [59] R. Peña-Alzola, M. Liserre, F. Blaabjerg, R. Sebastián, J. Dannehl and F. W. Fuchs, "Systematic design of the lead-lag network method for active damping in LCL -filter based three phase converters", *IEEE Trans. Ind. Inform.*, vol. 10, no. 1, pp. 43–52, Feb. 2014.
- [60] X. Li, X. Wu, Y. Geng, X. Yuan, C. Xia and X. Zhang, "Wide damping region for LCL -type grid-connected inverter with an improved capacitor-current-feedback method", *IEEE Trans. Power Electron.*, vol. 30, no. 9, pp. 5247–5259, Sep. 2015.
- [61] C. Chen, J. Xiong, Z. Wan, J. Lei and K. Zhang, "A time delay compensation method based on area equivalence for active damping of an LCL -type converter", *IEEE Trans. Power Electron.*, vol. 32, no. 1, pp. 762–772, Jan. 2017.
- [62] Z. Xin, X. Wang, P. C. Loh and F. Blaabjerg, "Grid-current-feedback control for LCL -filtered grid converters with enhanced stability", *IEEE Trans. Power Electron.*, vol. 32, no. 4, pp. 3216–3228, Apr. 2017.
- [63] M. Lu, X. Wang, P. C. Loh, F. Blaabjerg and T. Dragicevic, "Graphical evaluation of time-delay compensation techniques for digitally controlled converters", *IEEE Trans. Power Electron.*, vol. 33, no. 3, pp. 2601–2614, Mar. 2018.
- [64] X. Wang, F. Blaabjerg and P. C. Loh, "Virtual RC damping of LCL -filtered voltage source converters with extended selective harmonic compensation", *IEEE Trans. Power Electron.*, vol. 30, no. 9, pp. 4726–4737, Sep. 2015.
- [65] Q. Huang and K. Rajashekara, "Virtual RLC active damping for grid-connected inverters with LCL filters", *Proc. 32th Annu. IEEE Appl. Power Electron. Conf. Exp.*, pp. 424–429, 2017.
- [66] A. Niragire, "Linear quadratic optimal control for a cascaded converters-based microgrid." M.S. thesis, Dept. Elect. Eng., the University of Arkansas, Fayetteville, AR, USA, 2017.
- [67] A. Reznik, M. G. Simões, A. Al-Durra and S. M. Muyeen, "LCL Filter Design and Performance Analysis for Grid-Interconnected Systems," in *IEEE Transactions on Industry Applications*, vol. 50, no. 2, pp. 1225–1232, March-April 2014.
- [68] M. Liserre, F. Blaabjerg and S. Hansen, "Design and control of an LCL-filter-based three-phase active rectifier," in *IEEE Transactions on Industry Applications*, vol. 41, no. 5, pp. 1281–1291, Sept.-Oct. 2005.
- [69] M. Said-Romdhane, M. Naouar, I. Belkhodja, E. Monmasson, "An Improved LCL Filter Design in Order to Ensure Stability without Damping and Despite Large Grid Impedance Variations", *Energies*, vol. 10, pp. 336, 2017.
- [70] A. A. Rockhill, M. Liserre, R. Teodorescu and P. Rodriguez, "Grid-Filter Design for a Multimegawatt Medium-Voltage Voltage-Source Inverter," in *IEEE Transactions on Industrial Electronics*, vol. 58, no. 4, pp. 1205–1217, April 2011.

- [71] D. Pan, X. Ruan, C. Bao, W. Li and X. Wang, "Optimized Controller Design for LCL-Type Grid-Connected Inverter to Achieve High Robustness Against Grid-Impedance Variation," in *IEEE Transactions on Industrial Electronics*, vol. 62, no. 3, pp. 1537–1547, March 2015.
- [72] S. G. Parker, B. P. McGrath and D. G. Holmes, "Regions of Active Damping Control for LCL Filters," in *IEEE Transactions on Industry Applications*, vol. 50, no. 1, pp. 424–432, Jan.-Feb. 2014.
- [73] P. T. Krein, "Inverters," in *Elements of Power Electronics*, 2nd ed. New York, USA: Oxford Univ. Press, 2015, ch. 5, pp. 246–290.
- [74] M. Davari and Y. A. R. I. Mohamed, "Robust vector control of a very weak grid-connected voltage-source converter considering the phase-locked loop dynamics," in *IEEE Transactions on Power Electronics*, vol. 32, no. 2, pp. 977–994, Feb 2017.
- [75] Y. Han, M. Yang, H. Li, P. Yang, L. Xu, E. A. A. Coelho, et al., " Modeling and stability analysis of LCL -type grid-connected inverters: A comprehensive overview ", *IEEE Access*, vol. 7, pp. 114975–115001, Aug. 2019.
- [76] C. C. Gomes, A. F. Cupertino and H. A. Pereira, "Damping techniques for grid-connected voltage source converters based on LCL filter: An overview", *Renew. Sustain. Energy Rev.*, vol. 81, pp. 116–135, Jan. 2018.
- [77] X. Ruan, X. Wang, D. Pan, D. Yang, W. Li and C. Bao, *Control Techniques for LCL-Type Grid-Connected Inverters*, Singapore:Springer, 2017.
- [78] R. Peña-Alzola, M. Liserre, F. Blaabjerg, R. Sebastián, J. Dannehl and F. W. Fuchs, " Analysis of the passive damping losses in LCL -filter-based grid converters ", *IEEE Trans. Power Electron.*, vol. 28, no. 6, pp. 2642–2646, Jun. 2013.
- [79] A. K. Balasubramanian and V. John, "Analysis and design of split-capacitor resistiveinductive passive damping for LCL filters in grid-connected inverters", *IET Power Electron.*, vol. 6, no. 9, pp. 1822–1832, Nov. 2013.
- [80] R. N. Beres, X. Wang, F. Blaabjerg, M. Liserre and C. L. Bak, "Optimal design of high-order passive-damped filters for grid-connected applications", *IEEE Trans. Power Electron.*, vol. 31, no. 4, pp. 2083–2098, Mar. 2016.
- [81] P. Channegowda and V. John, "Filter optimization for grid interactive voltage source inverters", *IEEE Trans. Ind. Electron.*, vol. 57, no. 12, pp. 4106–4114, Dec. 2010.
- [82] C. Liu, K. Dai, K. Duan and Y. Kang, "Application of a C-type filter based LCFL output filter to shunt active power filters", *J. Power Electron.*, vol. 13, no. 6, pp. 1058–1069, Nov. 2013.

- [83] W. Yao, Y. Yang, X. Zhang, F. blaabjerg and P. C. Loh, "Design and analysis of robust active damping for LCL filters using digital notch filters", *IEEE Trans. Power Electron.*, vol. 32, no. 3, pp. 2360–2375, Mar. 2017.
- [84] J. Dannehl, F. W. Fuchs, S. Hansen and P. B. Thøgersen, "Investigation of active damping approaches for PI-based current control of grid-connected pulse width modulation converters with LCL filters", *IEEE Trans. Ind. Appl.*, vol. 46, no. 4, pp. 1509–1517, Jul./Aug. 2010.
- [85] D. Pan, X. Ruan, C. Bao, W. Li and X. Wang, "Capacitor-current-feedback active damping with reduced computation delay for improving robustness of LCL-type grid-connected inverter", *IEEE Trans. Power Electron.*, vol. 29, no. 7, pp. 3414–3427, Jul. 2014.
- [86] X. Wang, C. Bao, X. Ruan, W. Li and D. Pan, " Design considerations of digitally controlled LCL -filtered inverter with capacitor- current-feedback active damping ", *IEEE J. Emerg. Sel. Topics Power Electron.*, vol. 2, no. 4, pp. 972–984, Dec. 2014.
- [87] Y. He, X. Wang, X. Ruan, D. Pan, X. Xu and F. Liu, "Capacitor-current proportional-integral positive feedback active damping for LCL-type grid-connected inverter to achieve high robustness against grid impedance variation", *IEEE Trans. Power Electron.*, vol. 34, no. 12, pp. 12423–12436, Dec. 2019.
- [88] X. Wang, F. Blaabjerg and P. C. Loh, "Virtual RC damping of LCL-filtered voltage source converters with extended selective harmonic compensation", *IEEE Trans. Power Electron.*, vol. 30, no. 9, pp. 4726–4737, Sep. 2015.
- [89] H.-C. Chen, P.-T. Cheng, F. Blaabjerg and X. Wang, "A passivity-based stability analysis of the active damping technique in the offshore wind farm applications", *IEEE Trans. Ind. Appl.*, vol. 54, no. 5, pp. 5074–5082, Sep./Oct. 2018.
- [90] C. Nie, Y. Wang, W. Lei, M. Chen and Y. Zhang, "An enhanced control strategy for multiparalleled grid-connected single-phase converters with load harmonic current compensation capability", *IEEE Trans. Ind. Electron.*, vol. 65, no. 7, pp. 5623–5633, Jul. 2018.
- [91] Y. Guan, Y. Wang, Y. Xie, Y. Liang, A. Lin and X. Wang, "The dual-current control strategy of grid-connected inverter with LCL filter", *IEEE Trans. Power Electron.*, vol. 34, no. 6, pp. 5940–5952, Jun. 2019.
- [92] J. W. He and Y. W. Li, "Generalized closed-loop control schemes with embedded virtual impedances for voltage source converters with LC or LCL filters", *IEEE Trans. Power Electron.*, vol. 27, no. 4, pp. 1850–1861, Apr. 2012.
- [93] J. Xu, S. Xie and T. Tang, "Active damping-based control for grid-connected LCL - filtered inverter with injected grid current feedback only", *IEEE Trans. Ind. Electron.*, vol. 61, no. 9, pp. 4746–4758, Sep. 2014.

- [94] X. Wang, F. Blaabjerg and P. C. Loh, "Grid-current-feedback active damping for LCL resonance in grid-connected voltage-source converters", *IEEE Trans. Power Electron.*, vol. 31, no. 1, pp. 213–223, Jan. 2016.
- [95] Z. Lin, W. Yao, Z. Bai and Z. Lu, "Study on active damping of LCL filter resonance based on grid current feedback compensation", *Proc. IEEE Int. Symp. Ind. Electron. (ISIE)*, pp. 1–6, May 2013.
- [96] M. Hanif, V. Khadkikar, W. Xiao and J. L. Kirtley, "Two degrees of freedom active damping technique for LCL filter-based grid connected PV systems", *IEEE Trans. Ind. Electron.*, vol. 61, no. 6, pp. 2795–2803, Jun. 2014.
- [97] R. A. Fantino, C. A. Busada and J. A. Solsona, "Optimum PR control applied to LCL filters with low resonance frequency", *IEEE Trans. Power Electron.*, vol. 33, no. 1, pp. 793–801, Jan. 2018.
- [98] Y. Chen, Z. Xie, L. Zhou, Z. Wang, X. Zhou, W. Wu, et al., "Optimized design method for grid-current-feedback active damping to improve dynamic characteristic of LCL-type grid-connected inverter", *Int. J. Electr. Power Energy Syst.*, vol. 100, pp. 19–28, Sep. 2018.
- [99] X. P. Zhou, L. Zhou, Y. Chen, Z. Shuai, J. M. Guerrero, A. Luo, et al., "Robust grid-current-feedback resonance suppression method for LCL-type grid-connected inverter connected to weak grid", *IEEE J. Emerg. Sel. Topics Power Electron.*, vol. 6, no. 4, pp. 2126–2137, Dec. 2018.
- [100] Z. Xin, X. Wang, P. C. Loh and F. Blaabjerg, "Grid-current-feedback control for LCL-filtered grid converters with enhanced stability", *IEEE Trans. Power Electron.*, vol. 32, no. 4, pp. 3216–3228, Apr. 2017.
- [101] J. Wang, J. D. Yan and J. Zou, "Inherent damping of single-loop digitally controlled voltage source inverters with LCL filters", *Proc. IEEE Int. Symp. Ind. Electron. (ISIE)*, pp. 487–492, Jun. 2016.
- [102] E. Twining and D. G. Holmes, "Grid current regulation of a three-phase voltage source inverter with an LCL input filter", *IEEE Trans. Power Electron.*, vol. 18, no. 3, pp. 888–895, May 2003.
- [103] D. N. Zmood and D. G. Holmes, "Stationary frame current regulation of PWM inverters with zero steady-state error", *IEEE Trans. Power Electron.*, vol. 18, no. 3, pp. 814–822, May 2003.
- [104] W. Yang, Y. Cho, C. Choo, J. Shim, W. Jeon, J. Kim, S. Yu, K. Park, J. Wee, and P. Kumar H., "Kalman filter and wiener filter" in *MATLAB/Simulink for Digital Signal Processing*. Seoul, Korea: Hongrung Publishing Company, 2012, pp. 265–293.

- [105] H. Miranda, R. Teodorescu, P. Rodriguez, and L. Helle, "Model predictive current control for high-power grid-connected converters with output LCL filter", in *Proc. Industrial Electronics, 2009. IECON '09. 35th Annual Conference of IEEE*, pp. 633–638, 2009.
- [106] R. Guzman, L. G. de Vicuña, A. Camacho, J. Miret and J. M. Rey, "Receding-horizon model-predictive control for a three-phase VSI with an LCL filter", *IEEE Trans. Ind. Electron.*, vol. 66, no. 9, pp. 6671-6680, Sep. 2019.
- [107] T. Dragicevic, "Model Predictive Control of Power Converters for Robust and Fast Operation of AC Microgrids", *IEEE Trans. Power Electron.*, vol. 33, no. 7, pp. 6304–6317, Jul. 2018.

APPENDICES

Appendix A: NCREPT Microgrid System Parameters

Appendix A summarizes the parameters and their values for the microgrid modelled in chapter III.

TABLE A.1
TRANSFORMERS

Transformer Name	Connection Type	Voltage (kV)	Rated Power (kVA)	Impedance (~ %)
T1	Δ/Y	0.480/13.8	2500	5
T2	Δ/Y	0.480/13.8	2500	5
T3	Δ/Y	0.480/13.8	2500	5
T4	Δ/Y	0.480/13.8	2500	5
T5	Δ/Y	0.480/13.8	2500	5
T6	Δ/Y	0.480/13.8	2500	5
Utility Txmr	Y/Y	12.47/0.480	15000	5

TABLE A.2
REGENERATIVE DRIVE (REGEN) - PARAMETERS

Name	Unit Value	Set Up	Total Value
EMI Filter Cap	20 μ F	1 per line, input side	20 μ F
Filter Cap	3 x 96 μ F, Δ	5 on each side	3 x 480 μ F
Filter Inductor	20 μ H @ 2500 A	1 on each side	20 μ H
DC Capacitor	2700 μ F	28 of series pairs	37800 μ F
Rectifier Switching Frq	4 kHz		4 kHz
Inverter Switching Frq.	5 kHz		5 kHz

TABLE A.3
VARIABLE VOLTAGE VARIABLE FREQUENCY (VVVF) DRIVE - RATINGS

Name	Unit Value
Input Voltage	120 - 528 Vac
Output Voltage	-----
Output Current	2000 A (RMS) @ 30 °C
IGBT Current	1500 A DC, Continuous
Input Frequency	47-63 Hz
Output Frequency	-----
Overload Capacity	110 % for 60 sec, 125 % for 3 sec

TABLE A.4
VARIABALE VOLTAGE VARIABLE FREQUENCY (VVVF) DRIVE - PARAMETERS

Name	Unit Value	Set Up	Total Value
EMI Filter Cap	20 μ F	2 per line, on input side only	40 μ F
Filter Cap	3 x 96 μ F, Δ	10 on each side	3 x 960 μ F
Filter Inductor	110 μ H @ 750 A	1 on each side	110 μ F
DC Capacitor	2700 μ F	28 of series pairs	37800 μ F
Rectifier Switching Frq	8 kHz		8 kHz
Inverter Switching Frq	10 kHz		10 kHz

TABLE A.5
VARIABALE VOLTAGE VARIABLE FREQUENCY (VVVF) DRIVE - RATINGS

Name	Unit Value
Input Voltage	360 - 528 Vac
Output Voltage	120 - 520 Vav
Output Current	685 A (RMS) @ 40 °C
IGBT Current	1500 A DC, Continuous
Input Frequency	47-63 Hz
Output Frequency	45-66 Hz
Overload Capacity	150 % for 60 sec, 175 % for 3 sec